CIRCULAR PLATES SUBJECTED TO LOCALISED BLAST LOADS - SOME INSIGHTS INTO THE MECHANISM OF TEARING AND THE ENERGY REQUIRED

Miles Alexander Wiehahn

A dissertation submitted to the Department of Mechanical Engineering,
University of Cape Town, in fulfilment of the requirements
for the degree of Master of Science in Engineering.

Cape Town, June 2000

Declaration

I declare that this dissertation is essentially my own work. It is being submitted for the degree of Master of Science in Engineering in the University of Cape Town. It has not been submitted in this or any other form for a degree or examination in any other university.

Acknowledgments

The author wishes to thank my supervisor Professor G.N. Nurick, Mr H.C. Bowles and the staff and students of CERECAM and Mechanical Engineering for their helpful comments, advice and suggestions.

I acknowledge the financial support received from the National Research Foundation (NRF), Centre for Research in Computational and Applied Mechanics (CERECAM) and the Department of Mechanical Engineering.

Contents

Declaration i

Abstract ii

Acknowledgements v

Contents vi

List of Figures x

List of Tables xiv

List of Symbols xv

1 INTRODUCTION 1
- 1.1 BACKGROUND 1
- 1.2 OBJECTIVES OF THIS THESIS 2
- 1.3 SCOPE OF THIS THESIS 2
- 1.4 PLAN OF DEVELOPMENT 3

2 LITERATURE REVIEW 4
- 2.1 THE ENERGY OF TEARING 4
- 2.2 BLAST EXPLOSION ON THIN BUILT-IN CIRCULAR PLATES . . . 7
- 2.3 MODELLING EXPLOSIVE BLASTS 9
  - 2.3.1 APPLYING PRESSURE TO MODEL THE EXPLOSION 9
  - 2.3.2 USING THE EQUATION OF STATE 10

2.4 MODELLING THE MATERIAL PROPERTIES 13
2.4.1 CLASSICAL METAL PLASTICITY 13
2.4.2 JOHNSON-COOK PLASTICITY MODEL 15
2.4.3 FAILURE CRITERIA 16
2.5 FORMATION AND MODELLING OF SHEAR BANDS 17

3 EXPERIMENTAL DATA **20**
3.1 EXPERIMENTAL PROCEDURE 20
3.1.1 METHOD OF CREATING THE BLAST 21
3.1.2 THE TEST PLATES 22
3.1.3 THE BALLISTIC PENDULUM 23
3.1.4 THE VELOCITY MEASURING DEVICE 24
3.2 EXPERIMENTAL RESULTS 24
3.2.1 FRAGMENT VELOCITY 25
3.2.2 THE CRITICAL IMPULSE THAT RESULTS IN FRACTURE 27
3.2.3 OBSERVATION ABOUT THE FRACTURE SURFACE 29

4 METHOD OF FINITE ELEMENT MODELLING **33**
4.1 FINITE ELEMENT ANALYSIS PROCEDURE 33
4.2 FINITE ELEMENT MODEL GEOMETRY 34
4.2.1 MODEL SYMMETRY 34
4.2.2 ELEMENTS USED 35
4.2.3 BOUNDARY CONDITIONS 36
4.3 MATERIAL PROPERTIES 37
4.3.1 YIELD HARDENING 38
4.3.2 STRAIN RATE 38
4.3.3 TEMPERATURE DEPENDENCE 39
4.4 MODELLING THE BLAST 40
4.4.1 PRESSURE DISTRIBUTION USED 42
4.4.2 DETERMINING THE EXPONENTIAL DECAY 43

5 FINITE ELEMENT RESULTS **45**

5.1 PLATE MODELLING USING A COARSE MESH 45
5.1.1 UNCAPPED PLATES 46
5.1.2 CAPPED PLATES 46
5.2 PLATE MODELLING USING FINE MESHES 52
5.2.1 EFFECT OF MESH DENSITY 53
5.3 POSSIBLE EXPLANATION OF THE MESH DEPENDENT RESULTS 60
5.4 METHOD OF PLATE FAILURE 61
5.5 THE NUMERICAL ENERGIES 62
5.5.1 THE WHOLE MODEL ENERGIES 62
5.5.2 THE SHEAR BAND ENERGY 66
5.5.3 DETERMINING THE ENERGY OF TEARING 67

6 CONCLUSIONS **71**
6.1 MODELLING USING TEMPERATURE DEPENDENT MATERIAL PROPERTIES 71
6.1.1 COARSE MESHES 71
6.1.2 FINE MESHES 72
6.2 INSIGHTS INTO THE METHOD OF FRACTURE 72
6.3 THE ENERGY OF TEARING DURING CAPPING 73
6.4 CONCLUDING REMARK 73

7 RECOMMENDATIONS **74**
7.1 RECOMMENDATIONS FOR FUTURE BLAST EXPERIMENTATION 74
7.2 RECOMMENDATIONS ON THE MODELLING OF DYNAMIC FRACTURE 75
7.3 WORK ON THE MODELLING OF THE EXPLOSION 75

REFERENCES **76**

A MEASUREMENT OF THE APPLIED IMPULSE **80**

B EXPERIMENTAL RESULTS 83

C VELOCITY DATA 85

D THE JWL EQUATION OF STATE 89
D.1 THE FEM MODEL 89
D.2 JWL MATERIAL PROPERTIES 89
D.3 COMPARISON BETWEEN THE DIFFERENT CONTACT METHODS 90
D.4 DETERMINING THE IMPULSE 91
D.4.1 OBTAINING THE IMPULSE FOR THE NUMERICAL SOLUTION 91
D.4.2 IMPULSE RESULTS 93
D.5 CONCLUSION 95

E GRAPHS OF THE OPTIMUM EXPONENTIAL DECAY 96

F USER SUBROUTINE VDLOAD 99

G ABAQUS/EXPLICIT INPUT DECKS 101
G.1 COARSE MESH EXAMPLE 101
G.2 FINE MESH EXAMPLE 108

H COARSE MESH RESULTS 116
H.1 PLASTICALLY DEFORMED PLATES 116
H.2 CAPPED PLATES 116

I FINE MESH RESULTS 125

List of Figures

2.1 JWL Equation of State Example Given in the ABAQUS Manual. . . . 12

2.2 The JWL Equation of State as Used by Grobbelaar. 13

3.1 The Explosive Setup. 21

3.2 Test Specimen Dimensions. 22

3.3 A Diagram of the Blast Pendulum. 23

3.4 A Diagram of the Velocity Measuring Device. 25

3.5 A Top View of a Platically Deformed Plate. 26

3.6 Oblique View of a Plastically Deformed Plate. 26

3.7 A Top View of a Capped Plate. 27

3.8 Fragment Position Time History. 28

3.9 80 % Tearing in the Region of Capping. 29

3.10 Plate Cross Section Showing the Different Angles of Fracture. 31

3.11 A Plate with an Angle of Fracture Mainly of 45^0. 31

3.12 A Plate with a Fracture Angle of Mainly 135^0. 32

3.13 A Plate with an Angle of Fracture of 45^0 and 135^0 to the Deformed Plate. 32

4.1 Schematic of a CAX4R Element. 35
4.2 Schematic of a CAX3 Element. 36
4.3 Encastred Boundary Conditions. 36
4.4 Modelling the Support. 37
4.5 True Stress and Logarithmic Plastic Strain. 38
4.6 Young's Modulus as a Function of Temperature. 41
4.7 Normalised Yield Stress as a Function of Temperature. 41
4.8 Effect of Temperature on the Young's Modulus and Yield Stress. . . . 42
4.9 Pressure Distribution used to Model the Capped Plates. 44

5.1 Whole Model Displacement and Temperature Profiles of an Uncapped Plate Using a Coarse Mesh (1 x 0.292 mm). 47
5.2 Whole Model Displacement and Temperature Profiles of a Capped Plate Using a Coarse Mesh (1 x 0.292 mm). 49
5.3 Displacement and Temperature Profiles in the Area of Cap Formation for a Coarse Mesh (1 x 0.292 mm). 50
5.4 Displacement and Temperature Profiles at the Plate Boundary for a Coarse mesh (1 x 0.292 mm). 51
5.5 Whole Model Deformation and Temperature Profiles for a Mesh Density of 0.04 x 0.04 mm. 54
5.6 Shear Band Formation for a Mesh Density of 0.04 x 0.04 mm. 55
5.7 Shear Band Fracture for a Mesh Density of 0.04 x 0.04 mm. 56
5.8 Temperature Localization at the Boundary of the Thin Plate for a Mesh Density of 0.04 x 0.04 mm. 57
5.9 The Effects of Mesh Density on the Shear Bands. 59

5.10 Whole Model Energies with a Coarse Mesh (1 x 0.292 mm). 64

5.11 Whole Model Energies with a Coarse Mesh Using a Different Time Scale (1 x 0.292 mm). 64

5.12 Whole Model Energies with a Fine Mesh (0.04 x 0.04 mm). 65

5.13 Comparison of the Kinetic Energy for both a Fine and Coarse Mesh. . 65

5.14 Strain Energy Along the Plate Midpoint for Different Times (Mesh Density of 0.04 x 0.04 mm). 68

5.15 Defined Regions to Determine the Approximate Shear Band Energy. . 68

5.16 Total Strain energy in the Fractured and Shear Band Region. 69

5.17 Additional Strain Energy Required to Form the Shear Band untill the Point of Fracture. 69

5.18 Effect of Mesh Density on Shear Band Strain Energy. 70

C.1 Example of an Oscilloscope Reading. 86

C.2 Fragment Position Time History. 86

C.3 Velocity Diagram Showing the Measured and True Velocity. 87

D.1 Free Body Diagram of the Finite Element Model. 93

D.2 Impulse Obtained for Different Methods of Modelling the Blast. 94

E.1 Optimum Displacement Profile for Plate T5 (k=1.1). 97

E.2 Optimum Displacement Profile for Plate T6 (k=1.3). 97

E.3 Optimum Displacement Profile for Plate T7 (k 1.15). 98

H.1 Temperature Profiles of Plate T5 for a Mesh Density of 1 x 0.278 mm. 117

H.2 Temperature Profiles of Plate T6 for a Mesh Density of 1 x 0.268 mm. 118

H.3 Temperature Profiles of Plate T7 for a Mesh Density of 1 x 0.328 mm. 119

H.4 Temperature Profiles of Plate T10 for a Mesh Density of 1 x 0.292 mm. 120

H.5 Temperature Profiles of Plate T11 for a Mesh Density of 1 x 0.258 mm. 121

H.6 Temperature Profiles of Plate T12 for a Mesh Density of 1 x 0.305 mm. 122

H.7 Temperature Profiles of Plate T16 for a Mesh Density of 1 x 0.30 mm. 123

H.8 Temperature Profiles of Plate T18 for a Mesh Density of 1 x 0.288 mm. 124

I.1 Temperature Profiles of Plate T10 for a Mesh Density of 0.04 x 0.04 mm. 126

I.2 Temperature Profiles of Plate T11 for a Mesh Density of 0.04 x 0.04 mm. 127

I.3 Temperature Profiles of Plate T12 for a Mesh Density of 0.04 x 0.04 mm. 128

I.4 Temperature Profiles of Plate T16 for a Mesh Density of 0.04 x 0.04 mm. 129

I.5 Temperature Profiles of Plate T18 for a Mesh Density of 0.04 x 0.04 mm. 130

List of Tables

2.1 FRACTURE RESULTS OF THIN CIRCULAR BUILT IN PLATES . 8

3.1 EXPERIMENTALY MEASURED FRAGMENT VELOCITIES 28

3.2 FRACTURE RESULTS OF THE EXPERIMENTAL TESTS 30

4.1 OPTIMISED EXPONENTIAL DECAY 44

5.1 COARSE MESH SIMULATION RESULTS 52

5.2 FINE MESH SIMULATION RESULTS 58

5.3 EFFECT OF MESH DENSITY ON FINE MESHES 60

B.1 EXPERIMENTAL RESULTS 84

C.1 FRAGMENT POSITION TIME HISTORY 85

C.2 TRUE FRAGMENT VELOCITY 88

D.1 JWL EQUATION OF STATE MATERIAL PROPERTIES 90

D.2 MIDPOINT PLATE DISPLACEMENT USING THE NORMAL CONTACT METHOD 91

D.3 MIDPOINT PLATE DISPLACEMENT USING THE PENALTY CONTACT METHOD 92

List of Symbols

A	Johnson and Cook material property
A	Area of the specimen that the blast wave is applied
B	Johnson and Cook material property
B	Plate width
C	Johnson and Cook material property
c_d	Material wave speed
d_1- d_5	Johnson and Cook material property failure parameters
E	Young's modulus
E_{DF}	Deformation strain energy of the front plate
E_{DR}	Deformation strain energy for the rear plate
E_F	Friction energy when the fragment is welded to the back face
E_{IN}	Total input energy due to the blast
E_{mo}	Energy per unit mass
E_R	Residual kinetic energy of the fragment
E_{TF}	Energy required for the tearing of the front plate
E_{TR}	Energy required for the tearing of the back plate
I	Impulse
I	Internal element forces
k	Exponential decay
K	Geometric constant
L	Plate length
L^e	Element length
M	Mass matrix

m	Johnson and Cook material property
n	Johnson and Cook material property
n	Number of points
p	Pressure
P	Blast pressure
R_0	Explosive radius
R	Plate radius
R_1	JWL material constant
R_2	JWL material constant
t	Plate thickness
t	Time
t_{bd}	Blast duration
T_i^t	Temperature at node i and time t
$\ddot{u}$	Nodal accelerations
w	Tube half width
V_b	Burn speed of the explosive
α	Thermal diffusivity
Δt	Time increment
Δx	Node spacing
$\Delta_{yExperimental}$	Experimental displacement
$\Delta_{yNumerical}$	Numerical displacement
$\Delta\epsilon^{pl}$	Increment of the equivalent plastic strain
δ	Maximum midpoint deflection
ε_{norm}	Nominal strain
$\epsilon_{\ln}^{pl}$	Logarithmic plastic strain
$\dot{\epsilon}^{pl}$	Equivalent plastic strain rate
$\bar{\epsilon}_f^{pl}$	Equivalent plastic failure strain
σ	Yield stress
σ_{true}	True stress
σ_{norm}	Nominal stress
σ_y	Temperature dependent static yield stress

σ_{yo}	Static yield stress at the reference temperature
σ_0	Static yield stress
ρ	Material density
θ	Current material temperature
$\hat{\theta}$	Non-dimensional temperature
θ_{melt}	Melting temperature
$\theta_{transitional}$	Transitional temperature
ϕ	Dimensionless impulse
ω	JWL material constant
ω	Shear failure damage parameter

Chapter 1

INTRODUCTION

Extreme loading situations, such as blast loads, occur far more frequently than people would like to believe. Disasters occur due to insufficient knowledge of design parameters, unexpected working conditions, acts of god or by sabotage. It is imperative that designers look into the "what if" situations and learn to limit the damage of these disasters saving lives and money.

1.1 BACKGROUND

Explosive impulse loading on metal plates results in one of four possibilities (see Section 2.2 for full details):

- Large inelastic deformation.
- Large inelastic deformation with partial tearing.
- Large inelastic deformation with complete tearing resulting in the formation of fragments.
- No or little deformation with complete tearing.

The large inelastic deformation response of thin plates has been extensively reported in the literature. Empirical and analytical equations have been developed to determine the deformation profiles of the plates and failure modes have been identified.

However, the subject of plate fragmentation due to blast loading is less established. Less work on the energy evaluation of the fragmented plates has been done. The energy required to tear the plates is still unknown although it would be of great aid to the establishment of fracture criteria and could improve structural codes.

1.2 OBJECTIVES OF THIS THESIS

The objective of this thesis is to undertake an energy balance on explosively loaded plates and determine the energy of tearing. In particular the following items should be addressed:

- Determine the velocity of the capped fragments.
- Determine the fracture process when a fragment is formed.
- Undertake an energy balance on the plates.
- Determine the amount of energy required to make the plate tear.
- Draw conclusions from the results and base recommendations on the conclusions.

1.3 SCOPE OF THIS THESIS

The scope of this study extends to experimental tests of plates subjected to blast loads with the intention of measuring the velocity of the fragments and the subsequent modelling of the plates. A comparison of the results of the numerical and experimental results must be undertaken. An energy balance of the fractured plates must be undertaken with the aim of determining the energy of tearing.

1.4 PLAN OF DEVELOPMENT

This thesis has the following plan of development:

- Literature review - this chapter contains a review of all the literature that pertains to the study. The key areas addressed are energy balances on fractured plates, blast explosions on circular plates, modelling blasts, material properties and work pertaining to shear bands.
- Experimental data - the method of undertaking the experimentation and the subsequent experimental results and observations are outlined in this chapter.
- Method of finite element modelling - the method of modelling the plates is explained in detail.
- Finite element results - the results and observations of the finite element modelling are presented in this chapter.
- Conclusions - conclusions are drawn from the experimental data, numerical modelling, the subsequent energy balance and the literature review.
- Recommendations - suggested further investigations are presented in this section.

Chapter 2

LITERATURE REVIEW

A number of different topics had to be researched for this study. The main areas are:

- Early attempts to obtain the energy of tearing.
- Experimental blast work on built-in thin circular plates.
- Modelling the blast waves.
- Suitable material models available.
- The formation and modelling of shear bands.

2.1 THE ENERGY OF TEARING

Shen and Jones [1] devised a theoretical analysis examining the plastic response and failure of fully clamped plates subjected to uniformly distributed impulse loads. The rigid plastic analysis used an energy density failure criterion to predict failure at the support of the plate. The correlation between the experimental results for a theoretical critical impulse to rupture was poor, possibly because the experimental plates were not ideally clamped.

Nurick and Bryant [2] investigated fragmentation damage as a result of an explosion. Two sets of explosive tests were carried out on square tubing of 100 x 100 mm with thicknesses of 2 and 3 mm. As a result of the blast, either the front face of the tube was deformed or the resulting fragment from the front face deformed the rear face. In some cases the fragment was welded on to the back face of the tube due to the high velocity of the fragment.

An energy balance of the system was introduced as:

$$E_{IN} = E_{DF} + E_{TF} + E_R \tag{2.1}$$

where

E_{IN} Total input energy due to the blast.

E_{DF} Deformation strain energy of the front plate.

E_{TF} = Energy required for the tearing of the front plate.

E_R = Residual kinetic energy of the fragment.

The residual kinetic energy can be further defined as:

$$E_R = E_{DR} + E_F + E_{TR} \tag{2.2}$$

where

E_{DR}= Deformation strain energy of the rear plate.

E_F Friction energy when the fragment is welded to the back face.

E_{TR}= Energy required for the tearing of the back plate.

However, no attempt was made to evaluate any of the unknowns in Equations 2.1 and 2.2. The velocity of the fragment was never measured directly although the residual

impulse of the fragment hitting the rear face of the tube was evaluated. The fragment impulse was referred to as the residual impulse and is defined as:

$$\text{residual impulse} = \text{total impulse} - \text{critical impulse} \tag{2.3}$$

where the total impulse is the impulse measured for the experiment and the critical impulse is the maximum impulse before full tearing occurs.

Nurick [3] reported that for blast loaded plates of particular geometries, the mid-point deflection can be expressed in terms of a dimensionless impulse as:

$$\frac{\delta}{t} = K\phi \tag{2.4}$$

where δ is the maximum midpoint deflection, t is the plate thickness, K is the geometric constant and ϕ is the dimensionless impulse. The dimensionless impulse is given by the equation:

$$\phi = \frac{I(2 + \ln \frac{R}{R_0})}{\pi R t^2 (\rho\sigma_0)^{\frac{1}{2}}} = \text{dimensionless impulse for circular plates} \tag{2.5}$$

$$\phi = \frac{I}{\pi t^2 (BL\rho\sigma_0)^{\frac{1}{2}}} = \text{dimensionless impulse for rectangular plates} \tag{2.6}$$

where I is the total applied impulse, R is the plate radius, B is the plate width, L is the plate length, R_0 is the loading radius, ρ is the material density and σ_0 is the static yield stress.

The front plate geometry of the square tubes was assumed to be a rectangular plate fixed along two boundaries with a circular concentrated load resulting in the equation:

$$\phi = \frac{I(1 + \ln \frac{w}{R_0})}{\pi w t^2 (\rho\sigma_0)^{\frac{1}{2}}} = \text{dimensionless impulse for the square tubing} \tag{2.7}$$

where w is the half width of the tube. All the impulses can be converted to dimensionless impulses using Equation 2.7 and Equation 2.3 can now be written in dimensionless form:

$$\text{residual dimensionless impulse} = \text{total dimensionless impulse} - \text{critical dimensionless impulse} \tag{2.8}$$

2.2 BLAST EXPLOSION ON THIN BUILT-IN CIRCULAR PLATES

The response of thin plates subject to various blast loading conditions has been studied for many years. Menkes and Opat [4] defined three failure modes for beams subject to impulsive loads:

Mode I : Large inelastic deformation.

Mode II : Tensile tearing at the edges.

Mode III : Transverse shear failure at the edges.

The failure modes are also observed in circular plates subjected to uniform blast loads [5] and for square plates [6]. However, when thin circular plates are subjected to localized blast loads the following additional failure modes have been identified (see Refs. 7] and [8]):

Mode Itc : Large inelastic response with thinning in the central area.

Mode $II*c$: Partial tearing in the central area.

Mode IIc : Complete tearing in the central area.

Mode IIc can result in the formation of a single circular fragment from the centre of the plate under specific load conditions. This phenomenon is known as capping and the circular fragment is referred to as a cap. The fragment is almost perfectly circular

Table 2.1: FRACTURE RESULTS OF THIN CIRCULAR BUILT-IN PLATES

Plate Thickness	Explosive Diameter		
	25 mm	33 mm	40 mm
1.6 mm	Capping or Petalling	Capping and/or boundary tearing	Capping and/or boundary shearing
2.6 mm	Capping or Petalling	Capping	Capping and/or boundary shearing
3.6 mm	-	Petalling and boundary tearing	Boundary shearing

and little petalling occurs around the fragment edge. The symmetry of the fragment makes capping an ideal condition to analyse the tearing mechanism of plates due to blast loads.

Chung Kim Yuen [8] performed an extensive series of experiments using built-in circular plates with a diameter of 100 mm and thicknesses of 1.6, 2.6 and 3.6 mm subjected to explosive loads with diameters of 25, 33 and 40 mm. Low intensity blast loads resulted in plastic deformation (mode *I* and *IIc*) while larger impulses resulted in tearing of the plate (mode *II*). The exact nature of the mode *II* tearing depended on the plate thickness, explosive diameter and the explosive mass. The failure results are summarized in Table 2.1. The 1.6 mm plates resulted in capping for an explosive diameters of 25 mm. For explosive diameters of 33 mm and 40 mm the plates capped and/or tore/sheared at the boundary. The 2.6 mm plates capped for load diameters of 25 mm and 33 mm. For load diameters of 40 mm the plates capped and/or tore/sheared at the boundary. Large impulses often resulted in petalling occurring instead of capping for the 1.6 mm and 2.6 mm plates. The 3.6 mm plates did not cap but they were subjected to a combination of petalling and/or failure at the boundary.

2.3 MODELLING EXPLOSIVE BLASTS

There are two different methods of modelling a blast wave using the finite element code ABAQUS/Explicit. The first method involves modelling the blast wave as an applied pressure over a given area for a given time. The second method involves modelling the explosive using the Jones-Wilkins-Lee (JWL) equation of state (EOS).

2.3.1 APPLYING PRESSURE TO MODEL THE EXPLOSION

Numerous people have used this method for modeling blast-loaded plates including Bimha [9], Gelman [10], Farrow [11] and Grobbelaar [12]. Bimha modelled thin circular clamped plates that were subjected to centrally positioned disks of explosive while Refs [10] and [11] applied a uniform pressure to the entire plate area.

The basic theory of the modelling is relating the impulse imparted on the specimen (which is measured on a ballistic pendulum) to a pressure-time distribution. For an axisymmetric model, the relationship is given by the equation:

$$I = \int_0^{\infty} \int_0^{R} P(r) dA dt \tag{2.9}$$

where

$P(r)$ is the pressure of the blast as a function of radius r from the specimens centre to the specimens edge R.

A is the area of the specimen where the blast wave is applied.

t is the time the pressure is applied to the plate.

The exact nature of the pressure wave is very complex. However, it is possible to approximate the pressure distribution and obtain reasonable finite element solutions.

Binnha [9] approximated the pressure distribution as a constant pressure over the area of the explosive with an exponential decay over the rest of the plate. The pressure distribution is given as:

$$\begin{aligned} P(r) &= P_0 \qquad \text{for} \quad r \leq R_0 \\ P(r) &= P_0 e^{-k(r-R_0)} \quad \text{for} \quad R_0 < r < R \end{aligned} \tag{2.10}$$

where P_0 is the pressure magnitude and k is the exponential decay. Substituting Equation 2.10 into Equation 2.9 results in:

$$I = \pi t P_0 \left[R_0^2 + 2 \left\{ \left(\frac{R_0}{k} + \frac{1}{k^2} \right) - \left(\frac{R}{k} + \frac{1}{k^2} \right) e^{k(R_0 - R)} \right\} \right] \tag{2.11}$$

Solving for P_0 gives:

$$P_0 = \frac{I}{\pi t \left[R_0^2 + 2 \left\{ \left(\frac{R_0}{k} + \frac{1}{k^2} \right) - \left(\frac{R}{k} + \frac{1}{k^2} \right) e^{k(R_0 - R)} \right\} \right]} \tag{2.12}$$

The time the blast is applied to the plate is referred to as the blast duration. The blast duration is approximated by the burn time of the explosive:

$$t_{bd} = \frac{R_0}{V_b} \tag{2.13}$$

where t_{bd} is the blast duration and V_b is the burn speed of the explosive.

The value of the exponential decay was given by the empirical equation:

$$k = 130 - 261 \frac{R_0}{R} + 948 \left(\frac{R_0}{R} \right)^2 \quad \text{for the range} \quad 0.15 < \frac{R_0}{R} < 0.6 \tag{2.14}$$

2.3.2 USING THE EQUATION OF STATE

The use of the JWL equation of state allows the modelling of the explosive directly. The explosive is modelled by assigned JWL equation of state material properties to

the elements that represent the explosive. The explosive is then detonated at one or more detonation points in the explosive.

Only two reports could be found in the literature in which the use of the JWL EOS with ABAQUS Explicit has been discussed. The first example was in the ABAQUS Explicit Example Problems Manual [13] and the second by Grobbelaar [14].

THEORY OF THE JWL EQUATION OF STATE

The JWL EOS models the pressure generated by the release of chemical energy in an explosive. The equation can be written in terms of the initial energy per unit mass, E_{m0}:

$$p = A\left(1 - \frac{\omega\rho_0}{R_1\rho_0}\right)\exp\left(-R_1\frac{\rho_0}{\rho}\right) + B\left(1 - \frac{\omega\rho}{R_2\rho_0}\right)\exp\left(-R_2\frac{\rho_0}{\rho}\right) + \frac{\omega\rho^2}{\rho_0}E_{m0} \quad (2.15)$$

where A, B, R_1, R_2 and ω are material constants that must be defined, p is the pressure and ρ is the explosive density.

The arrival time of the detonation wave, at a particular material point, is determined by the distance between the material point and the nearest detonation point divided by the detonation speed. A burn fraction is then computed that spreads the detonation wave over several elements.

EXAMPLE IN THE ABAQUS MANUAL

The example in the ABAQUS Explicit Example Problems Manual [13] consists of two concentric steel pipes that have the annulus between them filled with high explosive. The explosive material is detonated at four points around the circumference of the cylinder in both a two-dimensional and three-dimensional model. Due to the symmetry of the problem, only one-eighth of the pipe is modelled. A diagram of the two-dimensional case is shown in Figure 2.1. The interaction between the explosive and the steel is through common nodes between the explosive and steel elements.

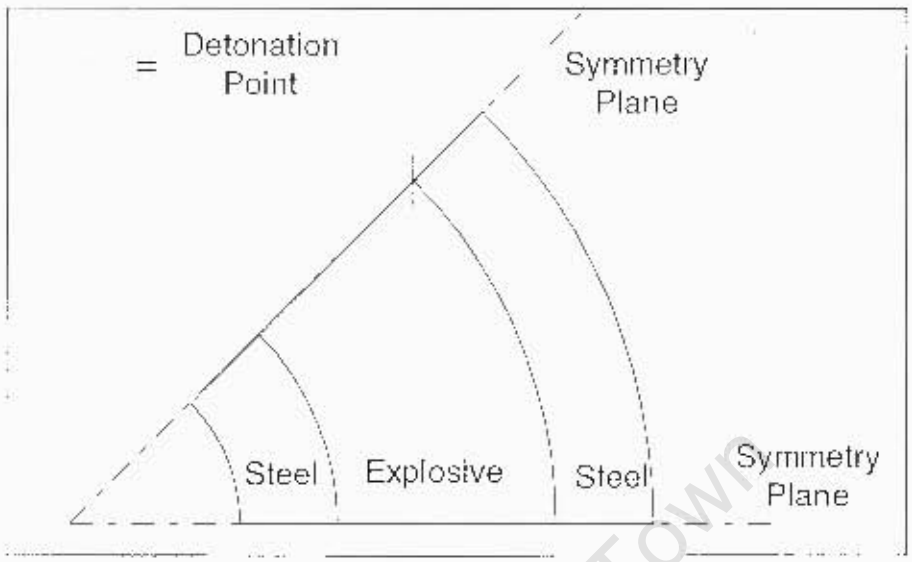

Figure 2.1: JWL Equation of State Example Given in the ABAQUS Manual.

AS USED BY GROBBELAAR

Grobbelaar [14] was able to use the equation of state to successfully model the deformation of Radford's [15] clamped circular plates. The explosive was modelled using normal axisymmetric or 3D continuum elements that are then given an EOS material property. Contact boundary conditions are then imposed between the explosive outer surface and the plate. The EOS is then given a detonation point in the middle of the explosive. A diagram of the explosive setup as used by Grobbelaar is given in Figure 2.2.

Grobbelaar established the use of contact with the EOS using ABAQUS at the University of Cape Town. He concluded that the JWL enabled reasonably accurate modelling of explosive blasts and eliminated the uncertainties associated with guessing the pressure time distribution. It was noted that the method uses a force based contact algorithm that treats the explosive and material as two different solids as opposed to a shock-to-shock interaction that occurs between a gas and a solid.

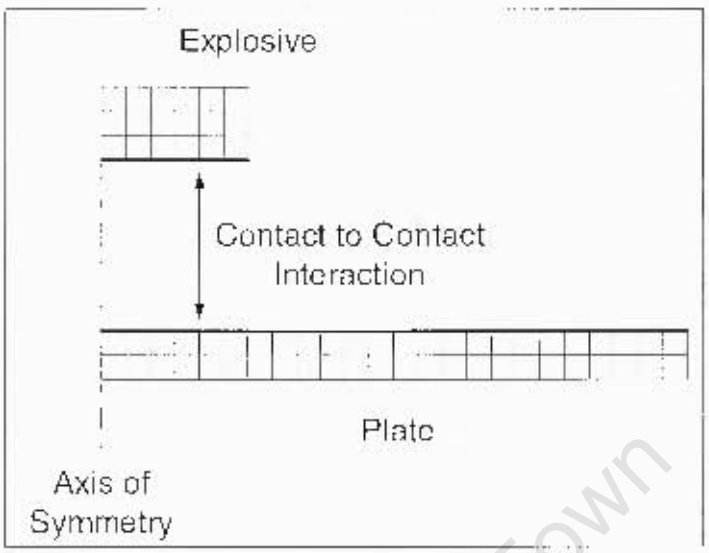

Figure 2.2: The JWL Equation of State as Used by Grobbelaar.

2.4 MODELLING THE MATERIAL PROPERTIES

Blast loading results in excessive plastic deformation at high strain rates and high temperatures. Material model development and obtaining material properties at high strain rates and temperatures is still an ongoing process in research. This section shall discuss the material models and the failure prediction methods that are available for modelling metals at high strain rates in ABAQUS/Explicit [16]. Two different material models are available for modelling metals, namely:

- The classical metal plasticity model as referred to in [16].
- The Johnson-Cook plasticity model.

2.4.1 CLASSICAL METAL PLASTICITY

Classical metal plasticity involves obtaining stress-strain data from uniaxial tensile tests and then modifying the stress for strain rate and temperature dependencies if

required.

STRAIN HARDENING

The elastic region is described by the Young's modulus. However, for the plastic region, true stress and logarithmic plastic strain data is required. For an isotropic material, nominal stress-strain data can be determined from uniaxial tests. This can then be converted to true stress and logarithmic plastic strain by the equations in Ref. [16]:

$$\sigma_{true} = \sigma_{norm}(1 + \varepsilon_{norm}) \tag{2.16}$$

$$\varepsilon_{\ln}^{pl} = \ln(1 + \varepsilon_{norm}) - \frac{\sigma_{true}}{E} \tag{2.17}$$

where σ_{true} is the true stress, σ_{norm} is the nominal stress, ε_{norm} is the nominal strain, $\varepsilon_{\ln}^{pl}$ is the logarithmic plastic strain and E is the Young's modulus.

RATE DEPENDENCE

As strain rate increases, most metals show an increase in yield stress. This can be entered in tabular form or the Cowper-Symonds equation can be used. The Cowper-Symonds equation is defined [16] as:

$$\dot{\bar{\varepsilon}}^{pl} = D\left(\frac{\sigma}{\sigma_0} - 1\right)^n \tag{2.18}$$

where $\dot{\bar{\varepsilon}}^{pl}$ is the equivalent plastic strain rate, σ_0 is the static stress and σ is the dynamic stress, D and n are material constants.

TEMPERATURE DEPENDENCE

Plastic work results in heat generation causing the degradation of material properties. This option is typically used in simulation of bulk metal forming [17]. It appears that this has yet to be applied to the blast simulation of thin circular plates.

ABAQUS/Explicit allows adiabatic stress analysis to be performed where heat is generated by plastic strain. The resulting temperature rise is then computed using the specific heat of the metal. The Young's modulus and the true stress - logarithmic plastic strain data can be entered in tabular form for different temperatures. ABAQUS will determine the exact Young's modulus and logarithmic plastic strain by linearly interpolating between the tabulated values.

2.4.2 JOHNSON-COOK PLASTICITY MODEL

The Johnson-Cook plasticity model is an empirical equation that was developed for high-strain-rate deformation of most metals. It is typically used in adiabatic transient dynamic simulations.

The model is given by the equation:

$$\bar{\sigma} = \left[A + B\left(\bar{\varepsilon}^{pl}\right)^{n}\right]\left[1 + C\ln\left(\frac{\dot{\bar{\varepsilon}}^{pl}}{\dot{\varepsilon}_0}\right)\right]\left(1 - \hat{\theta}^{m}\right) \tag{2.19}$$

where

$\bar{\sigma}$ is the yield stress at a given temperature and strain rate.

$\hat{\theta}$ is the non-dimensional temperature.

A, B, C, n and m are material properties.

The non-dimensional temperature is defined as:

$$\hat{\theta} = \begin{cases} 0 & \text{for} \quad \theta < \theta_{transitional} \\ \frac{\theta - \theta_{transitional}}{\theta_{melt} - \theta_{transitional}} & \text{for} \quad \theta_{transitional} < \theta < \theta_{melt} \\ 1 & \text{for} \quad \theta \geq \theta_{melt} \end{cases} \tag{2.20}$$

where θ is the current material temperature, θ_{melt} is the melting temperature of the metal and $\theta_{transitional}$ is the transitional temperature at which A and B were chosen. Unfortunately determining the material properties for the Johnson-Cook plasticity model is not an easy task due to the difficulties of testing the material properties

at the high strain rates and temperatures. Most modellers use materials that already have had their material properties published in the literature.

2.4.3 FAILURE CRITERIA

For the classical metal plasticity and the Johnson-Cook plasticity model, both a shear and tensile failure criterion are available. The shear failure model is based on the value of the equivalent plastic strain, while the tensile failure model is based on the value of a hydrostatic pressure stress. Both failure methods are applicable to high-strain-rate problems.

Shear Failure Criteria

The shear failure predicts failure when the damage parameter exceeds unity. The damage parameter is defined as:

$$\omega = \sum \left(\frac{\Delta \bar{\varepsilon}^{pl}}{\bar{\varepsilon}_f^{pl}} \right) \tag{2.21}$$

where $\Delta \bar{\varepsilon}^{pl}$ is an increment of the equivalent plastic strain, $\bar{\varepsilon}_f^{pl}$ is the equivalent plastic failure strain and the summation is performed over all increments of the analysis.

For the classical plasticity model the equivalent plastic strain can be given in tabular form as a function of the equivalent plastic strain rate, a dimensionless pressure-deviatoric stress ratio, the temperature and other predefined field variables. The Johnson-Cook shear failure criteria modify the equivalent plastic failure strain with the following equation:

$$\bar{\varepsilon}_f^{pl} = \left[d_1 + d_2 \exp\left(d_3 \frac{p}{q} \right) \right] \left[1 + d_4 \ln\left(\frac{\dot{\bar{\varepsilon}}^{pl}}{\dot{\varepsilon}_0} \right) \right] \left(1 + d_5 \hat{\theta} \right) \tag{2.22}$$

where d_2 to d_5 are failure parameters associated with the stress state, the strain rate and temperature dependence.

The failed elements can either be deleted by setting the material properties to zero, or the elements will only support a compressive pressure stress.

Tensile Failure Criteria

The tensile failure criteria assumes that failure occurs when the pressure stress becomes more tensile then the specified hydrostatic cutoff stress. The hydrostatic cutoff stress can be entered as a function of temperature and other predefined fields. The failed elements can either be removed or subjected to various spall models. The different spall models have the options of allowing the deviatoric stress components to be unaffected or equal to zero, and the pressure stress may be limited by the hydrostatic cutoff stress or may be required to be compressive.

2.5 FORMATION AND MODELLING OF SHEAR BANDS

Heat generated by plastic strain at high strain rates has little or no time to flow to neighbouring regions, resulting in a deformation process that is essentially adiabatic. The localized heat generation and temperature increase result in the region being subjected to both strain-hardening and thermal softening. Consequently, if the thermal-softening rate overcomes the strain-hardening rate, the flow stress will decrease with strain, resulting in a convex stress-strain curve with a maximum flow stress separating the hardening and softening regimes. This localization strain usually manifests itself in the form of shear bands, with measured widths typically of $5 - 100\,\mu$m and strains of $5 - 100\%$ [18]. The corresponding strain rate in the formed shear band is estimated to be between $10^4$and $10^6\,s^{-1}$, and the temperature rise in the shear band is estimated

to be several hundred degrees Celsius [19]. The method of failure of many metals subjected to high strain rates is sometimes attributed to the formation of shear bands and they are generally considered to be a percussor to fracture [20] and [21].

Adiabatic shear bands have been studied extensively in recent years, e.g. [18], [19], [20], [21], [22], [23], [24], [25], [26], [27], [28], [29] and [30]. These shear bands play a role in many diverse areas with high strain rates such as ballistic impact, high-speed forming and shaping, machining and explosive fragmentation. The study of shear bands has been analysed primarily experimentally allowing the development of analytical theories. The main methods used to generate the shear bands experimentally include: explosively loaded cylinders [24], high speed machining tests [27], dynamic torsion tests and dynamic impact tests [20]. More recently the problem has been analysed using numerical simulation.

Irick et al.[20] modelled the formation of shear bands under low velocity impact conditions. The numerical analysis was done on a finite element hydrocode, DYNA, incorporating the Johnson-Cook constitutive equation. It was concluded that it was possible to quantitatively and realistically model adiabatic shear bands for a range of materials (OFCH-Copper, S-7 tool steel and tungsten alloy).

Zhou et al.[26] carried out impact load experiments on pre-notched plates observing maximum temperatures of $1400°C$ or approximately 90 % of the melting point of the C 300 steel. High speed photography was used to measure the speed of the shear bands giving a maximum velocity of $1200\,m\,s^{-1}$. Subsequent finite element analysis [31] showed good agreement with the experimental work in all areas - namely temperature fields, shear band width and shear band propagation speed. The numerical analysis included temperature dependent material properties and a strain based damage failure model. Once an element fails, it is modelled as a viscous fluid. The use of the constitutive model for material based inside the shear band is motivated by the materials' ability to sustain pressure, by the continued dissipation through deformation and frictional forces and by the high temperature values observed in the experiments. Unfortunately, mesh density details were not given.

Pastor et al.[25] investigated the effect of mesh density and mesh alignment on the

formation of shear bands. They concluded that capturing shear bands requires a mesh size small enough to provide the required resolution. Wider elements result in the shear bands being diffused over several elements widths resulting in ductile behaviour while further mesh refinement will result in the shear band width approaching zero. The choice of element plays a critical role as locking, poor bending performance or poor behaviour under quasi isochoric conditions decrease the band definition and cause a stiffer behaviour. The alignment of 3 (first order), 6 (second order) and 15 (third order) noded triangular elements were investigated resulting in different solutions for different mesh alignment. Triangular elements of high order, such as the cubic strain triangle are much less influenced by mesh alignment than lower order constant strain triangles. However, the best definition and accuracy with which the shear band is computed, is for second order elements providing the triangle sides are conveniently aligned following the shear band. The use of adaptive remeshing was proposed where the mesh would be progressively refined in the region of the shear band until the mesh density reached 1/3 the width of the known shear band.

Various analytical model have been developed to simulate the formation and spacing of shear bands by various researchers e.g.[21], [23] and [28]. Wang [29] investigates various instabilities in metals including shear bands. In order to prevent mesh dependence, the use of two characteristic material length scales were used in the evolution of the shear band. The first length scale depends on both the viscosity parameter and the softening /hardening parameter. The second length scale is introduced by coupling second-order strain gradients to the yield surface. Numerical analysis with the model showed that the width of the shear band is dominated by the larger of the two length scales.

Chapter 3

EXPERIMENTAL DATA

Although experimental work has been undertaken on circular built-in plates subjected to localized blast loads [7] and [8], the velocity of the fragment has not been measured. Experimental tests were undertaken with the aim of determining the fragment velocity, the critical impulse to cause capping and obtaining uncapped specimens to calibrate the numerical model. This chapter explains the experimental procedure and then comments on the results of the experimentation.

3.1 EXPERIMENTAL PROCEDURE

The method of creating an impulsive load using plastic explosive and the measurement of the impulse is the same as used by Radford [15].

A description of the method of creating the blast followed by a detailed description of the apparatus used during the experimentation will be given in this section.

A list of the apparatus used during the experimentation is listed below:

- The test specimens.
- The ballistic pendulum.
- The velocity-measuring device.

3.1.1 METHOD OF CREATING THE BLAST

The plates were centrally loaded using plastic explosive (PE4). The explosive was spread evenly over a diameter of 25 mm on to the centre of a polystyrene pad. A detonator, with one gram of explosive, was then attached perpendicular to the centre of the explosive disk. The polystyrene pad has a diameter of 100 mm and a thickness of 12 mm. It was then attached to the centre of the blast specimen. A diagram of the explosive loading is shown in Figure 3.1. The polystyrene prevents spallation of the test specimen.

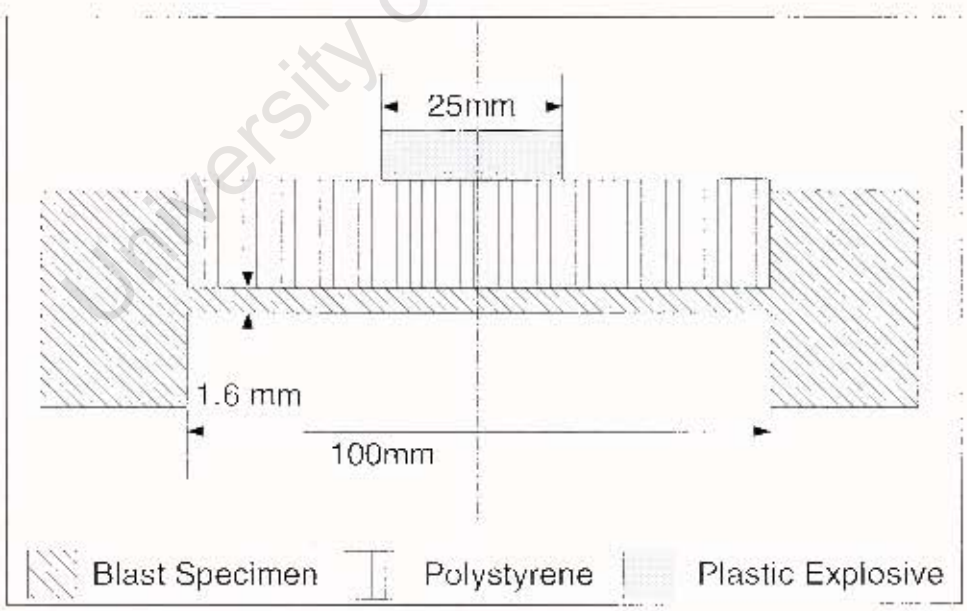

Figure 3.1: The Explosive Setup.

3.1.2 THE TEST PLATES

The built-in test plates are the same as used by Chung Kim Yuen [8]. They are made from a 200 mm mild steel square plate with a thickness of 20 mm that have 100 mm disks machined out of either side of the plate leaving a circular region with a thickness of about 1.6 mm. The specimens are then heat treated to relieve the internal stress caused by the machining process. The plates are fastened on to a ballistic pendulum by means of four bolts. A diagram of the plate is shown in Figure 3.2. In order to take into account the variable thickness of the plate, the thickness of the circular section was measured at different places and the average thickness recorded.

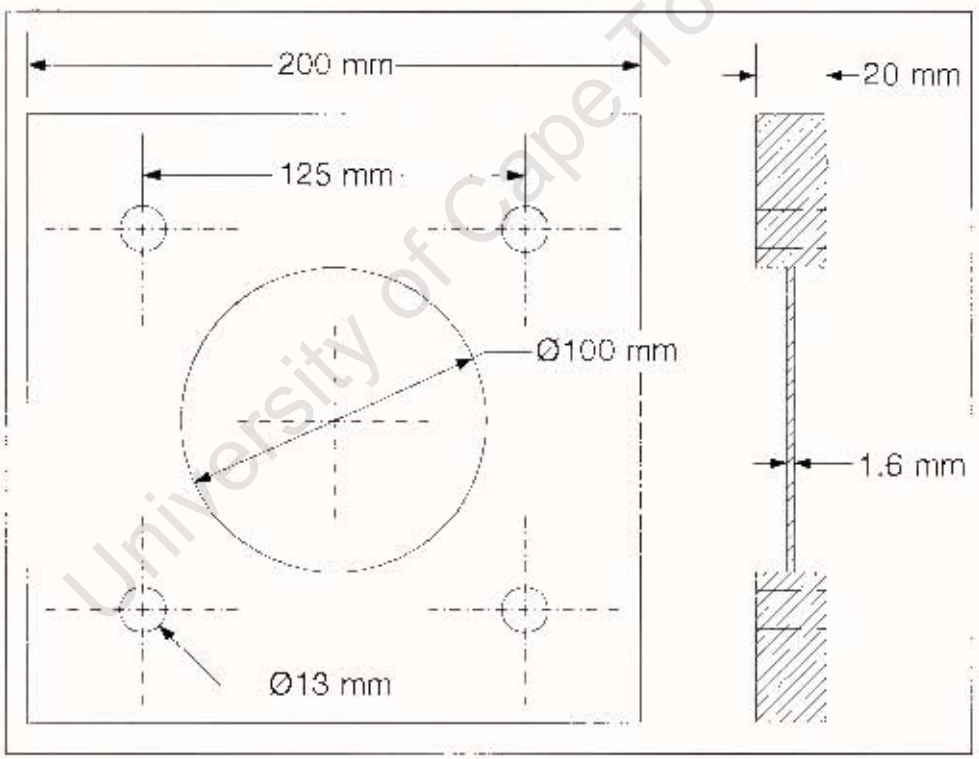

Figure 3.2: Test Specimen Dimensions.

3.1.3 THE BALLISTIC PENDULUM

The ballistic pendulum is used to measure the impulse of the explosive blast on the test specimen. The pendulum hangs from the ceiling by four wire ropes as seen in Figure 3.3. A pen that is attached to the back of the pendulum records the oscillation amplitudes of the pendulum. Before each blast the pendulum must be balanced so that the centroid of the pendulum is in the middle of the four wires by the use of balancing masses. The tension in the wires must be even and are adjusted by the use of adjustable screws. This is to ensure a constant straight swing that can be used to measure the impulse of the blast from the oscillation amplitudes. The method of determining the impulse is explained in Appendix A.

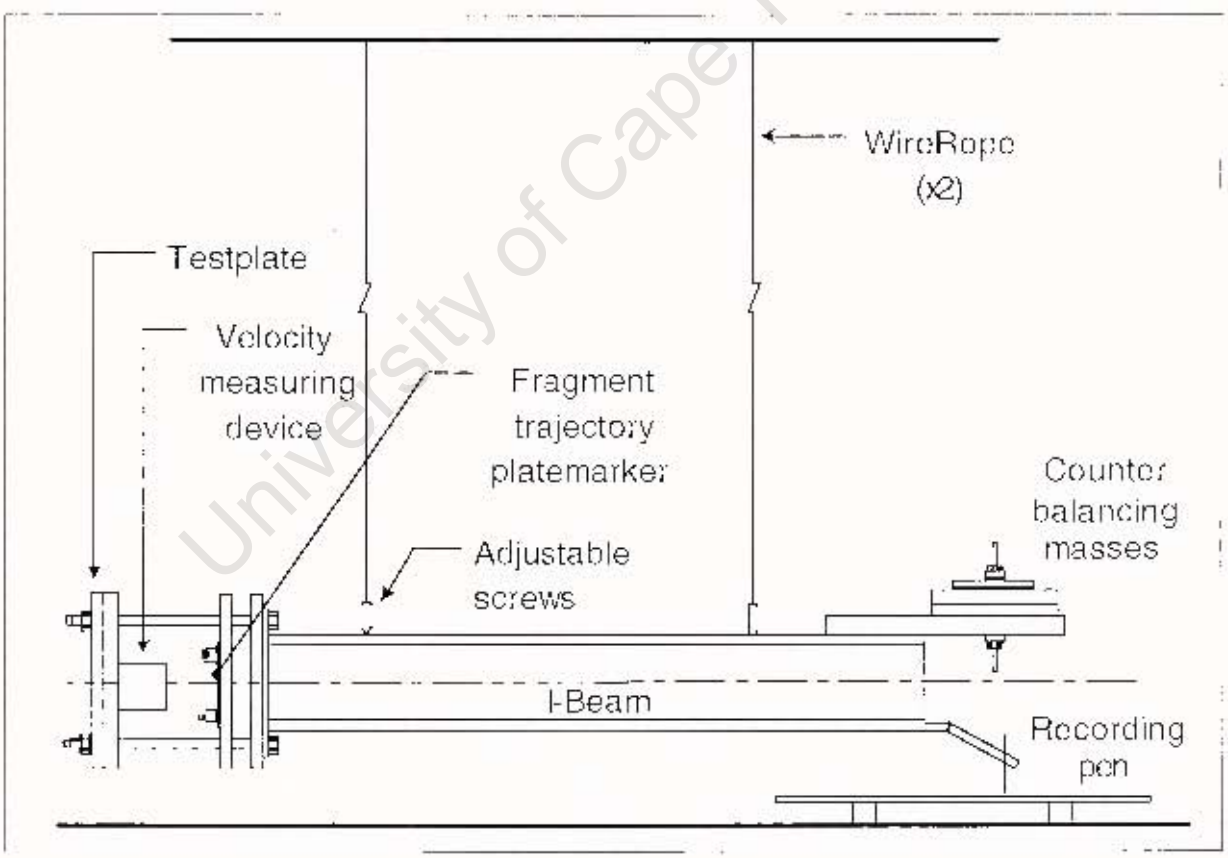

Figure 3.3: A Diagram of the Blast Pendulum.

3.1.4 THE VELOCITY MEASURING DEVICE

A velocity-measuring device using a system of wires, similar to that used by Nurick and Shave [6], is used to measure the speed of any fragment that may result from an explosive test. The device can be seen in Figure 3.4. It consists of four steel wires that are spaced 30 mm apart in the path of the fragment. A 12 volt current is passed through each of the wires. When the fragment breaks a wire, the voltage in the wire drops to zero. The voltage time history of all four wires is recorded on an oscilloscope enabling the fragment displacement time history to be recorded. The fragments velocity in the direction of the wires is calculated from the gradient of a best fit line through the fragments displacement-time graph. The trajectory of the fragment is recorded when the fragment hits a thin plate that plastically deforms marking the path of the fragment. The total fragment velocity can then be calculated using the fragment trajectory.

It should be noted that the velocity-measuring device is not able to measure any possible rotational velocity the fragment may have. Four wires have been used to determine the consistency of the system.

3.2 EXPERIMENTAL RESULTS

A series of explosions were undertaken for 1.6 mm plates subjected to plastic explosive. The explosive results ranged from plastic deformation to severe catastrophic failure. The experimental results are given in Appendix B. Some of the plates were subjected to severe plastic deformation (see Figures 3.5 and 3.6), while larger impulses resulted in capping (see Figure 3.7) and even larger impulses resulted in catastrophic failure of the central region.

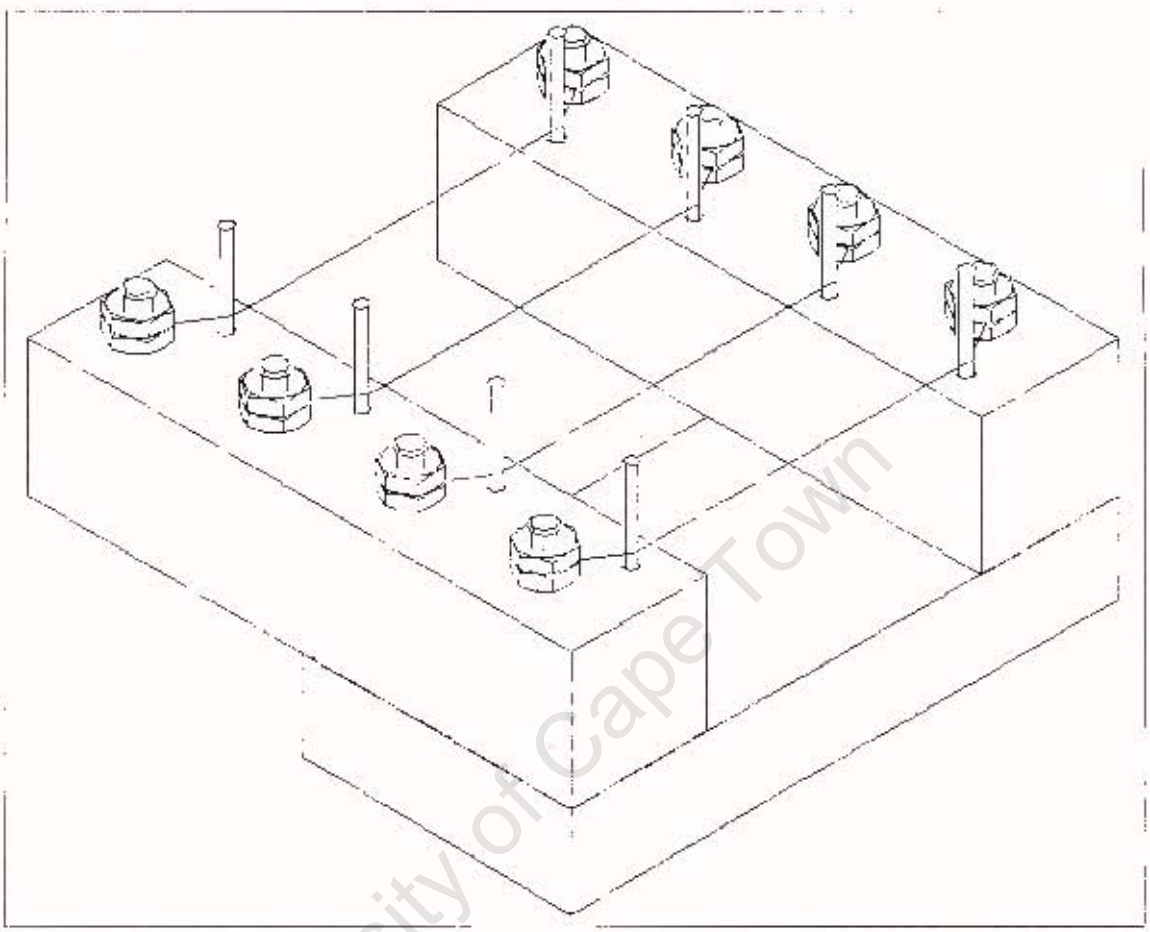

Figure 3.4: A Diagram of the Velocity Measuring Device.

3.2.1 FRAGMENT VELOCITY

A total of eleven tests were undertaken where the plate was subjected to the capping phenomenon. The wire velocity measuring device was used for seven of these tests, resulting in five velocity readings since the fragment missed the wires on two occasions. The displacement time graph of the fragments as recorded by the velocity measuring device is given in Figure 3.8. Appendix C contains the raw data. The cap velocity is given by the gradient of the best fit linear line through the data points. The high correlation coefficients of the best fit lines gives a high sense of confidence that the system works consistently. The recorded cap velocities are given in Table 3.1. The

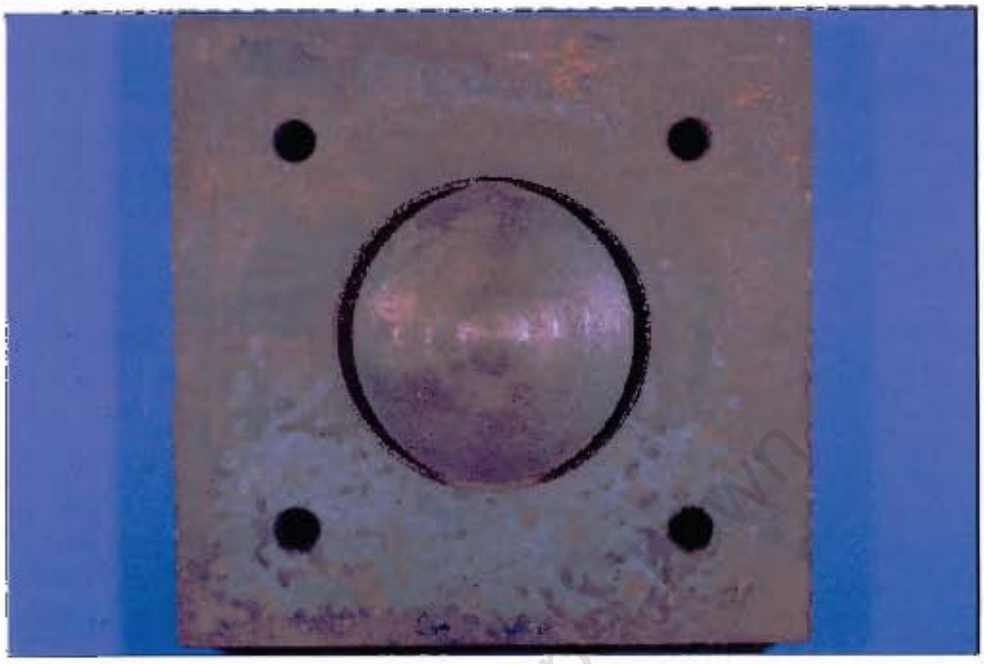

Figure 3.5: A Top View of a Plastically Deformed Plate.

Figure 3.6: Oblique View of a Plastically Deformed Plate.

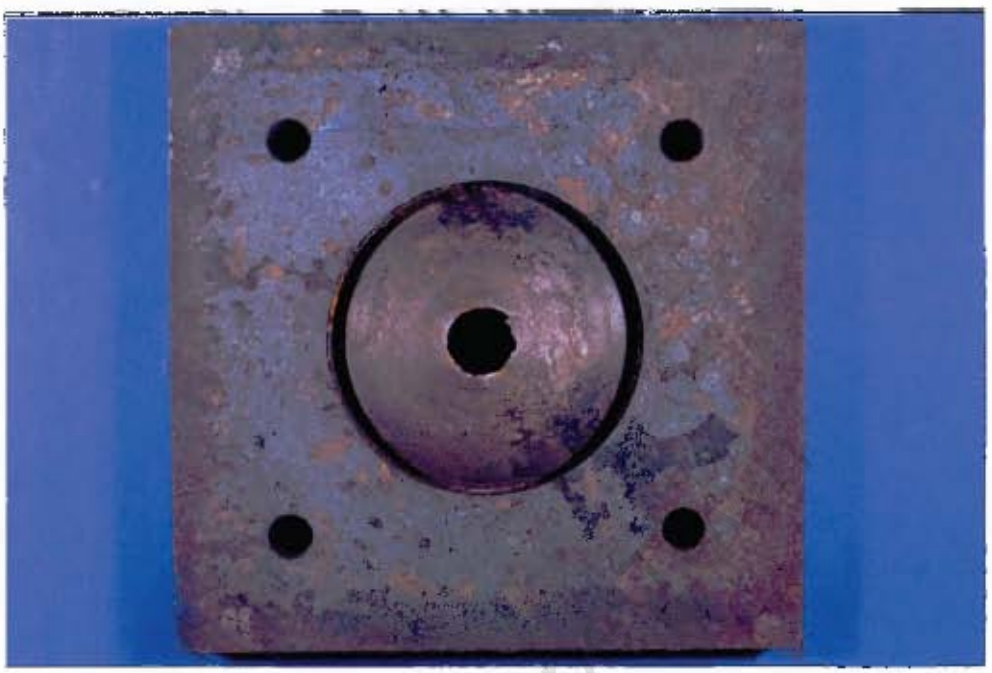

Figure 3.7: A Top View of a Capped Plate.

fragment velocity was recorded at a maximum of 403 $\mathrm{m\,s^{-1}}$ and a minimum of 282 $\mathrm{m\,s^{-1}}$. The fragment diameter, determined by a mass balance, varied from 8.0 to 9.6 mm.

3.2.2 THE CRITICAL IMPULSE THAT RESULTS IN FRACTURE

A list of the method of fracture in increasing dimensionless impulse is given in Table 3.2. The dimensionless impulse for circular plates is given by Equation 2.5 and the constants used for the equation are R=0.05 m, R_0=0.0125 m, ρ=7890 kg/m^3 and σ_0=200 MPa. The largest dimensionless impulse not to result in fracture is 35.2 and the largest dimensionless impulse not to result in capping is 39.8. Between the two mentioned dimensionless impulses, one capped plate, one slightly fractured plate and one plastically deformed plate occurred. Test $T14$, subjected to a dimensionless impulse

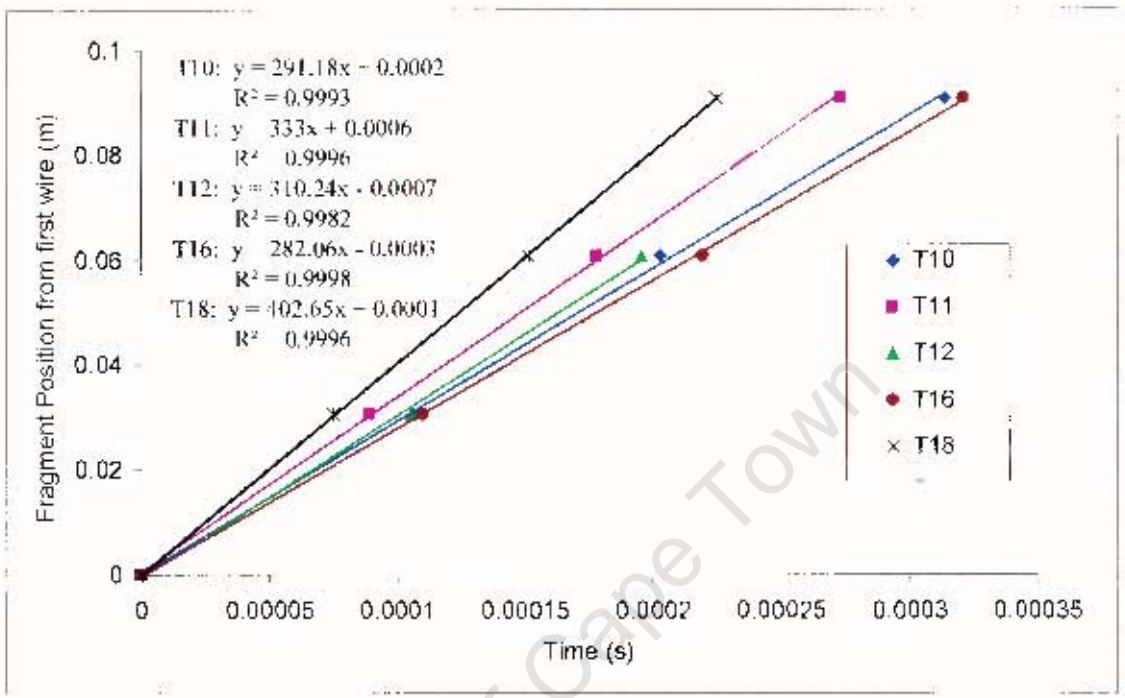

Figure 3.8: Fragment Position Time History.

Table 3.1: EXPERIMENTALLY MEASURED FRAGMENT VELOCITIES

Test No	Plate Thickness (mm)	Impulse (N · s)	Fragment Diameter (mm)	Fragment Velocity (m / s)	Correlation Coefficient
T10	1.75	10.44	9.3	295.1	0.9993
T11	1.55	8.95	9.6	333.2	0.9996
T12	1.83	10.88	8.0	310.2	0.9982
T16	1.8	11.21	9.4	282.3	0.9998
T18	1.73	11.94	9.3	402.9	0.9996

of 34.7, (see Figure 3.9) resulted in extensive tearing at the location of cap formation almost resulting in the formation of a cap. Overall one can conclude that the dimensionless critical impulse occurs in the region of 34 - 40.

Figure 3.9: 80 % Tearing in the Region of Capping.

3.2.3 OBSERVATION ABOUT THE FRACTURE SURFACE

Closer examination of the fractured surface resulted in observing a sheared surface at angles of either 45° or 135° relative to the midplane of the deformed plate (see Figure 3.10). This angle can be constant for most of the cap at an angle of either 45° (see Figure 3.11) or 135° (see Figure 3.12) or it can be at either angle for different segments in a random manner (see Figures 3.10 and 3.13). It appears as though the angle of fracture may be affected by the microstructure of the specimen in the immediate vicinity of the cap.

Table 3.2: FRACTURE RESULTS OF THE EXPERIMENTAL TESTS

Test No	Dimensionless Impulse $N \cdot s / m^2$	Fracture Details
T4	3.63	No fracture
T7	26.8	No fracture
T5	30.9	No fracture
T6	31.1	No fracture
T14	34.7	Hanging (Figure 3.11)
T13	35.2	No fracture
T15	39.1	Slight fracture
T12	39.3	Capped
T19	39.8	No fracture
T9	40.0	Capped
T10	41.2	Capped
T16	41.8	Capped
T21	43.1	Capped
T3	43.2	Capped
T20	44.9	Capped
T11	45.1	Capped
T17	46.1	Capped
T18	48.4	Capped
T2	53.8	Capped
T1	63.1	Petalling

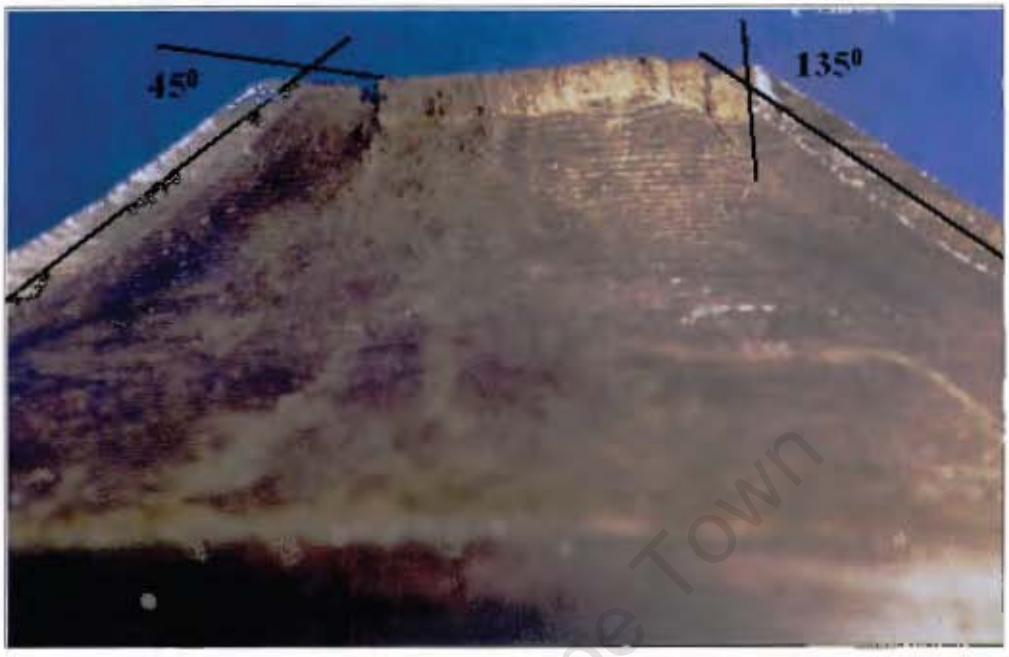

Figure 3.10: Plate Cross Section Showing the Different Angles of Fracture.

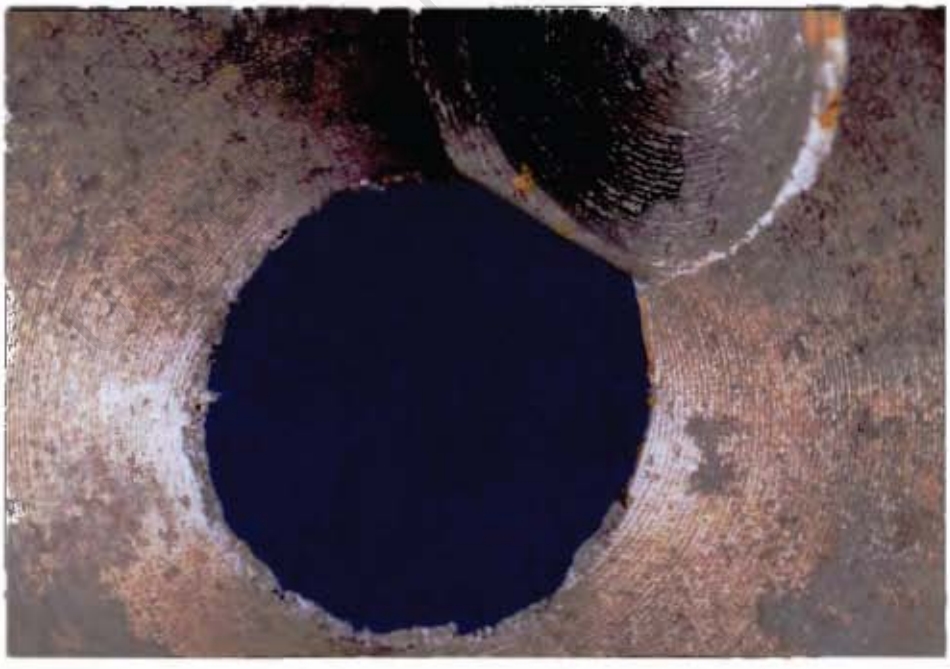

Figure 3.11: A Plate with an Angle of Fracture Mainly of 45^0.

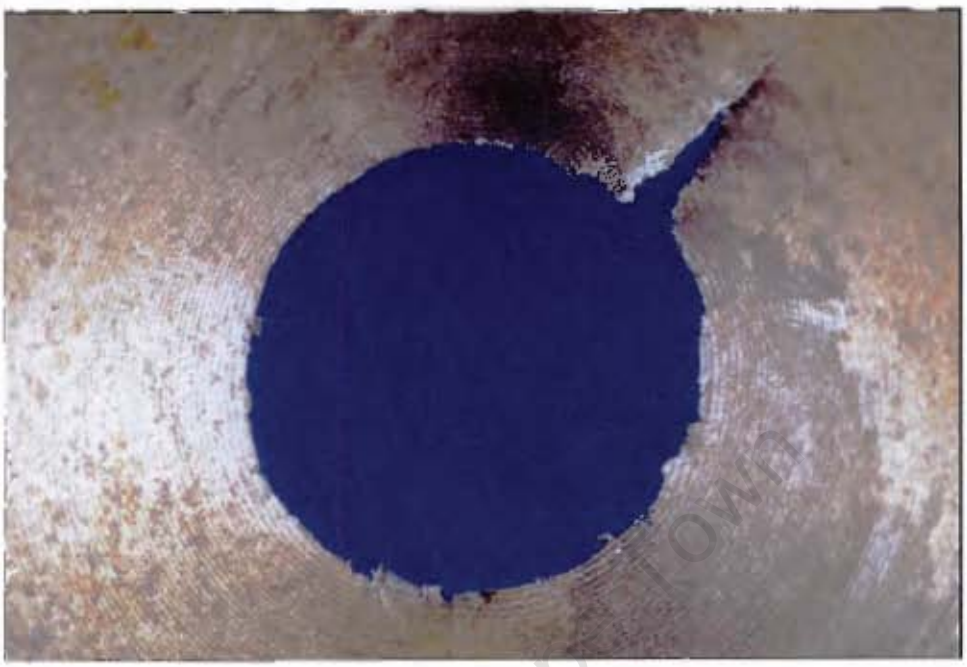

Figure 3.12: A Plate with a Fracture Angle of Mainly 135^0.

Figure 3.13: A Plate with an Angle of Fracture of 45^0 and 135^0 to the Deformed Plate.

Chapter 4

METHOD OF FINITE ELEMENT MODELLING

This section is intended to introduce the reader to the finite element method and to explain the method of modelling plates subjected to a blast load using finite elements. The results of the finite element models are presented in Chapter 5.

4.1 FINITE ELEMENT ANALYSIS PROCEDURE

The finite element package used is ABAQUS/Explicit which is well suited to solving non-linear high-speed dynamic events. The code uses an explicit time integration scheme, with a central difference rule, to integrate the equations of motion using the kinematic conditions at one increment to calculate kinematic conditions at the next increment. The state of the model is advanced through an increment in time based on the state of the model at the start of the increment. At the start of each increment the program solves dynamic equilibrium for the equation:

$$M\ddot{u} = P - I \tag{4.1}$$

where M is the mass matrix, $\ddot{u}$ is the nodal accelerations, P is the external applied forces and I is the internal element forces.

The stable time limit is based on the highest frequency in the system, and based on an element-by-element estimate it can be approximated as:

$$\Delta t_{stable} = L^e / c_d \tag{4.2}$$

where L^e is the element length and c_d is the wave speed of the material.

ABAQUS/Explicit chooses the time increment to be as close as possible to the stability limit automatically. For thin circular plates subjected to blast loading, local stabilities form at the loaded edges and the stable time is very small resulting in many iterations in each simulation.

4.2 FINITE ELEMENT MODEL GEOMETRY

This section will describe the boundary conditions and elements used to construct the model.

4.2.1 MODEL SYMMETRY

An axisymmetric model was used since the explosive and the thin plate are circular and have the same centre line. This is preferable because it requires the least number of elements and will result in the smallest computational run times. (In ABAQUS/Explicit [32] the computational cost is directly proportional to the number of degrees of freedom in the model and the smallest element size.)

4.2.2 ELEMENTS USED

Due to the desired accuracy of the models it was decided to use solid elements to model the plates instead of shell elements. The elements used were:

CAX4R

An axisymmetric four noded bilinear element with reduced integration and hourglass control (see Figure 4.1).

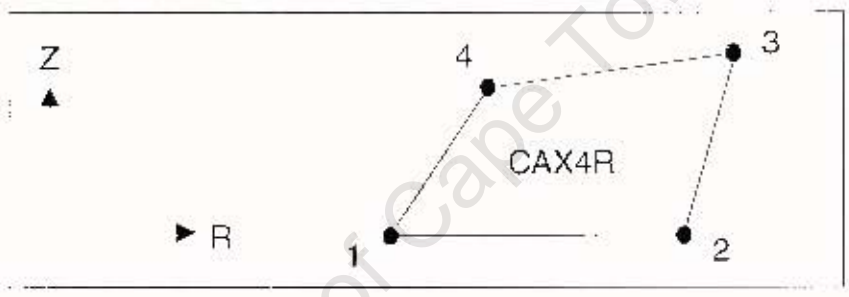

Figure 4.1: Schematic of a CAX4R Element.

CAX3

An axisymmetric three noded linear element (see Figure 4.2). This element was only used for mesh refinement due to the fact that the element has constant strain.

The element density varied greatly depending on the model, from the largest element size of 1 x 0.29 mm to the smallest element size of 0.02 x 0.02 mm. Mesh refinement was used extensively when fine meshes were used to allow for manageable run times. At no point did the element aspect ratio exceed four.

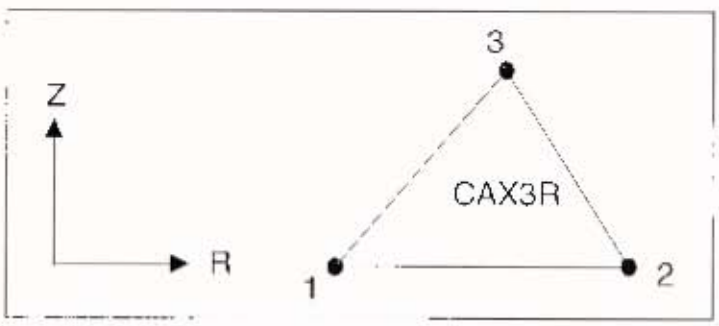

Figure 4.2: Schematic of a CAX3 Element.

4.2.3 BOUNDARY CONDITIONS

The plates modelled are thin circular-built-in plates as described in Section 3.1.2. Two different methods were attempted to model the built-in boundary conditions:

Encastre Boundary Condition

The boundary condition involves encastring the nodes along the built-in edge as shown in Figure 4.3. The boundary condition assumes that no displacement occurs along the built-in edge. This is an approximation that requires the minimum amount of elements resulting in the quickest computer run times.

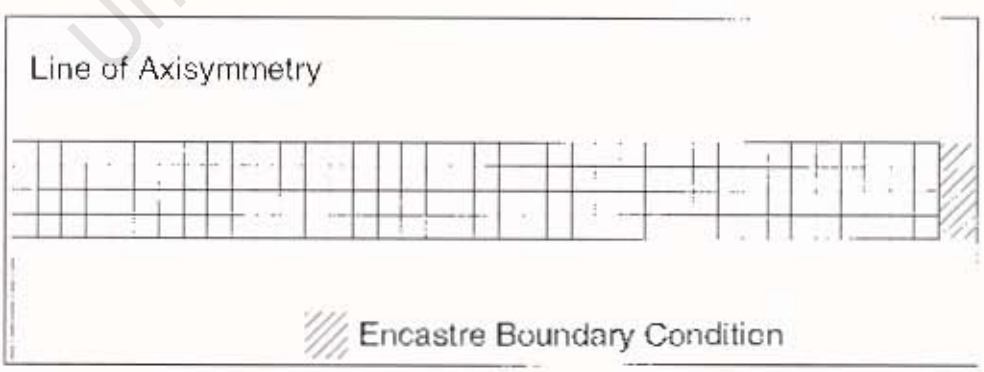

Figure 4.3: Encastred Boundary Conditions.

Modelling the Support

This boundary condition requires modelling the thicker part of the plate as shown in Figure 4.4. It was decided that best compromise between accuracy and manageable computer run times was a support with a width and height of three times the plate thickness. The edges of the support were then encastred. This method allows the plate boundary nodes to move and should provide a better solution. Modelling the support results in a 21.2 % increase in computational run time compared to the encastred boundary condition if a uniform mesh is used throughout the model.

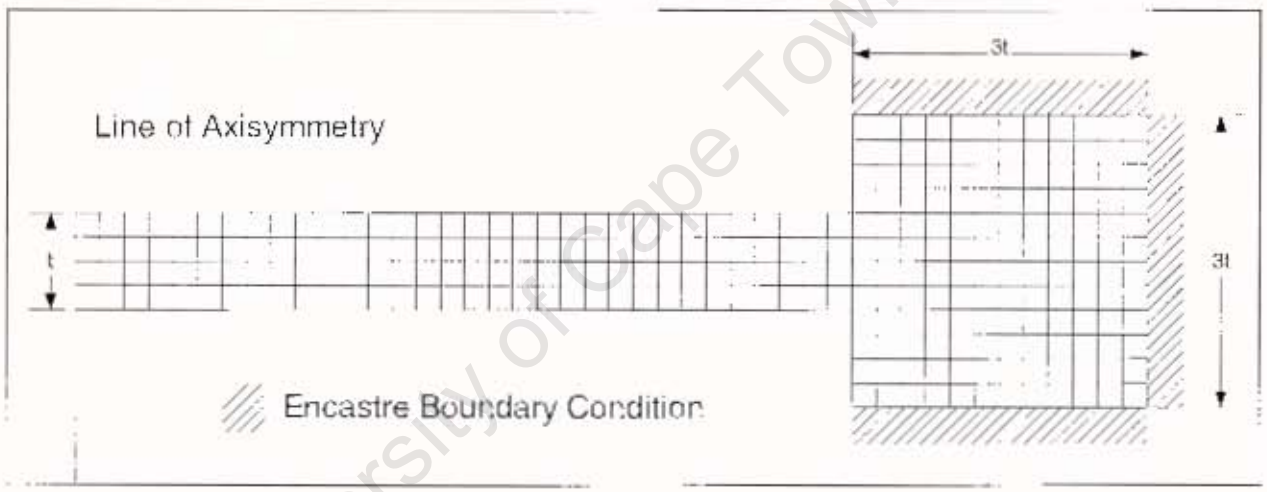

Figure 4.4: Modelling the Support.

4.3 MATERIAL PROPERTIES

The classical metal plasticity material model as discussed in Section 2.4.1 was used. The material model incorporated yield hardening, strain rate and temperature dependence. A strain based shear failure/predictor was also used.

4.3.1 YIELD HARDENING

Engineering stress strain curves were obtained from standard tensile tests and were converted into engineering static stress strain curves by Equation 2.18. The engineering static stress strain curves were then converted into true static stress and logarithmic plastic strain according to Equations 2.16 and 2.17. A graph of the true stress and logarithmic plastic strain is given in Figure 4.5.

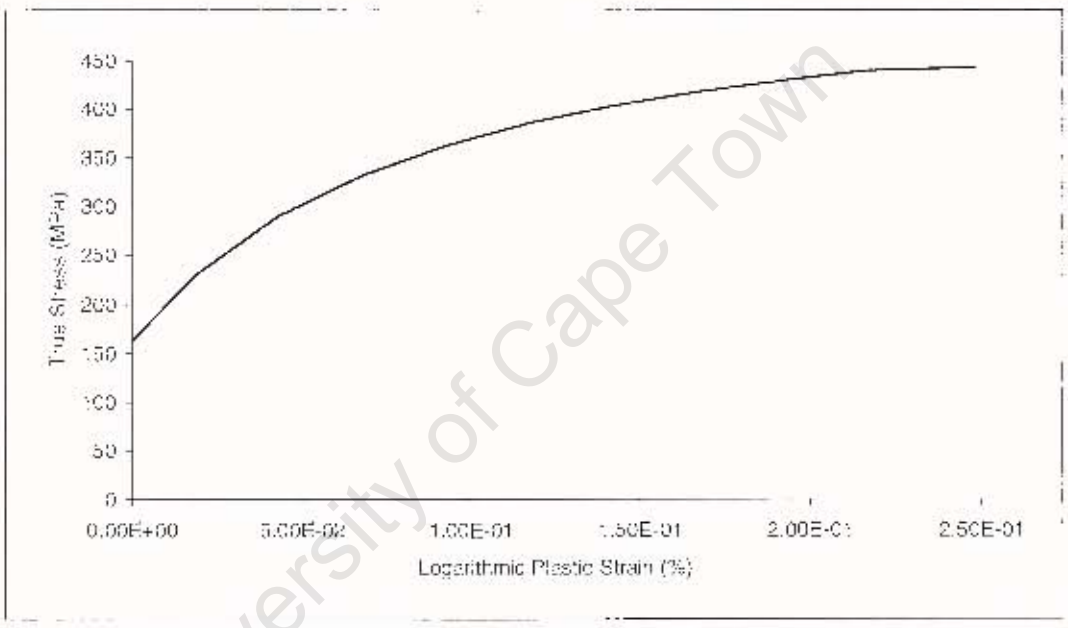

Figure 4.5: True Stress and Logarithmic Plastic Strain.

4.3.2 STRAIN RATE

Strain hardening is incorporated using the Cowper-Symonds equation (see Equation 2.18). The commonly accepted values for steel [33] of $D = 40.4\,s^{-1}$ and $n = 5$ were used.

4.3.3 TEMPERATURE DEPENDENCE

Temperature dependent material properties were incorporated in the second material model using the tabular form as described in Section 2.4.1. The material properties were obtained from Masui et al.[17]. The temperature effect on Young's modulus and the yield stress are given in Equations 4.3 and 4.4:

$$\begin{aligned} E &= 210 \cdot 10^9 - 58.34 \cdot 10^6 \cdot T && \text{for } T \leq 600\ ^\circ\text{C} \\ E &= 3.1 \cdot 10^5 (T - 1100)^2 + 97.9 \cdot 10^9 && \text{for } 600\ ^\circ\text{C} < T \leq 1100\ ^\circ\text{C} \end{aligned} \tag{4.3}$$

$$\begin{aligned} \sigma_y/\sigma_{yo} &= 1 && \text{for } T \leq 200\ ^\circ\text{C} \\ \sigma_y/\sigma_{yo} &= 1 - 0.00178(T - 200) && \text{for } 200\ ^\circ\text{C} < T < 700\ ^\circ\text{C} \\ \sigma_y/\sigma_{yo} &= 0.133 - 0.000388(T - 700) && \text{for } 700\ ^\circ\text{C} \leq T \leq 1000\ ^\circ\text{C} \end{aligned} \tag{4.4}$$

where σ_y is the temperature dependent static yield stress and σ_{yo} the static yield stress at the reference temperature of the tensile test. The results are shown in Figures 4.6 and 4.7. The Young's modulus is subjected to a gradual linear decrease from a value of 200 GPa at room temperature to 175 GPa at 600 °C. It is then subjected to a quadratic decay resulting in a value of 97.9 GPa at 1100 °C. The yield stress is affected to a greater extent then the Young's modulus by temperature. The yield stress remains constant until 200 °C where it is subject to a steep decay resulting in 11 % of the room temperature yield stress at 700 °C. At 1000 °C the yield stress is reduced to 2 % of its initial room temperature value. A temperature increase of only 280 °C from 200 °C will result in a yield stress decay of 50 %. A comparison of the temperature effect on the normalised Young's Modulus and the normalised yield stress is given in Figure 4.8.

Other constants required are the density and the specific heat, with commonly used values [34] of 7890 kg/m^3 and 452 J/kg K. It was assumed that the density and specific heat does not change with temperature [34].

Internal heat is generated through the dissipation of plastic work. For this study it is assumed that 90 % of the plastic work is converted to heat. It is assumed that the

model is adiabatic due to the very short duration of the blast (2 μs) and the subsequent deformation (150 μs) allowing very little heat to be dissipated from the deformation area.

STRAIN BASED SHEAR FAILURE CRITERIA

A shear failure criterion was used for most of the numerical simulations. The failure criterion is based on the fact that whenever the plastic strain in the element exceeded a specific value, the element was considered to have failed. This element is then removed from the model by making all of the element's material properties equal to zero. The method is described in Section 2.4.3.

4.4 MODELLING THE BLAST

Initially the blast was modelled using both the equation of state method and by applying a pressure distribution. However, the JWL Equation of state was not used because:

- Very fine meshes having many elements were often used resulting in long run times ($\pm$12 hours). The addition of the contact boundary condition between the explosive and plate would have made the run times even longer.
- The impulse obtained when the JWL Equation of state was used did not compare favourably to experimental values despite the fact that the displacement profile of the plates were acceptable. The JWL Equation of state model and the results are given in Appendix D.

All the subsequent modelling used the method of applying the pressure to the plate to model the blast.

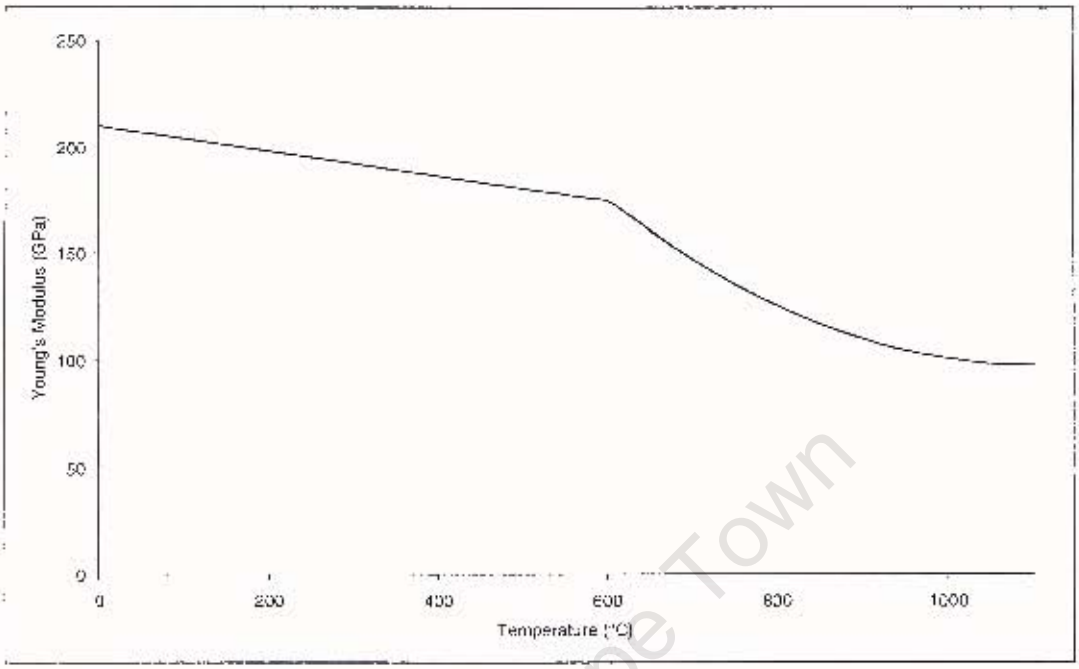

Figure 4.6: Young's Modulus as a Function of Temperature.

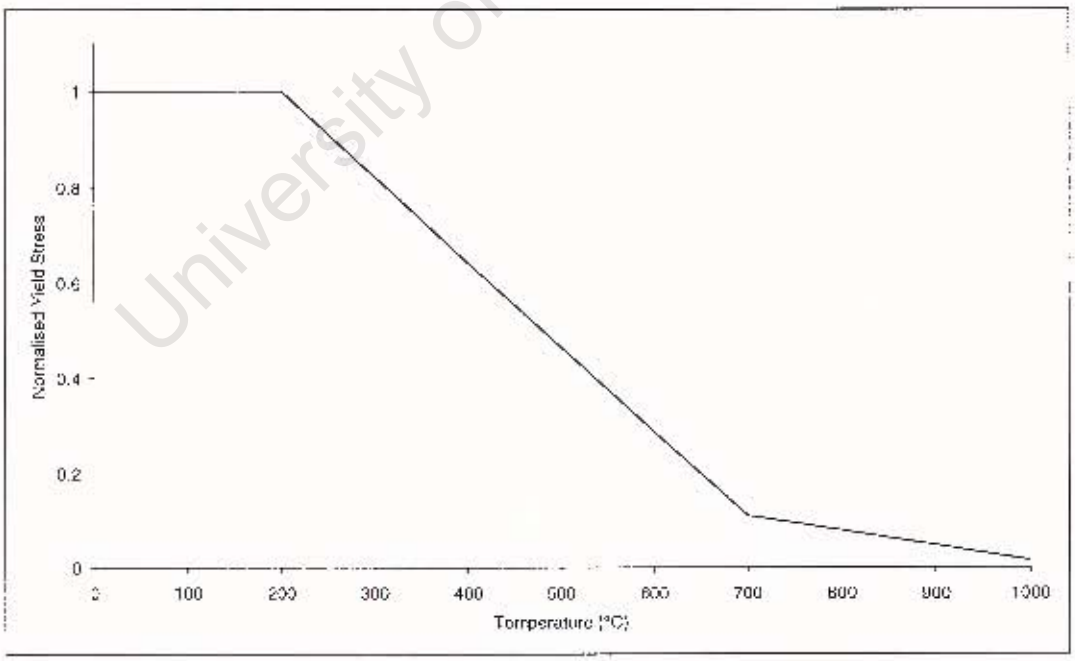

Figure 4.7: Normalised Yield Stress as a Function of Temperature.

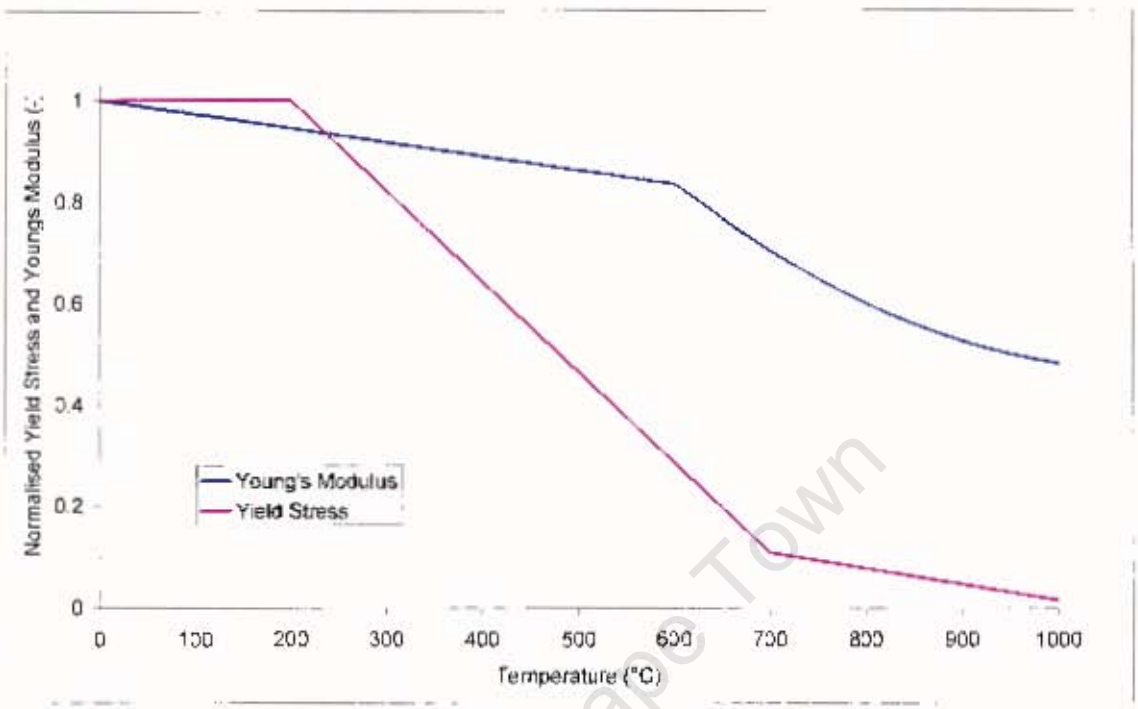

Figure 4.8: Effect of Temperature on the Young's Modulus and Yield Stress.

4.4.1 PRESSURE DISTRIBUTION USED

The pressure distribution used is the one defined by Bimha [9] where the pressure is constant over the area of the explosive and decays exponentially over the rest of the plate. The pressure details are described by the equations:

$$\begin{aligned} P(r) &= P_0 \quad \text{for} \quad r \leq R_0 \quad \text{and} \quad 0 \leq t \leq t_{Blast\ Duration} \\ P(r) &= P_0 e^{-k(r-R_0)} \quad \text{for} \quad R_0 \leq r \leq R \quad \text{and} \quad 0 \leq t \leq t_{Blast\ Duration} \end{aligned} \tag{4.5}$$

where P_0 is the pressure magnitude, k is the empirical exponential decay, r is the radius from the plate centre and t is the time after the start of the blast.

The approximate value of the blast duration is given by Equation 2.13 and is determined to be 1.786 μs. Simulations using different values for the blast duration were undertaken

(from 1 to 20 μs) providing similar results. A blast duration of 2.0 μs was used for the numerical modelling.

4.4.2 DETERMINING THE EXPONENTIAL DECAY

The numerical and experimental displacement profiles of three plastically deformed plates were compared for different exponential decay values. The best experimental decay constant for each plate was chosen by minimizing the residual sum of squares σ^2 between the experimental and numerical displacement profiles at nine evenly spaced points along the radius of the plate. The formula used to determine the residual sum of squares is:

$$\sigma^2 = \sum_{i=1}^{n} (\Delta y_{Experimental_i} - \Delta y_{Numerical_i}) \tag{4.6}$$

where n is the number of points, $\Delta y_{Experimental_i}$ is the experimental displacement at a radius of r_i and $\Delta y_{Numerical_i}$ is the numerical displacement at a radius of r_i.

The results of the optimum exponential decay are given in Table 4.1, and a comparison of the numerical and experimental displacement profiles can be seen in Appendix E. The value of the exponential decay was then found by averaging the three optimum decays giving a value of 1.2. This compares to a value of 1.24 obtained using Equation 2.14 as defined by Bimba [9]. A Graph of the pressure distribution is given in Figure 4.9. Only one experimental decay value is required since all the capped plates were blasted with the same explosive radii and have similar explosive masses. The pressure distribution is applied to the finite element model using a user subroutine VDLOAD programed in Fortran 77. An example of the VDLOAD subroutine used for plate T10 is given in Appendix F.

Table 4.1: OPTIMISED EXPONENTIAL DECAY

Test No	Plate Thickness (mm)	Explosive Mass (g)	Impulse (Ns)	Optimum Exponential Decay
T5	1.67	3.8	7.128	1.15
T6	1.61	3.5	6.66	1.3
T7	1.97	4.5	8.63	1.15

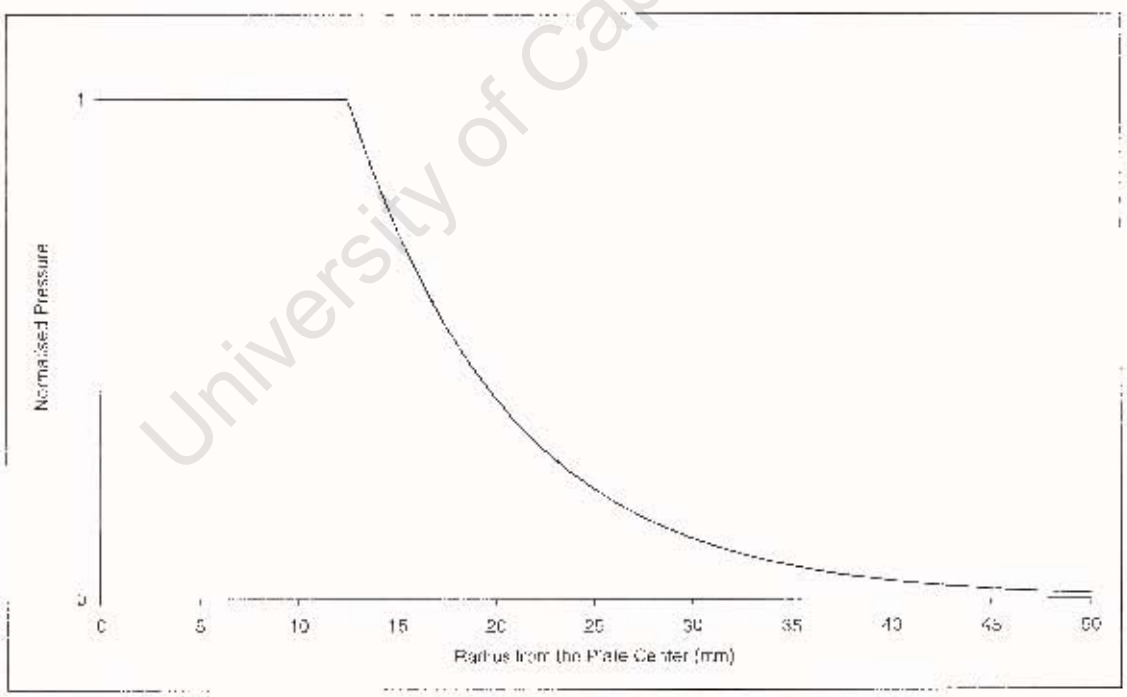

Figure 4.9: Pressure Distribution used to Model the Capped Plates.

Chapter 5

FINITE ELEMENT RESULTS

This section presents the results and discussions of the finite element simulations. The following main topics are presented:

- The numerical results and observations for both the fine and coarse meshes.
- Possible reasons for the mesh dependency.
- Method of plate fracture.
- An energy balance on the numerical model.

5.1 PLATE MODELLING USING A COARSE MESH

The simulations presented in this section have a uniform mesh using 50 x 6 elements in the plate resulting in a mesh density of approximately 1.0 x 0.267 mm. The material properties include temperature dependence. An example of an ABAQUS input deck for plate *T*10 is presented in Appendix G. Temperature profiles of the simulated plates are given in Appendix H.

5.1.1 UNCAPPED PLATES

Three uncapped plates were modelled. A deformation and temperature plot of plate $T7$ is given in Figure 5.1. Temperature rises are seen at the centre of the plate and at the boundary of the thin part of the plate. The temperature rise at the centre of the plate starts at a temperature of below 200 °C at 25 μs and reaches a temperature above 500 °C at 50 μs. The regions temperature increase slows down, finally reaching a maximum temperature of 700 °C at a time of 150 μs. At no point did the temperature dependence result in sufficiently large temperatures or strains through the whole thickness of the plate indicating that fracture would occur for any of the three uncapped plates that were modelled ($T5$, $T6$ and $T7$).

5.1.2 CAPPED PLATES

Subsequently, plates which were subjected to the capping behaviour were modelled. Figure 5.2 shows the temperature and displacement result for plate $T10$. The simulation is subjected to severe temperature rises at three different localizations:

- The region of cap fracture.
- The centre of the plate.
- The boundary of the thin part of the plate.

The most severe temperature rise is in the region of cap fracture. This is shown in Figure 5.3. At a time of about 40 μs, a temperature band with a width of three elements forms through the thickness of the plate. As the simulation progresses, the temperature of the band becomes hotter, the elements undergo extensive elongation in the radial direction and severe necking occurs. The element elongation exceeds realistic strains (at a time of 100 μs the strain exceeds 500 %) indicating that failure will occur within the narrow band.

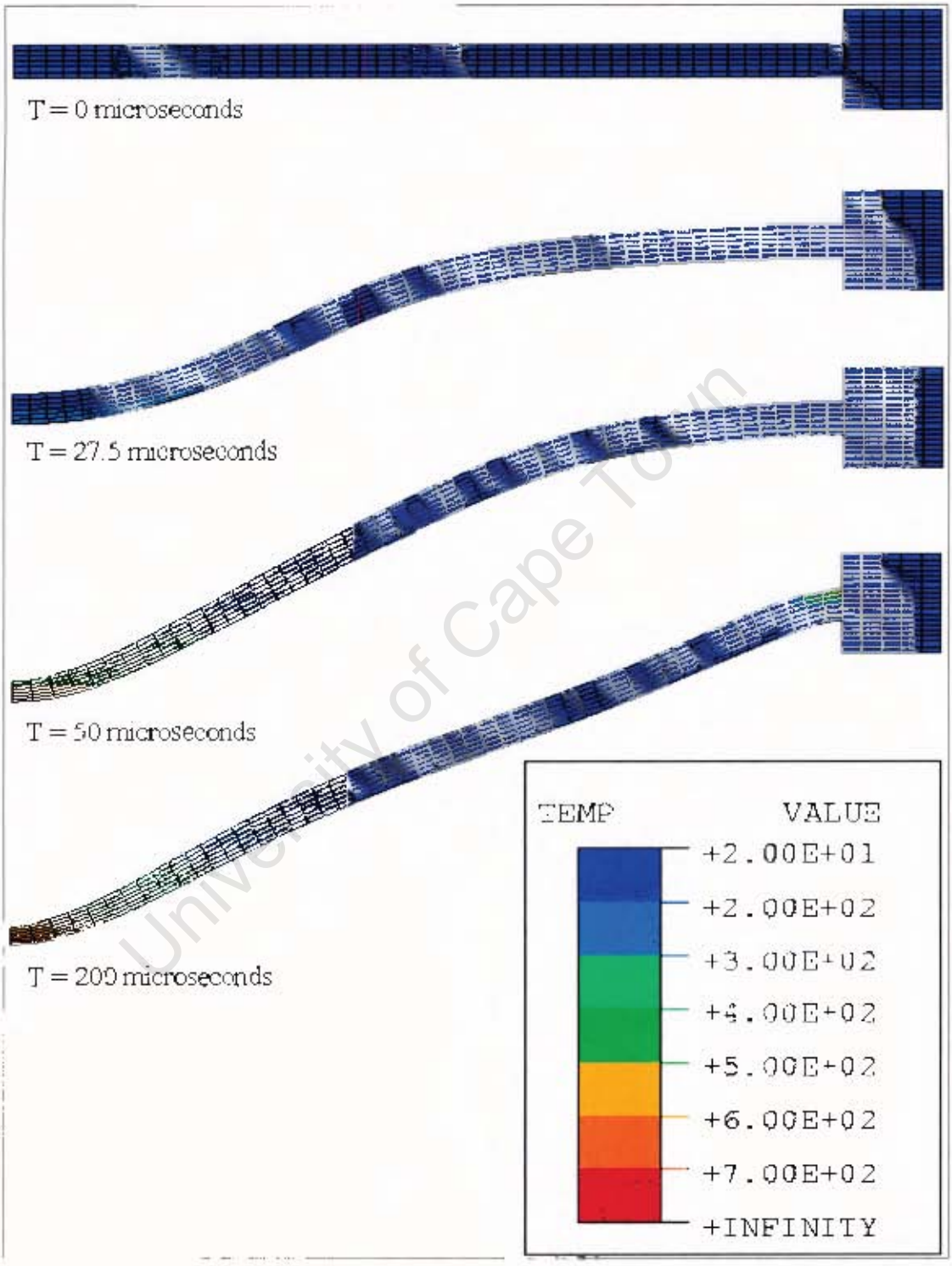

Figure 5.1: Whole Model Displacement and Temperature Profiles of an Uncapped Plate Using a Coarse Mesh (1 x 0.292 mm).

The reason for the severe element elongation can be ascribed to the effects of the temperature dependent material properties. At a particular localized point, a slightly larger amount of strain occurs compared to the surrounding areas. This results in greater adiabatic heating due to the large amount of plastic work resulting in the weakening of the material properties due to the rise in temperature. The weakening material properties result in even larger strains and higher temperatures until unrealistic elongation occurs. The increase in temperature offsets the strain hardening that usually occur with large strains.

The boundary of the plate experiences temperature localization (see Figure 5.4). The boundary temperature localization occurs after the localization in the region of cap fracture and the excessive elongation, as seen in the region of the cap, is not seen. Temperature localization at the centre of the plate occurs between 40 and 60 μs. The localization does not occur through the entire thickness of the plate and does not result in excessive temperatures or strain. No appreciable temperature rise occurs after 60 μs.

The strains that occur in the necked region reach unrealistic values due to thermal softening indicating that fracture would occur at some point. In order to determine the time of fracture, the fragment radius and fragment velocity, a failure criteria with a failure strain of 200 % was imposed on the model. The 200 % failure strain used in the model was a chosen number that ensures failure after extensive adiabatic heating in the localized region. The results of the capped model simulations are shown in Table 5.1.

A parametric study with the aim of determining the critical impulse for complete fracture throughout the thickness of the plate was undertaken. Plate T10 was subjected to varying impulses and it was found that fracture throughout the thickness of the plate occurred between the impulse of 8.36 N s and 8.88 N s . This results in a critical dimensionless impulse between 33 and 35.1 which compares well with an experimental critical dimensionless impulse of 34 - 40 (see Section 3.2.2).

The numerical cap velocities predicted by the use of the simple failure strains compare favourably with the experimental values. From the simulation results, it appears as

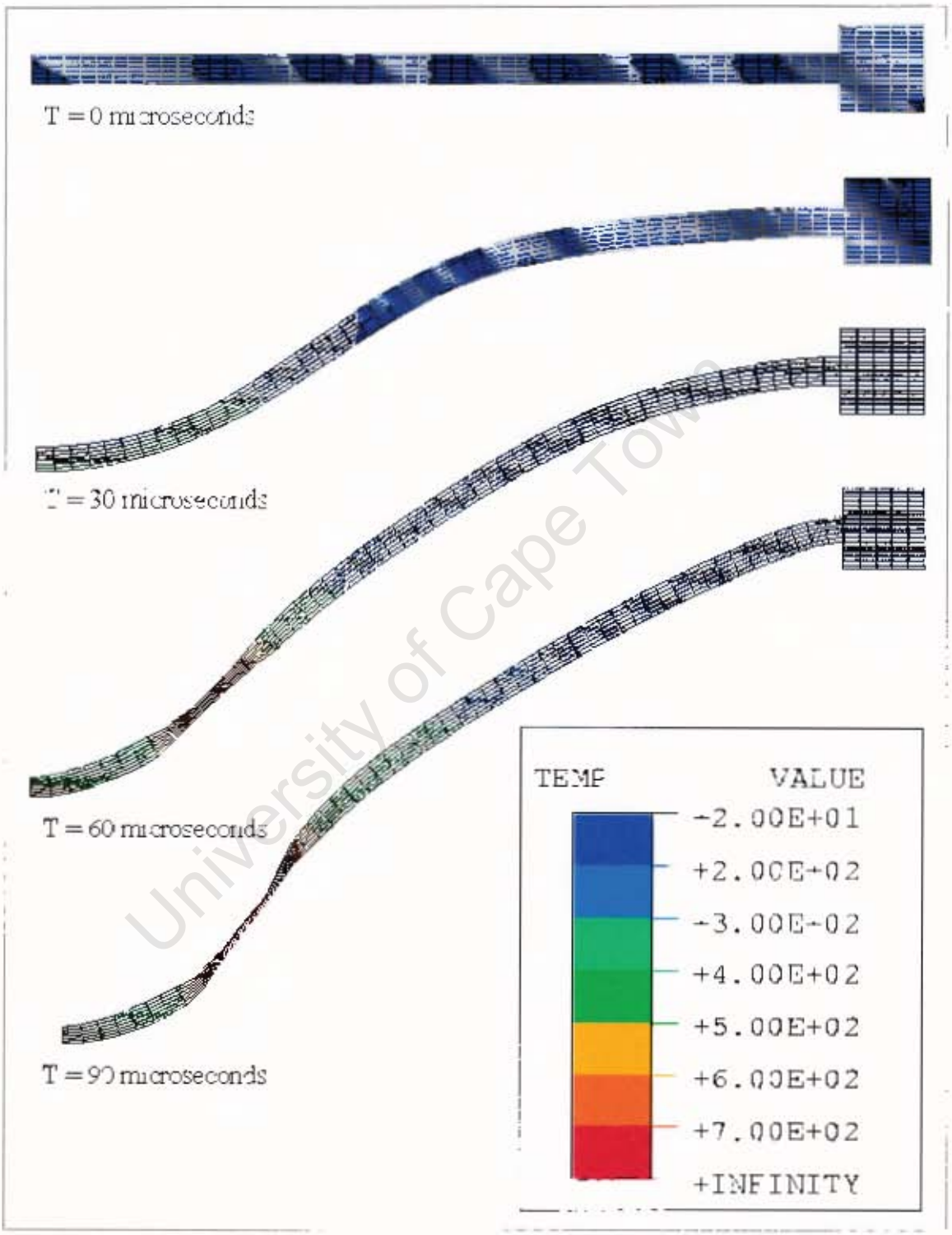

Figure 5.2: Whole Model Displacement and Temperature Profiles of a Capped Plate Using a Coarse Mesh (1 x 0.292 mm).

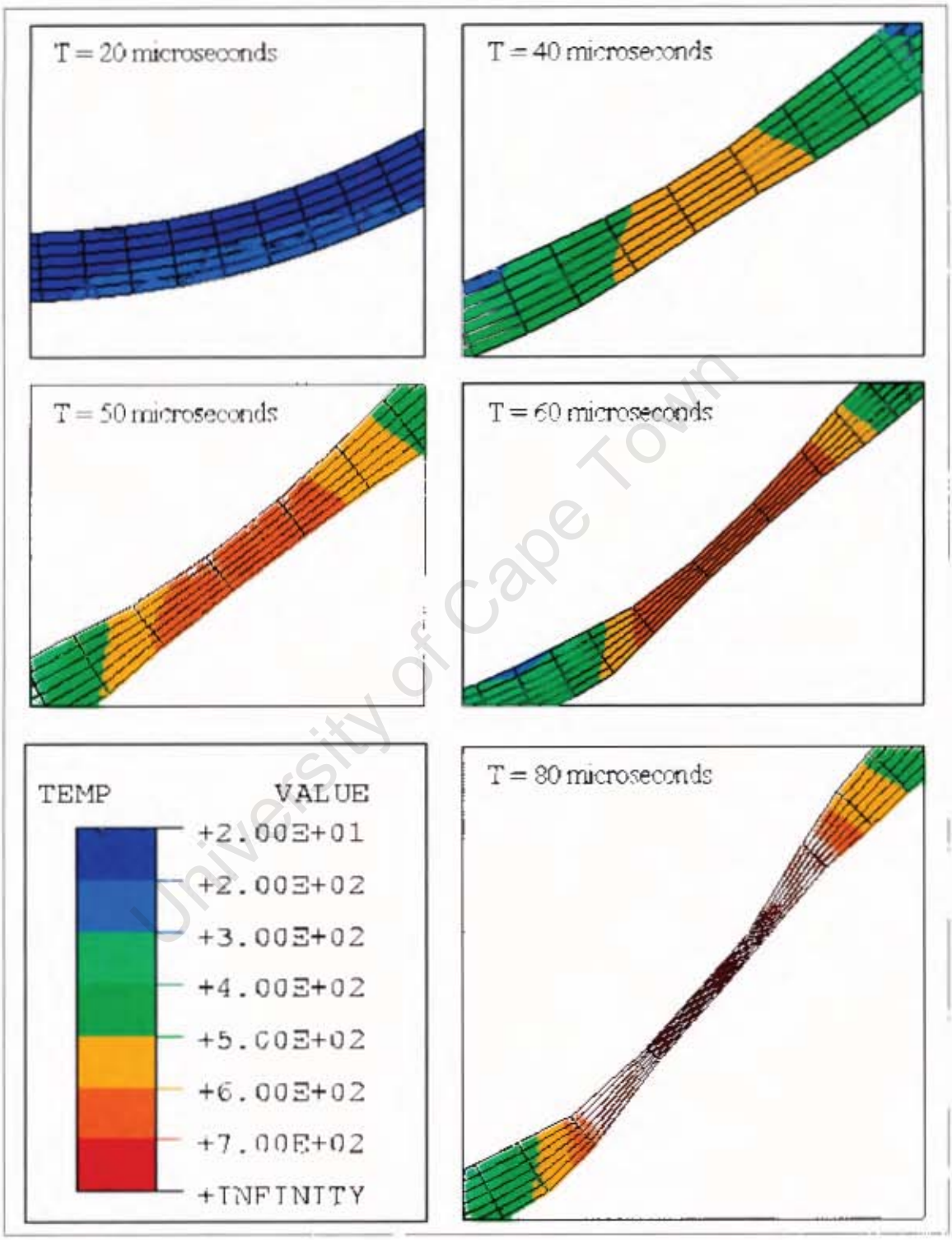

Figure 5.3: Displacement and Temperature Profiles in the Area of Cap Formation for a Coarse Mesh (1 x 0.292 mm).

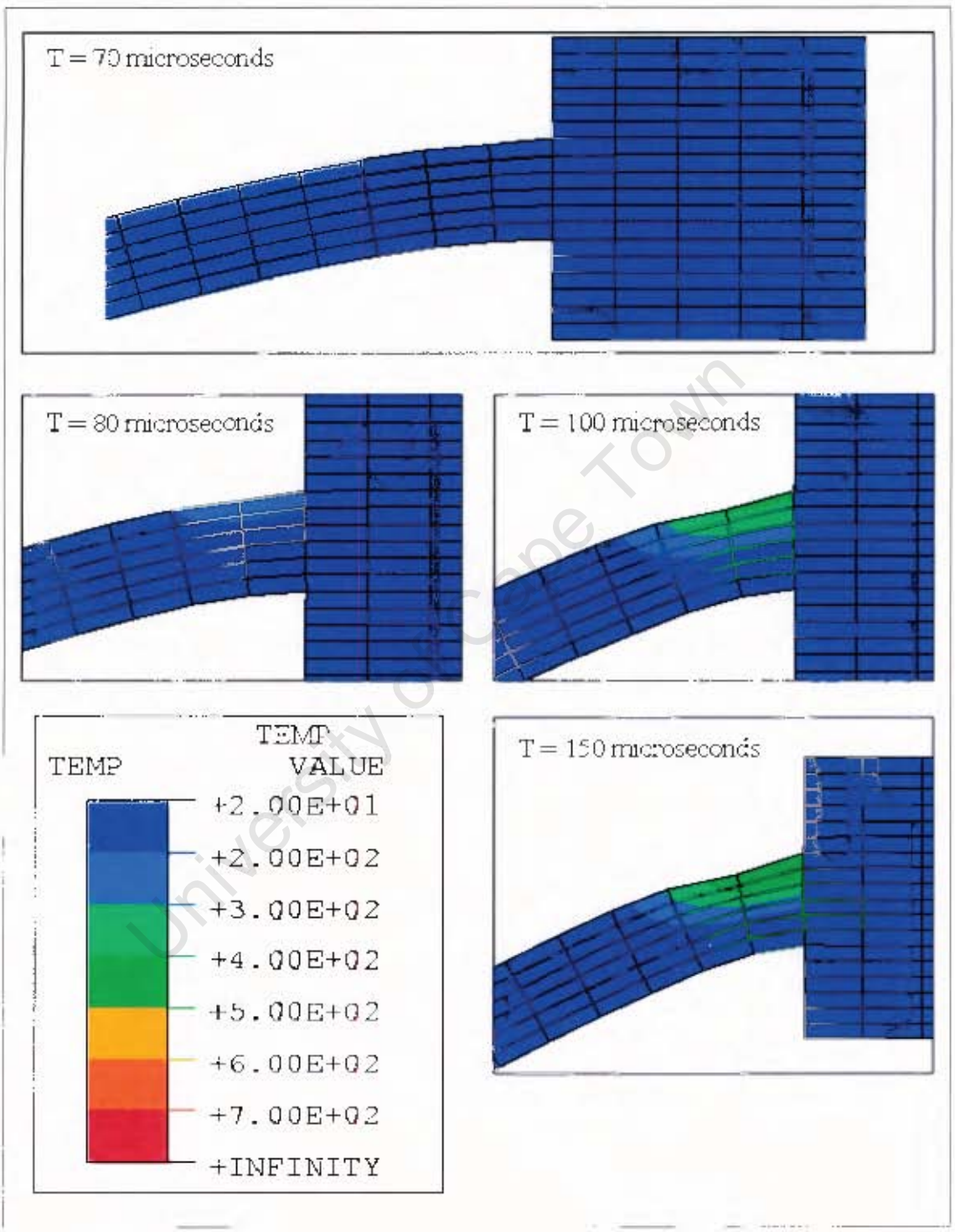

Figure 5.4: Displacement and Temperature Profiles at the Plate Boundary for a Coarse mesh (1 x 0.292 mm).

Table 5.1: COARSE MESH SIMULATION RESULTS

Plate	Experimental Radius	Experimental Velocity	Numerical Radius	Numerical Velocity
$T10$	9.3	293.7	9.5	285
$T11$	9.6	233.2	9.6	255.1
$T12$	8	310.4	9.5	270.9
$T16$	9.4	282.3	9.8	282
$T18$	9.3	402.9	9.5	303.4

though failure is as a result of thermal softening leading to extensive necking. However, the excessive necking seen in the numerical simulations has not been observed in the experimental results (see Section 3.2.3).

5.2 PLATE MODELLING USING FINE MESHES

In order to determine mesh sensitivity the analyses are repeated using progressively finer meshes. As the mesh size approaches 0.08 x 0.08 mm, the formation of shear bands were observed. Figure 5.5 shows plate $T10$ modelled with a mesh size of 0.04 x 0.04 mm in the region of the cap radius. Temperature localizations are seen to occur in the region of the cap boundaries and the boundary of the thin plate.

Instead of extensive necking occurring in the area of capping, the formation of shear bands are observed. The process of shear band formation is shown in Figure 5.6. Figure 5.7 shows the subsequent fracture of the shear band due to the 200 % failure strain imposed on the model. The first sign of a temperature localization in the form of a shear band occurs after 12 μs. At 13 μs two shear bands can be identified at an angle of 45° to the midplane of the deformed plate. The primary shear band is larger than the secondary shear band. Both shear bands develop, in terms of temperature and width, with time. However, the secondary shear bands appear to stop developing and become stable after 14 μs, while the primary shear band becomes hotter and wider due

to increases in strain. By 16 μs the strains in the primary shear band start to exceed 200 %, and the elements are deleted due to the failure criterion. By 17 μs the strain in the primary shear band has reached 200 % through the thickness of the plate and the cap separates from the plate. The shear band took 4 μs to fracture from first detection of a temperature localization. The numerical model predicts a fragment with a radius of 10.1 mm and a velocity of 474 $\mathrm{m\,s^{-1}}$. This compared to an experimental radius of 9.3 mm and a velocity of 285 $\mathrm{m\,s^{-1}}$. The poor fragment velocity obtained using a fine mesh can be ascribed to the early failure time of 17 μs compared to $\pm$55 μs for the coarse mesh.

At a time of 90 μs a temperature localization is seen at the boundary of the thin part of the plate (see Figure 5.8). The temperature localization results in excessive thermal softening resulting in a plastic hinge at the boundary that subsequently fails at 110 μs. None of the 1.6 mm plates exhibited failure at the boundaries. However, failure at the boundary is a common cause of failure for 2.6 and 3.6 mm built-in plates (as reported by Chung [8]).

Table 5.2 compares the numerical and experimental results. The temperature profiles of the modelled plates are shown in Appendix 1. The simulated cap velocities are over 50 % greater then the experimental velocities. The poor fragment velocity obtained using a fine mesh can be ascribed to the early failure time of $\pm$16 μs compared to $\pm$55 μs for the coarse mesh. The simulated plates have a cap radius of $\pm$11 mm as opposed to the experimental values of $\pm$9.2 mm.

5.2.1 EFFECT OF MESH DENSITY

Depending on the density of the mesh or the aspect ratio of the elements, it is found that the shear band changes with respect to the number, width, angle and position of the shear bands. The results of the different shear bands for different mesh densities can be seen in Figure 5.9 and the results are summarized in Table 5.3. All the shear bands occurred at an angle of either 45° or 135° to the plate midplane and one or more secondary shear bands were often formed. The secondary shear bands usually

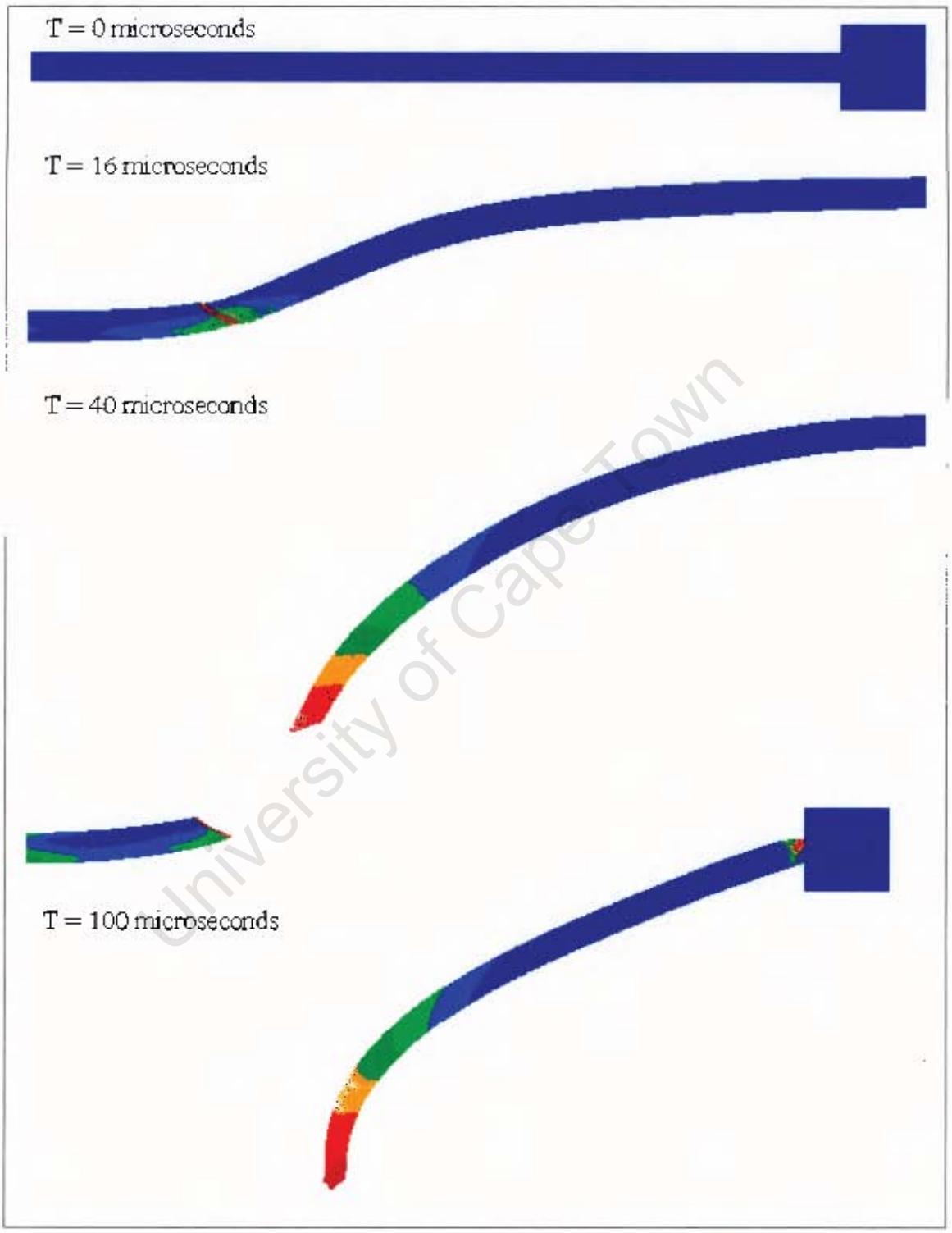

Figure 5.5: Whole Model Deformation and Temperature Profiles for a Mesh Density of 0.04 x 0.04 mm.

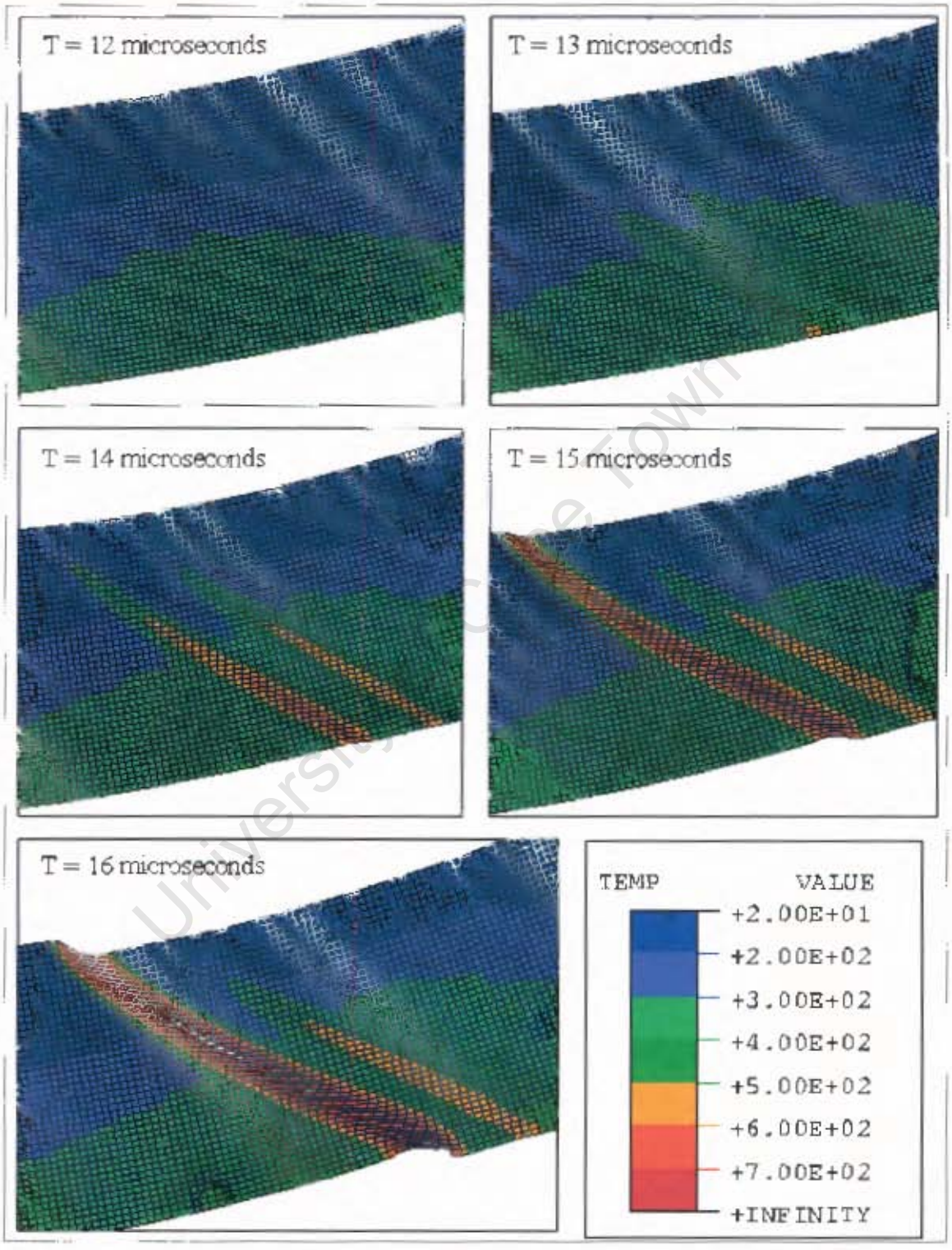

Figure 5.6: Shear Band Formation for a Mesh Density of 0.04 x 0.04 mm.

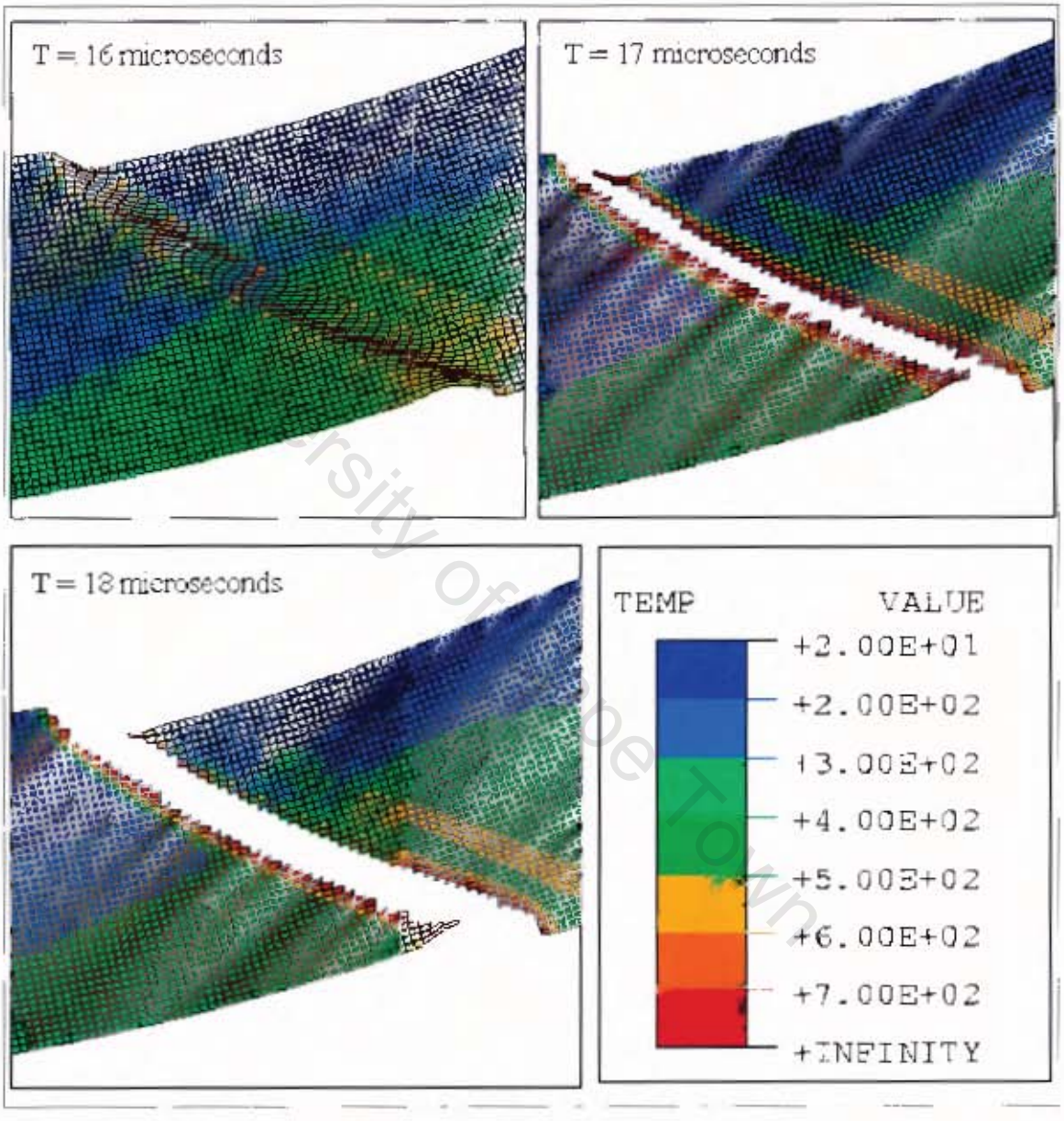

Figure 5.7: Shear Band Fracture for a Mesh Density of 0.04 x 0.04 mm.

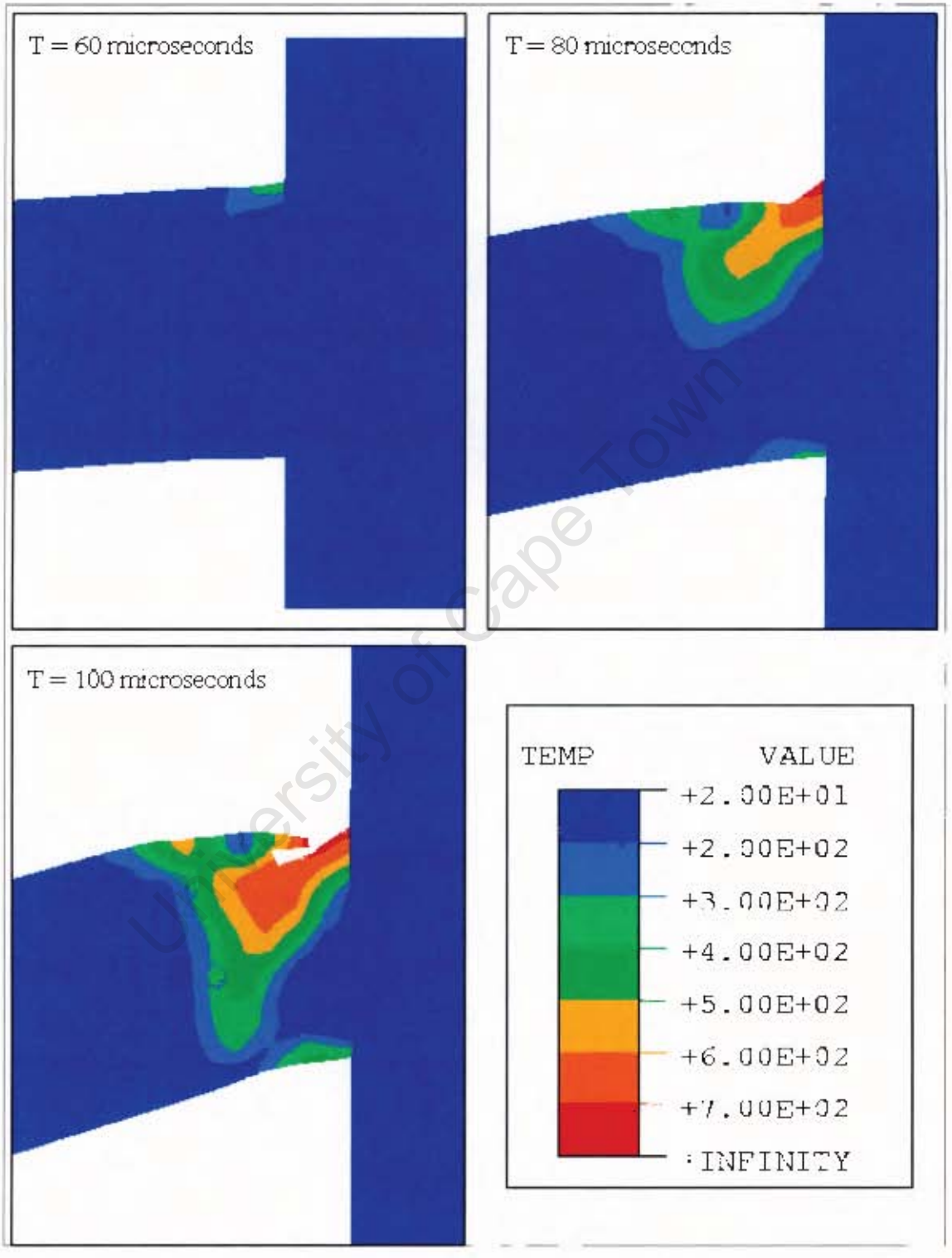

Figure 5.8: Temperature Localization at the Boundary of the Thin Plate for a Mesh Density of 0.04 x 0.04 mm.

Table 5.2: FINE MESH SIMULATION RESULTS

Plate	Experimental Radius	Experimental Velocity	Numerical Radius	Numerical Velocity
T10	9.4	293	11.09	474
T11	9.6	233.2	11.06	425
T12	8	310.4	10.7	475
T16	9.4	282.3	10.8	493
T18	9.3	402.9	11.1	550

remained stable. The shear band width varied extensively with the mesh density - the larger the elements, the larger the shear band. Mesh density had little effect on the cap radius.

It is suspected that the change in direction and the exact location of the shear bands is due to numerical noise. Experimental observations show that fracture occurs at an angle of either 45° or 135° to the midplane of the plate for different segments of the cap in what appears to be a random distribution. Local imperfections, either material and/or geometric, determine the angle of failure for a segment of the cap. Similarly, in the numerical model, local imperfections can be used to determine the angle (45° or 135°) of the shear bands.

The shear bands are mesh dependent in terms of the shear band width, time of fracture and fragment velocity. The width of the shear bands are proportional to the mesh density- the finer the mesh the smaller the shear band density. Typically three elements would fracture. Similarly the smaller the mesh is the earlier the time of fragment fracture which results in larger cap velocities.

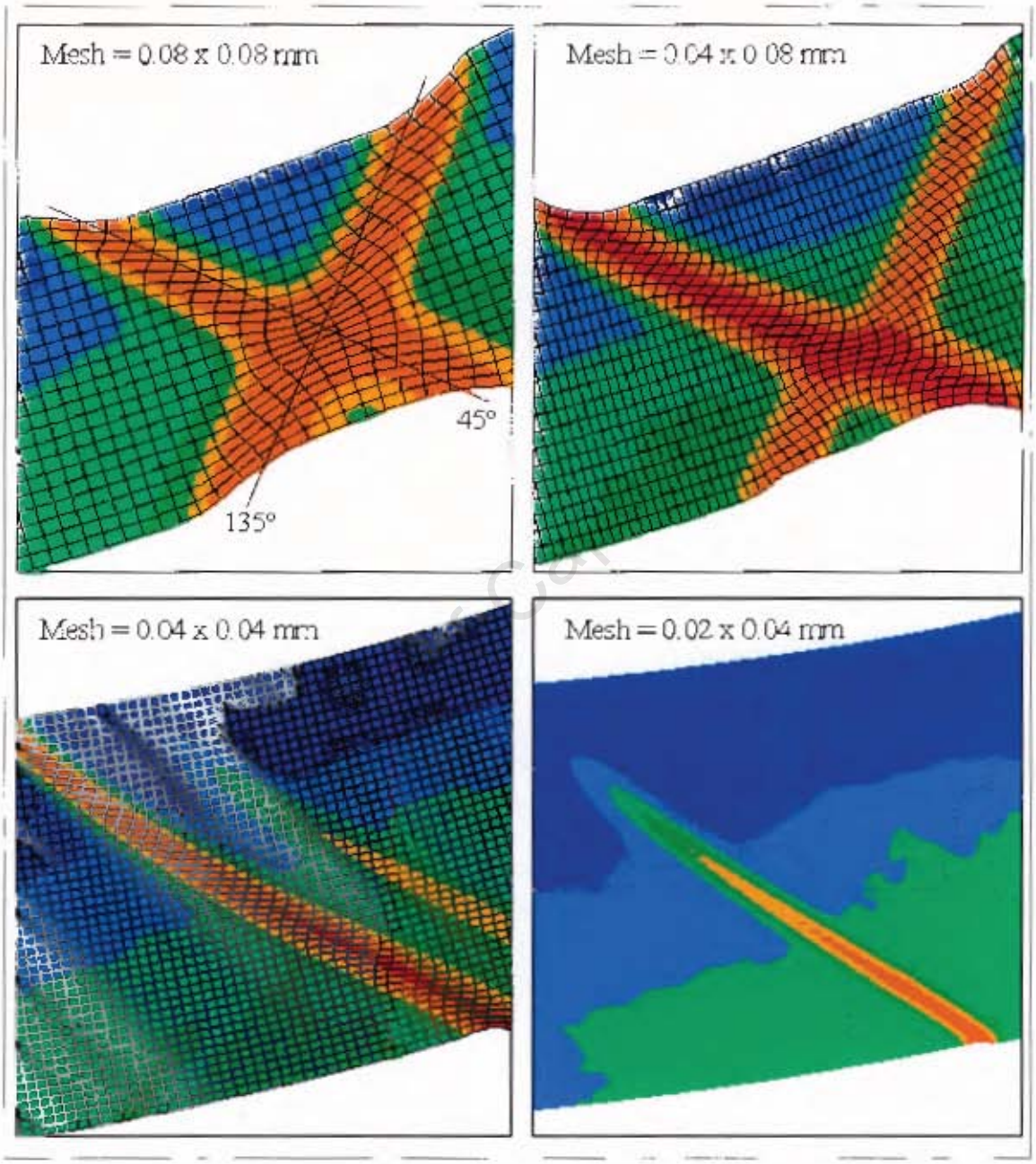

Figure 5.9: The Effects of Mesh Density on the Shear Bands.

Table 5.3: EFFECT OF MESH DENSITY ON FINE MESHES

Mesh Density (mm)	Time of Failure (μs)	Shearband Width	Angle of Fracture (Degrees)
0.08 x 0.08	26	Approximately	45° and 135°
0.04 x 0.08	22	Three	45° and 135°
0.04 x 0.04	18	Elements	45°
0.02 x 0.04	16		45°

5.3 POSSIBLE EXPLANATION OF THE MESH DEPENDENT RESULTS

The shear bands are only detected with the fine meshes. The coarse mesh does not have the resolution to detect the narrow shear bands which are smaller than the length of the elements. Once the mesh is fine enough to sense the shear bands, the shear band width is proportional to the element size. One explanation for this phenomenon is the use of an adiabatic finite element model. The adiabatic model does not allow for any heat transfer to occur. However, if one was to consider a transitional one dimensional heat transfer problem subject to conduction [35]. The solution can be solved using an explicit numerical scheme, where the temperature of a node at an increment in time is given by the equation:

$$T_i^{t+\Delta t} = T_i^t + \frac{\alpha \Delta t}{(\Delta x)^2}(T_{i-1}^t - 2T_i^t + T_{i-1}^t) \tag{5.1}$$

where $T_i^{t-\Delta t}$ is the temperature at node i and a time of $t - \Delta t$, Δx is the mesh spacing, Δt is the time increment and α is the thermal diffusivity.

Modifying Equation 5.1 to obtain the change in temperature for a single time increment at a particular node:

$$T_i^{t+\Delta t} - T_i^t = \cdot \frac{\alpha \Delta t}{(\Delta x)^2}(T_{i-1}^t - 2T_i^t + T_{i+1}^t) \tag{5.2}$$

Equation 5.2 shows that the change in temperature due to conduction is inversely proportional to the mesh density squared. For finer meshes the temperature change between two elements due to conduction will be greater and make the adiabatic approximation for the shear bands less valid. Heat conduction will dissipate some heat away from the shear band to the surrounding elements and possibly resulting in the following two effects:

- Make the shear band wider since the surrounding elements will also have degraded material properties. This may result in a minimum shear band width for very fine elements.
- The plate should fracture at a later time since the heat dissipated from the region should slow the material degradation. This will result in slower fragment velocities that will correspond better with experimental values.

5.4 METHOD OF PLATE FAILURE

The numerical results indicate that fracture involves a thermo-mechanical cycle whereby increased strain at a localized location results in increased temperatures weakening the material properties resulting in even larger strains and temperatures. However, the exact method of dynamic fracture appears to be dependent on the mesh density squared. Coarse meshes show fracture occurring through excessive thinning over a width of three elements. Fine meshes predict the formation of narrow shear bands at angles of 45° or 135° degrees to the angle of the deformed plate. Comparison of the numerical and

experimental results support the observations seen for the fine mesh:

- The experimental plates fail at angles of 45° or 135° to the deformed plate as predicted by the fine mesh.
- The excessive necking as observed by the coarse mesh simulations can not be seen in the specimens.

The coarse mesh is not able to pick up the shear bands because the shear bands are smaller then the mesh density. Therefore, it can be concluded that shear bands are formed in the region of the cap and the cap fracture occurs due the excessive strains caused by the formation of shear bands. The extremely large strains that occur in a very short time ($=4\,\mu s$) make the value of the failure strain less critical due to the thermo-mechanical process that can occur with temperature dependent material properties.

5.5 THE NUMERICAL ENERGIES

This section investigates the whole model energies and the energies involved in the shear band and attempts to determine the approximate energy required to cause capping. Plate T10 is used for this analysis.

5.5.1 THE WHOLE MODEL ENERGIES

Various energies can be obtained from ABAQUS Explicit as output variables [36]. The theory behind the method of calculating the energies is given in the ABAQUS theory Manuel [37]. The whole model energies consist of three main parts for the model: external work, kinetic energy and the strain energy. The external work is the energy done by the applied pressure pulse simulating the blast. The kinetic energy is the energy associated with the velocity of the individual elements. This includes the velocity of

the fragment and the kinetic energy of the moving elements associated with the plate. The strain energy is all the energy involved with the element deformation. The strain energy can be broken into the following individual components: the recoverable elastic strain energy, energy associated with plastic deformation and the 'artificial' strain energy associated with constraints used to remove singular modes (such as hourglass control). The strain energy also includes the heat since the heat is defined as 90 % of the plastic energy.

A graph of the energies associated with a coarse mesh (1 x 0.292 mm) can be seen in Figures 5.10 and 5.11. External work of 1540 J is applied during the blast duration (the first 2 μs). The external work is transferred immediately into a combination of kinetic energy and strain energy. Subsequently the kinetic energy is transferred to strain energy until it reaches a constant value of about 160 J. The 160 J of kinetic energy can be broken up into two components:

- The kinetic energy of the fragment - 158 J.
- The kinetic energy due to the vibration of the model. - 2 J.

The value of the kinetic energy due to plate vibration is because the model does not incorporate damping. Damping would dissipate the kinetic energy, but it requires a damping coefficient. Choosing a realistic damping coefficient is not an easy task.

A comparison of the whole model energies for a fine mesh (0.04 x 0.04 mm) is given in Figure 5.12. The external work is the same for both the coarse and fine mesh simulations. Figure 5.13 compares the kinetic energy of both the fine and coarse mesh densities. After 22 μs the kinetic energy of the fine mesh decreases far slower than the coarse mesh. This can be explained by the far greater kinetic energy of the fine mesh simulation due to its larger and faster fragment. The fragment kinetic energy is 599.3 J for the fine mesh and 158 J for the coarse mesh. The experimental kinetic energy of the fragment for plate $T10$ is 152.2 J.

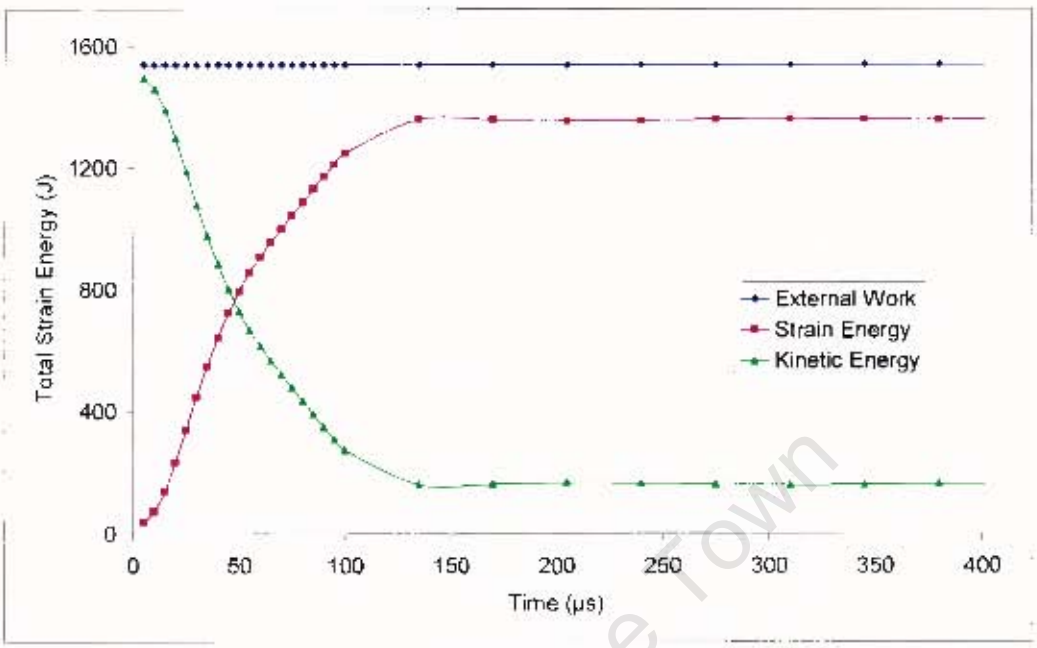

Figure 5.10: Whole Model Energies with a Coarse Mesh (1 x 0.292 mm).

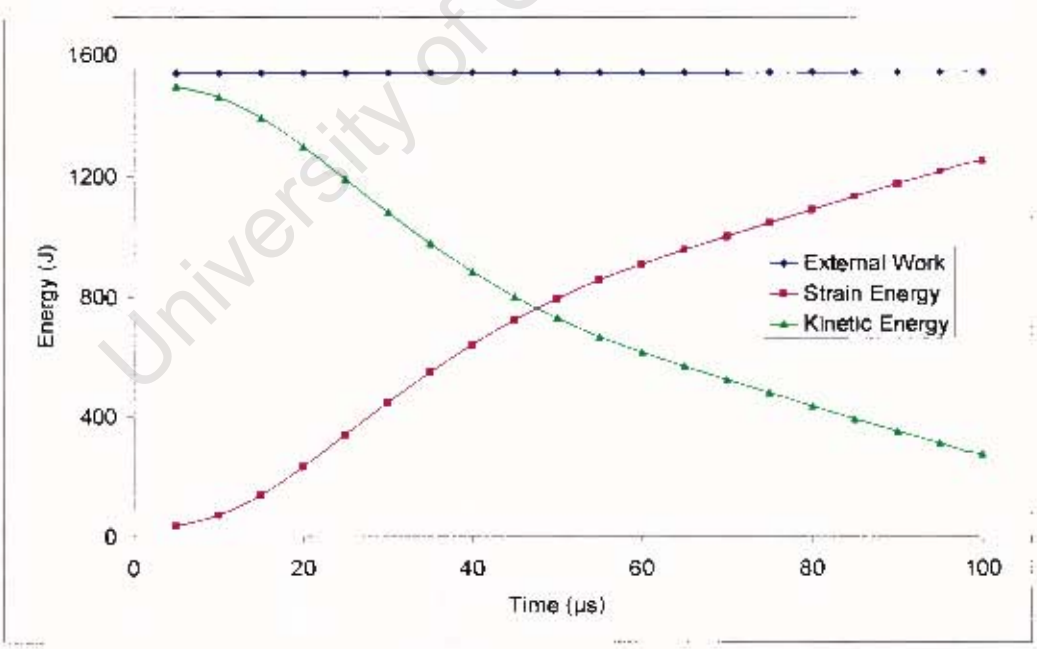

Figure 5.11: Whole Model Energies with a Coarse Mesh Using a Different Time Scale (1 x 0.292 mm).

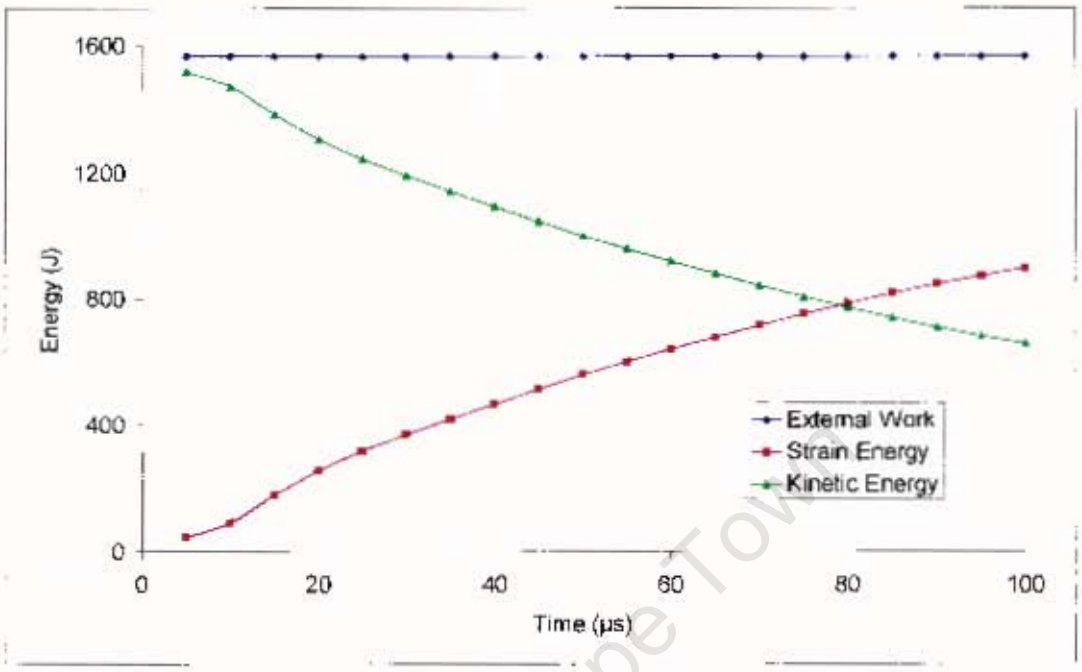

Figure 5.12: Whole Model Energies with a Fine Mesh (0.04 x 0.04 mm).

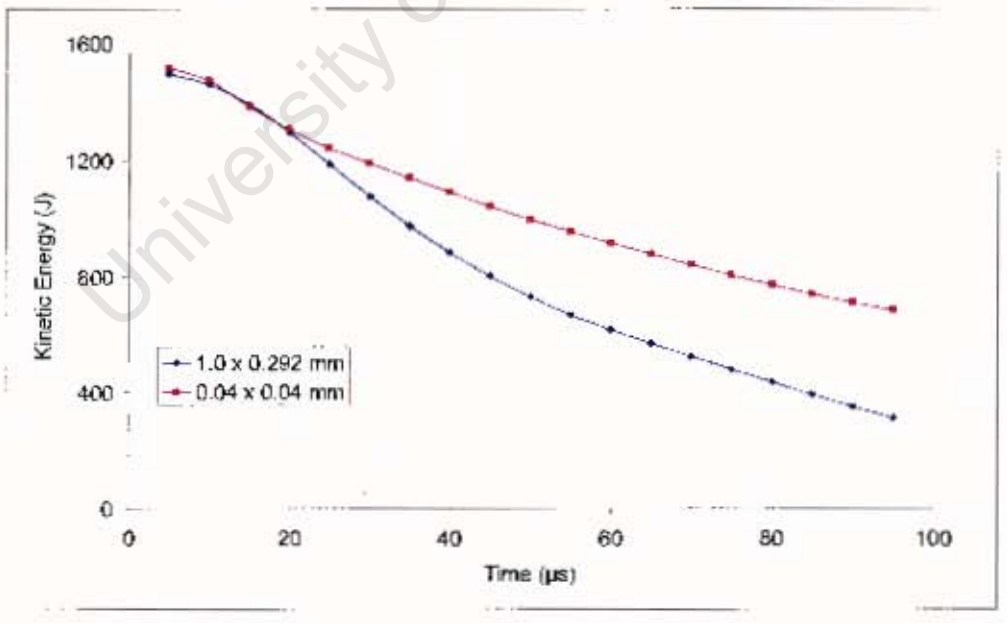

Figure 5.13: Comparison of the Kinetic Energy for both a Fine and Coarse Mesh.

5.5.2 THE SHEAR BAND ENERGY

A strain energy profile of the midplane of the plate in the region of the shear band for a fine mesh is shown in Figure 5.14 for different times. After 12 μs two rapid buildups of strain energy can be observed indicating the formation of a primary and secondary shear band. A very steep jump in energy density occurs from the undisturbed elements to the shear band elements. The rapid buildup of strain energy occurs through a width of 6 - 9 elements, of which five elements fractured due to the 200 % failure strain.

In order to find the strain energy required to form the shear band, it is necessary to determine the width of the shear band. Two different areas will be defined - the fractured region and shear band region. The fractured region is a conservative approach that regards all the elements that have fractured to belong to the shear band. The shear band region is defined as being the width of the fractured region plus three elements either side of the fractured region (see Figure 5.15). In some cases the number of elements chosen either side of the fractured region may be too large. However, it can be justified by the fact that the strain energy of any element that is not in the shear band contains under a third of the strain energy of any element in the shear band as seen in Figure 5.14.

In order to determine the additional amount of strain energy to form the shear band, a maximum energy density where shear bands will not form needs to be determined. The maximum energy (offset energy density) was determined by averaging the energy density of the elements either side of the shear band zone. An offset shear band energy was found by multiplying the offset energy density by the area of the shear band region. Similarly an offset fractured region was also obtained using the area of the fractured region.

A graph of the strain energies in the different regions is shown in Figure 5.16 for a mesh density of 0.01 x 0.04 mm. The strain energy of the offsetted shear band region and the shear band region contain the same amounts of energy until 12 μs - the first indication of shear band formation as seen in Figure 5.6. The extra energy required to form the

shear band until the time of fracture is found by subtracting the strain energies of the offset regions from the shear band regions as shown in Figure 5.17. From Figure 5.16, it can be determined that the shear band requires 11 J of strain energy from the start of the blast to the time of cap fracture. At the time of fracture, an additional amount of 7 J of strain energy is required compared to the surrounding areas of equal volume (as seen in Figure 5.17). The total strain energy required to fracture the plate is approximately 0.7 % of the total energy of the blast applied to the system. This is approximately 4.4 % of the experimentally measured kinetic energy of the fragment.

The effect of mesh density on the amount of energy to form a shear band is shown in Figure 5.18 for mesh densities of 0.04, 0.05, 0.06 and 0.08 mm. It is observed that a linear relationship exists between the mesh density and the strain energy. This can be explained by the linear relationship between mesh size and shear band width. The mesh dependency of the shear band makes it extremely hard to determine the exact amount of energy required to form the shear bands. Any energies obtained can only be regarded as order of magnitude results.

5.5.3 DETERMINING THE ENERGY OF TEARING

The energy of tearing involves two components, namely the strain energy involved in the formation of the shear band and any possible energies involved at the exact moment of fracture. The numerical model is able to simulate the formation and expansion of the shear bands. The actual fracture process cannot be simulated properly. The best that one can do is to delete the elements once they reach a given failure strain. Therefore it is impossible to determine the amount of energy in the final fracture with the current numerical models. However, the final fracture probably occurs at a temperature of 700 °C, which results in the yield stress having a value of 11 % of the room temperature yield stress. If one assumes that the energy involved in the final fractured state is small due to the weak material properties, the energy involved in the final fracture can be approximated by the strain energy involved in the formation of the shear bands from the start of the blast until fracture due to the 200 % failure strain. It is difficult to determine the validity of this assumption.

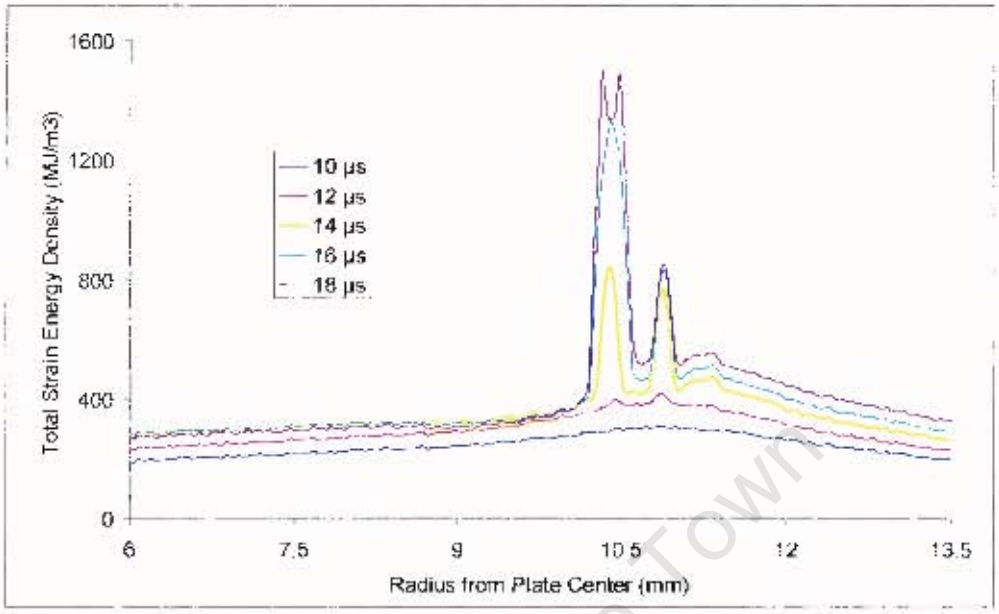

Figure 5.14: Strain Energy Along the Plate Midpoint for Different Times (Mesh Density of 0.04 x 0.04 mm).

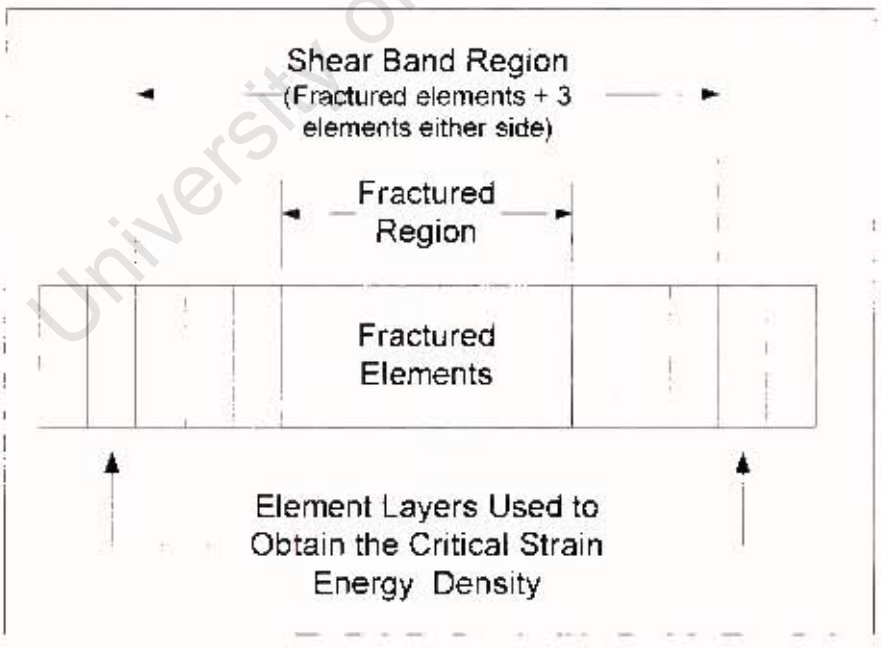

Figure 5.15: Defined Regions to Determine the Approximate Shear Band Energy.

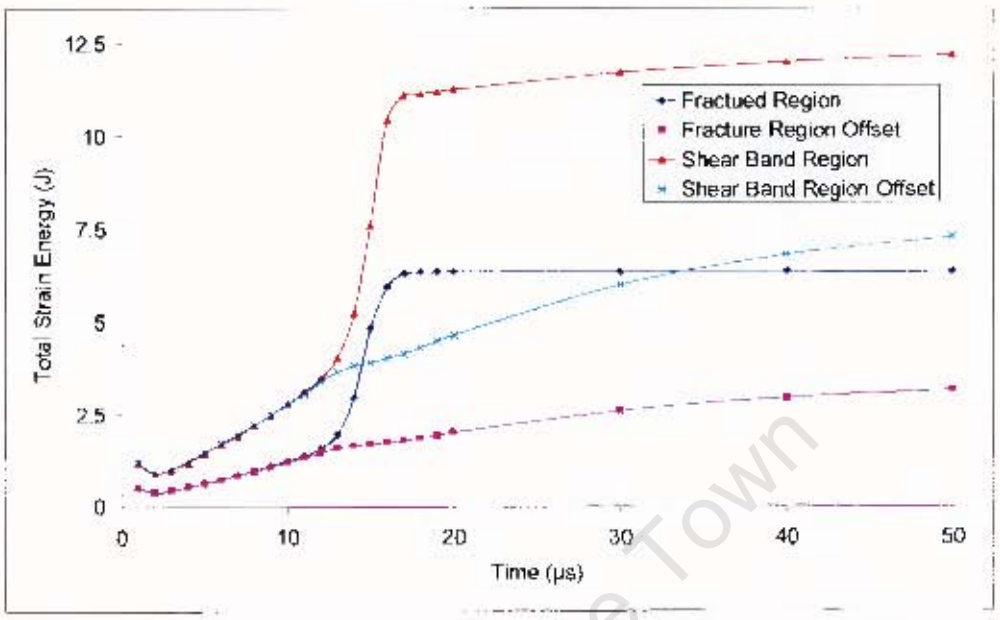

Figure 5.16: Total Strain energy in the Fractured and Shear Band Region.

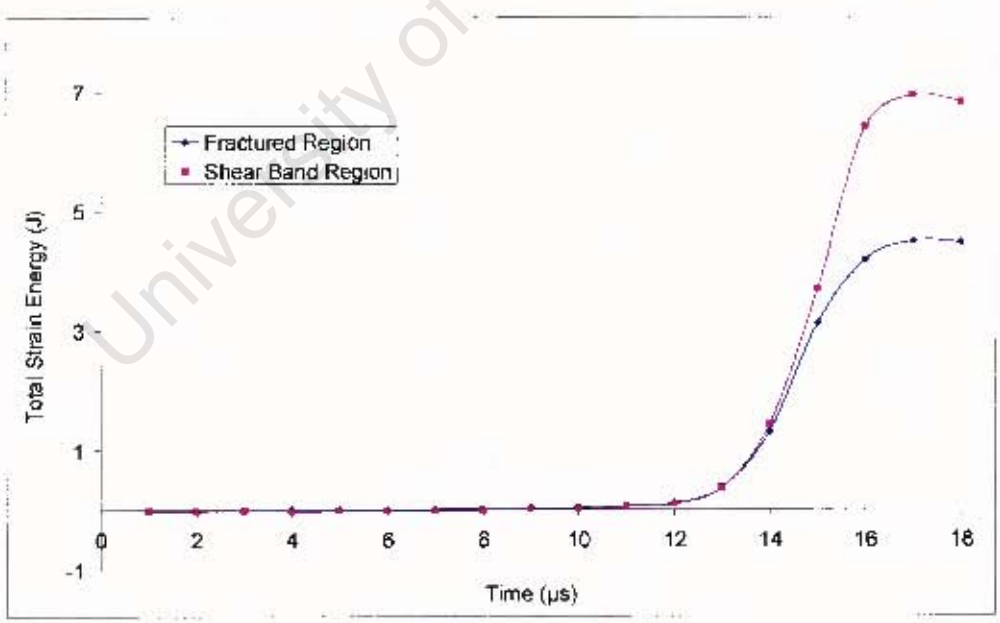

Figure 5.17: Additional Strain Energy Required to Form the Shear Band until the Point of Fracture.

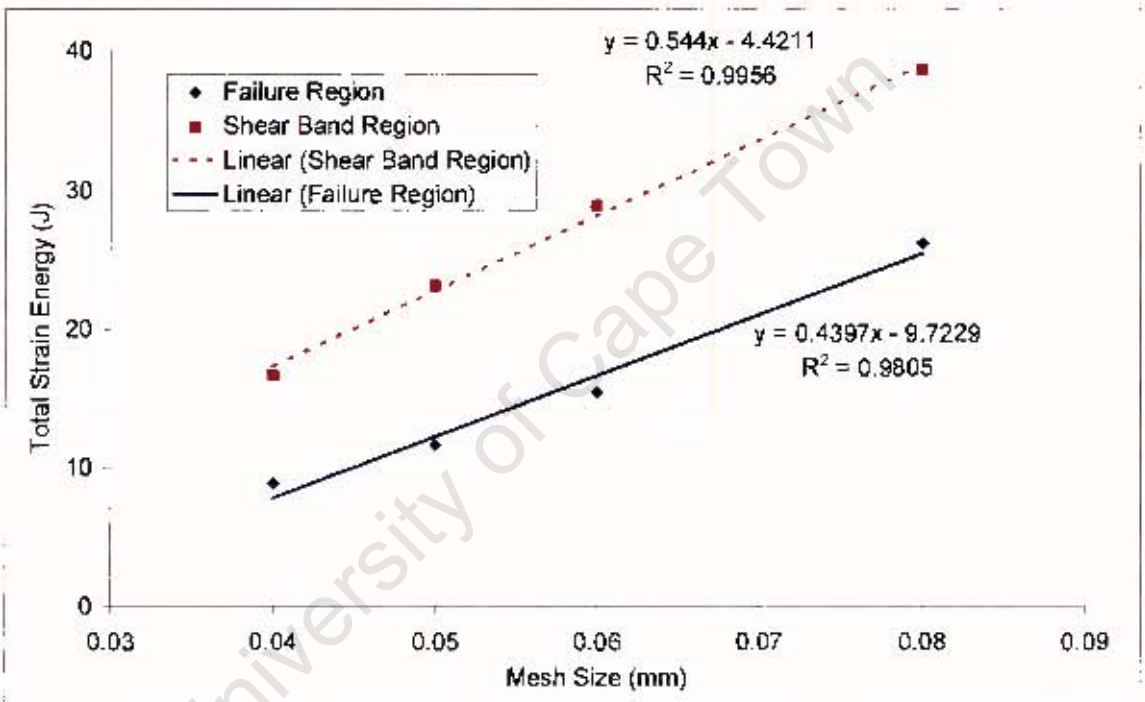

Figure 5.18: Effect of Mesh Density on Shear Band Strain Energy.

Chapter 6

CONCLUSIONS

6.1 MODELLING USING TEMPERATURE DEPENDENT MATERIAL PROPERTIES

Temperature dependent material properties were used for analysing plates subjected to blast loads. Different numerical results were obtained if a fine or coarse mesh was used. Both mesh densities had advantages.

6.1.1 COARSE MESHES

The following general conclusions can be made for the coarse mesh (element size of 1 x 0.292mm) that was used:

- The coarse mesh used was able to give good overall modelling results and was able to predict the onset of failure accurately.
- The coarse mesh used was unable to predict the exact method of failure. The mesh was unable to identify the formation of the shear bands.

6.1.2 FINE MESHES

Fine meshes (element size < 0.08 x 0.08 mm) were able to predict the formation of shear bands and determine the exact method of cap failure. However, the overall modelling performance was poor. This is thought to be due to the adiabatic finite element model used. The following conclusions can be made for fine meshes:

- Fine meshes are able to identify shear bands and explain the failure process of the plates.
- The overall modelling accuracy using fine meshes is poor.

6.2 INSIGHTS INTO THE METHOD OF FRACTURE

The numerical results show that the plate fracture appears to involve a thermo-mechanical cycle whereby increased strain at a localized location results in increased temperatures weakening the material properties resulting in even larger strains and temperatures. This process results in the formation of shear bands at angles of either 45° or 135° degrees to the angle of the deformed plate with a width of three elements. The degraded material properties result in unrealistic material properties indicating the occurrence of failure and make the task of choosing a critical failure strain for a strain based failure criteria a trivial matter for the simulations undertaken in this thesis. The fracture process occurs very quickly - $\pm 1 \mu s$ from first indication of a temperature localization in the form of a shear band until fracture is imposed by the 200 % failure strain.

6.3 THE ENERGY OF TEARING DURING CAPPING

Determining the amount of energy involved in the formation of the shear bands is a difficult task since the shear bands are mesh dependent. Therefore any energies obtained can only be regarded as order of magnitude results. Since final fracture occurs at over 700 °C severely weakening the material properties, it may be possible to assume that the energy of tearing can be approximated by the amount of energy required to form the shear band from the start of the blast to the time of fracture. If the above assumption is valid, ≈11 J of energy is required to form the fragment for a mesh density of 0.04 μm (the total strain energy of the shear band). This is approximately 0.7 % of the total energy applied to the plate and is 4.4 % of the experimentally measured fragment kinetic energy. This is a comparatively small amount of energy compared to the total plate strain energy and the fragment kinetic energy. The 11 J of energy required to tear the plate can only be regarded as an order of magnitude answer due to the mesh dependent nature of the shear bands and the assumptions used to obtain the energy of shear band formation.

6.4 CONCLUDING REMARK

Temperature dependent material properties are integral to the formation of shear bands and the subsequent fracture for thin circular plates subject to blast loads. Therefore any numerical modelling involving the fracture of metals subjected to blast loads should incorporate temperature dependent material properties. When fracture is modelled without temperature dependent material properties, a strain or stress based failure criterion is usually used. Small changes in the values of the failure criterions can have a large effect on the results of the simulations. From the results of this study it is seen that the structural performance is less sensitive to the choice of failure criterion when incorporating temperature dependence.

Chapter 7

RECOMMENDATIONS

7.1 RECOMMENDATIONS FOR FUTURE BLAST EXPERIMENTATION

Make the specimens using materials that have known material properties at high strain rates and temperatures. Copper is recommended for the following reasons:

- The material properties are well documented.
- It is isotropic.
- It does not undergo a phase change at high temperatures.
- It is easily obtainable.

7.2 RECOMMENDATIONS ON THE MODELLING OF DYNAMIC FRACTURE

- Use temperature dependent material properties when modelling fracture.
- Use an explicit code that allows temperature conduction between elements. This is particularly important when a fine mesh is used.
- Where possible model a material that has high strain rate and high temperature dependent material properties that are well documented in the literature.

7.3 WORK ON THE MODELLING OF THE EXPLOSION

- More work needs to be undertaken to determine the validity of using the JWL equation of state by applying a contact to contact boundary interaction between the explosive and the plate.
- The use of a constitutive model to simulate the explosive is still very desirable.

REFERENCES

[1] W. Q. Shen and M. Jones, Dynamic Response and Failure of Fully Clamped Circular Plates Under Impulsive Loading, International Journal of Impact Engineering **13**(2), 259–278 (1993).

[2] G. N. Nurick and M. W. Bryant, Fragment Damage as a Result of an Explosion, Plasticity and Impact Mechanics, Ed. N K Gupta, New Delhi, India, December 1996.

[3] G. N. Nurick and J. B. Martin, Deformation of Thin Plates Subjected to Impulse Loading- A Review Part II: Experimental Studies, International Journal of Impact Engineering **8**(2), 171–186 (1989).

[4] S. B. Menkes and H. J. Opat, Tearing and Shear Failure in Explosively Loaded Beams, Explosion Mechanics **13**, 480–486 (1973).

[5] R. G. Teeling Smith and G. N. Nurick, The deformation and Tearing of Thin Plates Subjected to Impulsive Loads, International Journal of Impact Engineering **11**(1), 77–91 (1991).

[6] G. N. Nurick and G. C. Shave, The deformation and Tearing of Thin Plates Subjected to Impulsive Loads - An Experimental Study, International Journal of Impact Engineering **18**(1), 99–116 (1996).

[7] G. N. Nurick and A. M. Radford, Deformation and Tearing of Clamped Circular Plates Subjected to a Localised Central Blast Load, Recent Development in Computational and Applied Mechanics, Ed. B D Reddy, A Volume in Honour of John B Martin, 1997.

[8] S. Chung Kim Yuen, The Effect of Plate Thickness on Localised Blast Loads, BSc Thesis, University of Cape Town, 1997.

[9] R. Bimha, Response of Thin Circular Plates to Blast Loading, Master's thesis, University of Cape Town, 1996.

[10] M. E. Gelman, A Numerical Study of the Response of Blast Loaded Thin Circular Plates, with Both Clamped and Integral Boundary Conditions, Master's thesis, University of Cape Town, 1996.

[11] G. H. Farrow, G. N. Nurick, and G. P. Mitchell, Modelling of Impulsively Loaded Circular Plates Subject to Impulsive Loads, Proc. 13th Symp. Finite Element Methods in South Africa, 1995.

[12] W. P. Grobbelaar, Modeling of Fragmentation Damage, Bsc Thesis, University of Cape Town, 1996.

[13] Habbit, Karlson and Sorenson, INC, *ABAQUS/Explicit Example Problems Manual*, v5.8 edition, 1998.

[14] W. P. Grobbelaar, An Investigation of Structures Subjected to Blast Loads Incorporating an EQS to Model the Material Behaviour of the Explosive, Implast 2000. The 7th Symposium on Structural Failure and Plasticity, Melbourne, Australia, October 2000.

[15] A. M. Radford, Deformation and tearing of clamped circular plates Subjected to Localised Blast Loads, Master's thesis, University of Cape Town, 1995.

[16] Habbit, Karlson and Sorenson, INC, *ABAQUS/Explicit Users Manual*, v5.8 edition, 1998.

[17] T. Masui, T. Nunokawa, and T. Hiramatsu, Shape Correction of Hot Rolled Steel Using an on Line Leveller, Journal of Japan Society for Technology of Plasticity, Journal of Japan Society for Technology of Plasticity (J) (1987).

[18] H. Rogers and C. Shastry, *Shock Waves and High Strain Rate Phenomena in Metals: Concepts and Applications*, Plenum Press, 1981.

[19] L. S. Costin, E. E. Crisman, and J. Duffy, Mechanical Properties of Materials at High Rates of Strain, Journal of Hardening , 90–100 (1979).

[20] E. Irick, C. Heinol, T. Clayton, J. Hashemi, and J. F. Cardenas-Garcia, Numerical and Experimental Investigation of Adiabatic Shear Bands in Metals Under Low-Velocity Impact Conditions, Journal of Materials Engineering and Performance **4**(6), 709–716 (1995).

[21] A. Molinari, Collective Behaviour and Spacing of Adiabatic Shear Bands, Journal of the Mechanics and Physics of Solids **45**(9), 1551–1575 (1997).

[22] T. G. Shawki and R. J. Clifton, Shear Band Formation in Viscoplastic Materials, Mechanics of Materials **8**, 13–43 (1989).

[23] T. W. Wright and H. Ockendon, A Model for Fully Formed Shear Bands, Journal of the Mechanics and Physics of Solids **40**, 1217–1226 (1992).

[24] L. Seaman, D. R. Curran, and D. A. Shockley, Scaling of Shear Band Fracture Processes, Materials Under High Stress and Ultrahigh Loading Rates , 295–307 (1983).

[25] M. Pastor, C. Rubio, and P. Mira, Shear Band Computations: Influence of Mesh Alignment, Computer Methods and Advances in Geomechanics , 2681–2687 (1995).

[26] M. Zhou, A. J. Rosakis, and G. Ravichandran, Dynamically Propagating Shear Bands in Impact-Loaded Prenotched Plates-I. Experimental Investigations of Temperature Signatures and Propagation Speed, Journal of the Mechanics and Physics of Solids **44**, 981–1006 (1996).

[27] G. Gioia and M. Ortiz, The Two-Dimensional Structure of Dynamic Shear Bands in Thermoviscoplastic Solids, Journal of the Mechanics and Physics of Solids **44**, 251–292 (1996).

[28] J. A. DiLellio and W. E. Olmstead, Temporal Evolution of Shear Band Thickness, Journal of the Mechanics and Physics of Solids **45**(3), 345–359 (1997).

[29] W. Wang, *Stationary and Propagative Instabilities in Metals - A Computational Point of View*, Delft University Press, 1997.

[30] C. G. Lee, W. J. Park, S. Lee, and K. S. Shin, Micro Structural Development of Adiabatic Shear Bands Formed by Ballistic Impact in a Welldlite 049 Alloy, Metallurgical and Materials Transactions A **29A**, 447–483 (1998).

[31] M. Zhou, A. J. Rosakis, and G. Ravichandran, Dynamically Propagating Shear Bands in Impact-Loaded Prenotched Plates-II. Numerical Simulations, Journal of the Mechanics and Physics of Solids **44**, 1007–1032 (1996).

[32] Habbit, Karlson and Sorenson, INC, *Getting Started with ABAQUS/Explicit*, 1998.

[33] N. Jones, *Structural Impact*, Cambridge University Press, Cambridge, 1989.

[34] G. R. Johnson and W. H. Cook, A Constitutive Model and Data Formetals Subjected to Large Strains, High Strain Rates and High Temperatures, Proc. 7th Symp. Ballistics, 1983.

[35] J. P. Holman, *Heat Transfer 7th Ed.*, McGraw-Hill Inc., UK, 1992.

[36] Habbit, Karlson and Sorenson, INC, *ABAQUS/Post Manual*, v5.8 edition, 1998.

[37] Habbit, Karlson and Sorenson, INC, *ABAQUS Theory Manual*, v5.8 edition, 1998.

Appendix A

MEASUREMENT OF THE APPLIED IMPULSE

The impulse is given by the equation:

$$I = M\,\dot{x}_o \tag{A.1}$$

where M is the total mass of the pendulum with all its attachments and $\dot{x}_o$ is the initial velocity of the pendulum.

The equation of motion for a pendulum is assumed to be given by the equation:

$$M\frac{d^2x}{dt^2} + C\frac{dx}{dt} + \frac{M}{R}gx = 0 \tag{A.2}$$

where x is the horizontal displacement, C is the damping coefficient and R is the radius of the pendulum motion.

If $\beta = \frac{C}{2M}$, $w_d = \frac{2\pi}{t}$ and T is the period of the pendulum then the solution to Equation A.2 is:

$$x = e^{-\beta t} \frac{\dot{x}_o}{w_d} \sin(w_d t) \tag{A.3}$$

where β is the damping constant and w_d is the pendulum frequency.

If $x_1$is the horizontal displacement at time $t = \frac{T}{4}$ and x_2 is the horizontal displacement at time $t = \frac{3T}{4}$, then solving Equation A.3 for x_1 and x_2 :

$$x_1 = e^{-\beta T/4} \dot{x}_o \frac{T}{2\pi} \tag{A.4}$$

$$x_2 = e^{-3\beta T/4} \dot{x}_o \frac{T}{2\pi} \tag{A.5}$$

The relationship between two successive amplitudes is given by the equation:

$$\frac{x_1}{x_2} = e^{\frac{1}{2}\beta T} \tag{A.6}$$

therefore:

$$\beta = \frac{2}{T} \ln \frac{x_1}{x_2} \tag{A.7}$$

The initial pendulum velocity can be found by substituting Equation A.7 into Equation A.4:

$$\dot{x}_n = x_1 \frac{2\pi}{T} e^{3\pi/4} \tag{A.8}$$

Appendix B

EXPERIMENTAL RESULTS

The results of all the experimental blasts undertaken are given in Table B.1. The keys used in the table are:

n/m - not measured

PD - Plastic Deformation

Cap - Capped

T - Tearing in the region of the cap

ST - Plastic deformation with a small crack in the region of capping

H - The plate's cap is still attached to the plate

Table B.1: EXPERIMENTAL RESULTS

Plate No	Thickness (mm)	Explosive mass (g)	Impulse (Ns)	Midpoint Deflection (mm)	Cap Mass (g)	Cap Velocity (m/s)	Note
T1	1.49	6.3	11.6		n/m	n/m	Blast
T2	1.57	6.3	11.0	–	n/m	n/m	H
T3	1.52	1.3	8.26	–	n/m	n/m	Cap
T4	1.62	0	0.79	n/m		–	PD
T5	1.67	3.8	7.13	18.7	–	–	PD
T6	1.61	3.5	6.66	20.6	–	–	PD
T7	1.97	4.5	8.63	17.1		–	PD
T9	1.72	6	9.78		2.75	n/m	Cap
T10	1.75	6	10.4		3.69	293.7	Cap
T11	1.55	5	8.95		3.5	333.2	Cap
T12	1.83	6.25	10.9	–	2.87	310.4	Cap
T13	1.72	4.48	8.61	23.3	–	–	PD
T14	1.69	4.58	8.20	–	–	–	H
T15	1.78	5.48	10.2	24.5	–		ST
T16	1.8	6.11	11.2		3.91	282.3	Cap
T17	1.65	5.45	10.4	–	–	–	T
T18	1.73	7.01	11.9	–	3.65	402.9	Cap
T19	1.73	4.56	9.84	24.8	–	–	PD
T20	1.79	6.52	11.9		2.46	n/m	Cap
T21	1.69	5.4	10.2	–	3.21	n/m	Cap

Appendix C

VELOCITY DATA

This section contains the data and method of determining the fragment velocity. A print out of one of the oscilloscope readings is given in Figure C.1. The x axis denotes time and the y axes denotes voltage. Unfortunately, the oscilloscope printer was not working properly, hence the reason for the four different channels starting at different time positions. However, the sharp drop in voltage which occurs when a wire is broken can be seen in the figure. Table C.1 contains the time at which the wires were broken with respect to the first wire. The distance between the wires with respect to the first wire is also given. Figure C.2 shows a graph of the fragment position history. The measured velocity is the gradient of the best fit line through each set of data.

Table C.1: FRAGMENT POSITION TIME HISTORY

Test No	Wire Number and Distance From the First Wire			
	First (0 mm)	Second (30.6 mm)	Third (60.8 mm)	Fourth (90.8 mm)
$T10$	0.0 μs	107 μs	203 μs	324 μs
$T11$	0.0 μs	89.2 μs	178 μs	273 μs
$T12$	0.0 μs	106 μs	196 μs	
$T16$	0.0 μs	110 μs	220 μs	327 μs
$T18$	0.0 μs	75.0 μs	152 μs	225 μs

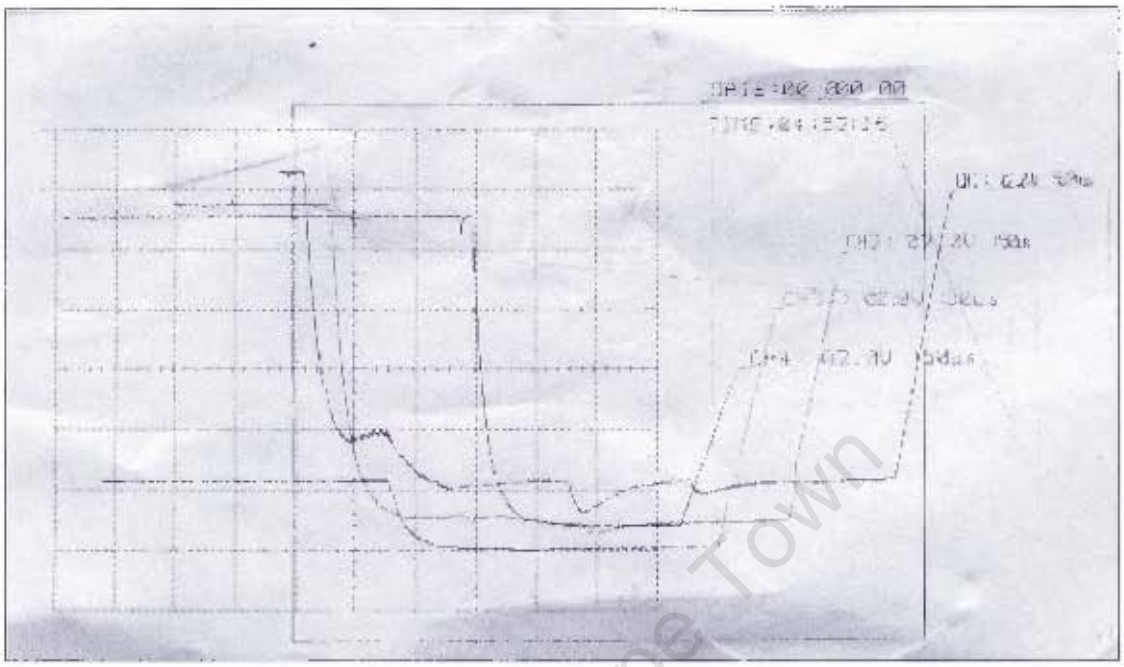

Figure C.1: Example of an Oscilloscope Reading.

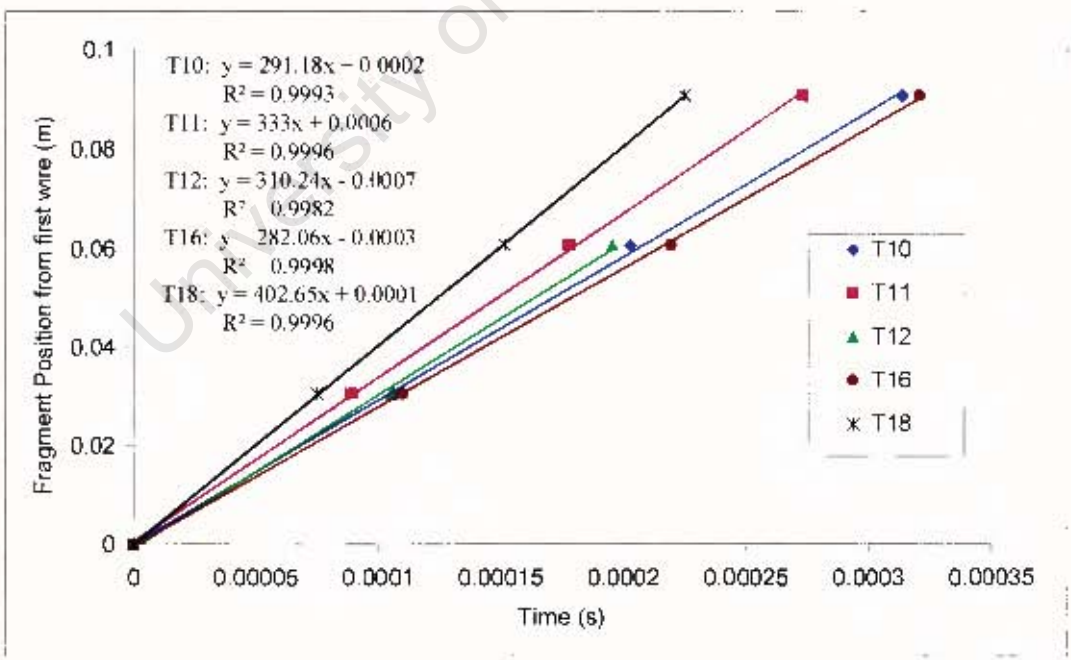

Figure C.2: Fragment Position Time History.

The path of the fragment is known because the fragment deforms the fragment trajectory plate marking its path (see Figure C.3). The radial offset distance is the distance between the measured path and a perpendicular path from the centre of the plate measured using the fragment trajectory plate which is 184 mm from the plate centre. A trajectory offset can be determined using the radial offset enabling the true fragment velocity to be obtained. The offset angle and the true velocity is given in Table C.2.

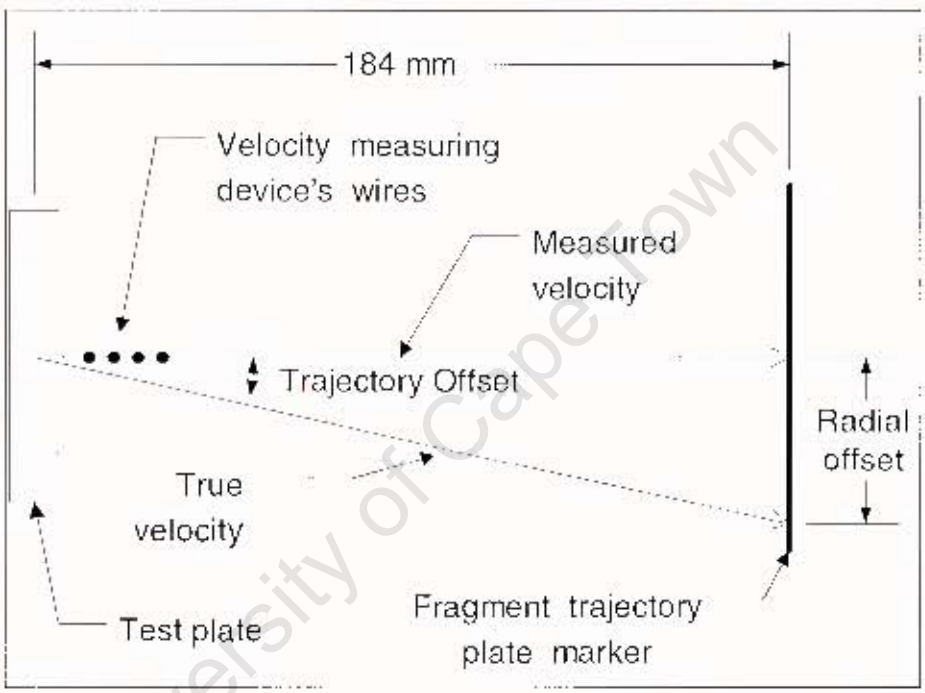

Figure C.3: Velocity Diagram Showing the Measured and True Velocity.

Table C.2: TRUE FRAGMENT VELOCITY

Test No	**Measured Velocity** (m/s)	**Radial Offset** (mm)	**Trajectory Angle Offset** (°)	**True Velocity** (m/s)
T10	291.2	24	7.43°	295.1
T11	333	7	0.04°	333
T12	310.2	6	0.03°	310.2
T16	282.1	7.3	0.04°	282.1
T18	402.7	9	0.05°	402.7

Appendix D

THE JWL EQUATION OF STATE

This appendix explains the use of the JWL equation of state, the results obtained and the unexplained phenomenon of providing bad impulses despite having acceptable displacement results.

D.1 THE FEM MODEL

The equation of state was modelled using the method developed by Grobbelaar at the University of Cape Town. The explosive was modelled using the CAX4R axisymmetric four noded elements with JWL equation of state material properties. The use of both the standard kinematic contact algorithm and the penalty contact interaction was initiated between the explosive and the plate's top surface.

D.2 JWL MATERIAL PROPERTIES

In order to model the JWL equation of state, ABAQUS/Explicit requires the material constants as explained in Equation 2.15. The material constants are given in Table D.1. The units are given commonly used units in the explosive field namely, *Mbar*,

Table D.1: JWL EQUATION OF STATE MATERIAL PROPERTIES

JWL Equation of State Constants	Value
Detonation Wave Speed - C_d	$0.819\,\mathrm{cm}\,\mu s$
JWL Constant - A	$6.0977\,Mbar$
JWL Constant - B	$0.1295\,Mbar$
JWL Constant - ω	0.25
JWL Constant - R_1	4.5
JWL Constant - R_2	1.4
Internal Energy per unit volume - E_{mo}	$0.09\,\mathrm{g}\,\mu s^{-2}\,\mathrm{cm}^{-1}$

cm, μs, and g. The density of the explosive is $1600\,\mathrm{kg\,m}^{-3}$. The detonation point of the explosive is the explosive centroid.

D.3 COMPARISON BETWEEN THE DIFFERENT CONTACT METHODS

Initial runs using the JWL equation of state yielded inconsistent displacements depending on the number of elements used to model the explosive. A parametric study was then undertaken to determine the effect of explosive mesh density on the effect of the centre plate displacement for both the kinematic contact algorithm and the penalty contact method. This study involved changing the number of elements in the explosive from 4 x 4 to 20 x 20. The results of this study can be seen in Table D.2 for the standard contact interaction and Table D.3 for the penalty contact method. In some cases the jobs were unable to finish due to excessive element deformation and are denoted by "-" in the table.

The normal contact method is very dependent on the mesh density. The use of 18 x 18 elements as opposed to 16 x 16 elements results in an increase in the plate midpoint displacement of 26.3 %. The penalty contact method provides a more consistent

Table D.2: MIDPOINT PLATE DISPLACEMENT USING THE NORMAL CONTACT METHOD

Number of elements along the the plate	Number of Elements above the Plate								
	4	6	8	10	12	14	16	18	20
4	1.72	1.77	2.17	2.06	2.08	2.44	2.79	–	–
6	1.76	1.81	2.03	2.13	2.17	2.34	2.76	2.63	4.64
8	1.84	1.84	2.14	2.16	2.65	2.55	2.48	2.74	6.99
10	1.69	1.99	2.43	2.24	2.51	2.84	3.55	3.28	
12	2.12	2.02	2.07	2.17	2.57	2.47	4.65	3.91	5.29
14	2.17	2.01	2.37	2.15	2.38	2.51	2.48		4.38
16	2.09	2.04	2.25	2.25	2.44	2.52	3.17	3.28	5.27
18	2.09	2.23	2.12	2.17	2.28	2.39	2.67	2.79	2.70
20	2.14	2.17	2.35		2.23	2.21	3.60	2.73	–

answer with less fluctuations between similar mesh densities.

D.4 DETERMINING THE IMPULSE

In order to further verify the equation of state, it was decided to compare the impulse obtained from the JWL EOS simulations with those obtained from experimentation.

D.4.1 OBTAINING THE IMPULSE FOR THE NUMERICAL SOLUTION

A free body diagram of the model is shown in Figure D.1.

The impulse is defined by the equation:

$$I = \int_0^T F dt \tag{D.1}$$

Table D.3: MIDPOINT PLATE DISPLACEMENT USING THE PENALTY CONTACT METHOD

Number of elements along the the plate	Number of Elements above the Plate								
	4	6	8	10	12	14	16	18	20
4	1.72	1.77	2.17	2.06	2.08	2.44	2.79	–	–
6	1.76	1.81	2.03	2.13	2.17	2.34	2.76	2.63	4.64
8	1.84	1.84	2.14	2.16	2.65	2.55	3.48	2.74	6.99
10	1.69	1.99	2.43	2.24	2.51	2.84	3.55	3.28	–
12	2.12	2.02	2.07	2.17	2.57	2.47	4.65	3.91	5.29
14	2.17	2.01	2.37	2.15	2.38	2.51	2.48		4.38
16	2.09	2.04	2.25	2.25	2.44	2.52	3.17	3.28	5.27
18	2.09	2.23	2.12	2.17	2.28	2.39	2.67	2.79	2.70
20	2.14	2.17	2.35		2.23	2.21	3.00	2.73	–

The impulse in the 2 direction is found by substituting the reaction force $F_{Boundary_2}(t)$ into Equation D.1:

$$I_2 = \int_0^T F_{Boundary_2}(t)dt \tag{D.2}$$

ABAQUS is able to provide the boundary forces for the boundary nodes. Therefore the total reaction force is found by summing all of the reaction forces of the boundary nodes in the 2 direction:

$$F_{Boundary_2}(t)dt = \sum_{n=1}^{Boundary\ Nodes} F_{Boundary_{2_n}}(t)dt \tag{D.3}$$

where $F_{Boundary_{2_n}}$ is the boundary force of boundary node n in the 2 direction. Substituting Equation D.3 into Equation D.2 gives:

$$I_2 = \int_0^T \sum_{n=1}^{Boundary\ Nodes} F_{Boundary_{2_n}} dt \tag{D.4}$$

Due to the symmetry of the problem, the reaction forces in the 1 direction cancel out.

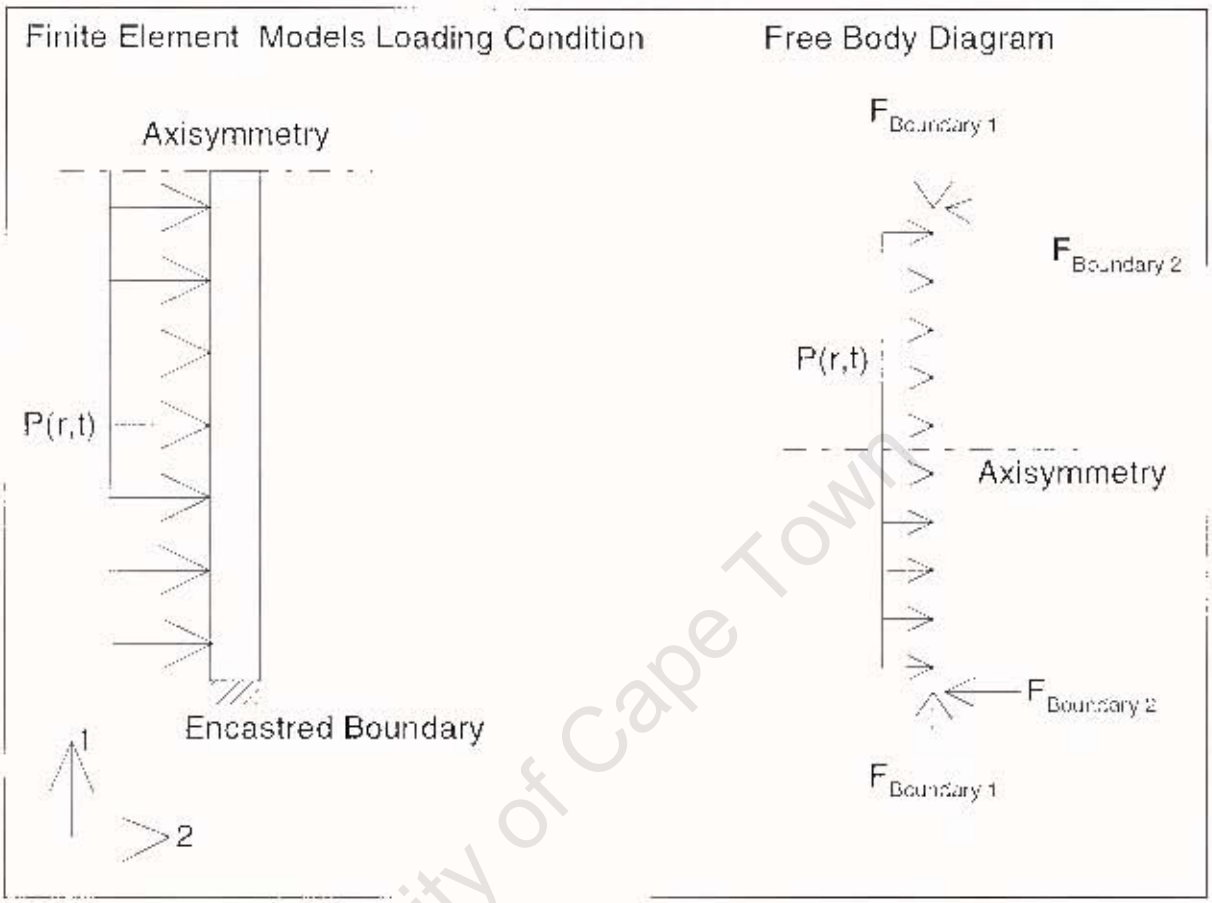

Figure D.1: Free Body Diagram of the Finite Element Model.

D.4.2 IMPULSE RESULTS

A graph of the impulse as a function of time for both the JWL EOS and the method of applying a pressure to simulate the blast is given in Figure D.2 for plate T5.

The oscillations of the graph is due to the lack of damping in the model. The impulse was obtained by finding the average between two periods (t = 346.2 - 661.8 μs for the EOS) giving a result of 3.5 N s for the equation of state. Using the method of applying a pressure to model the blast, an impulse of 6.89 N s was obtained. An experimental impulse of 7.13 N s was obtained resulting in a difference of 49.1 % between the equation of state and the experimental value. The method of applying a pressure to

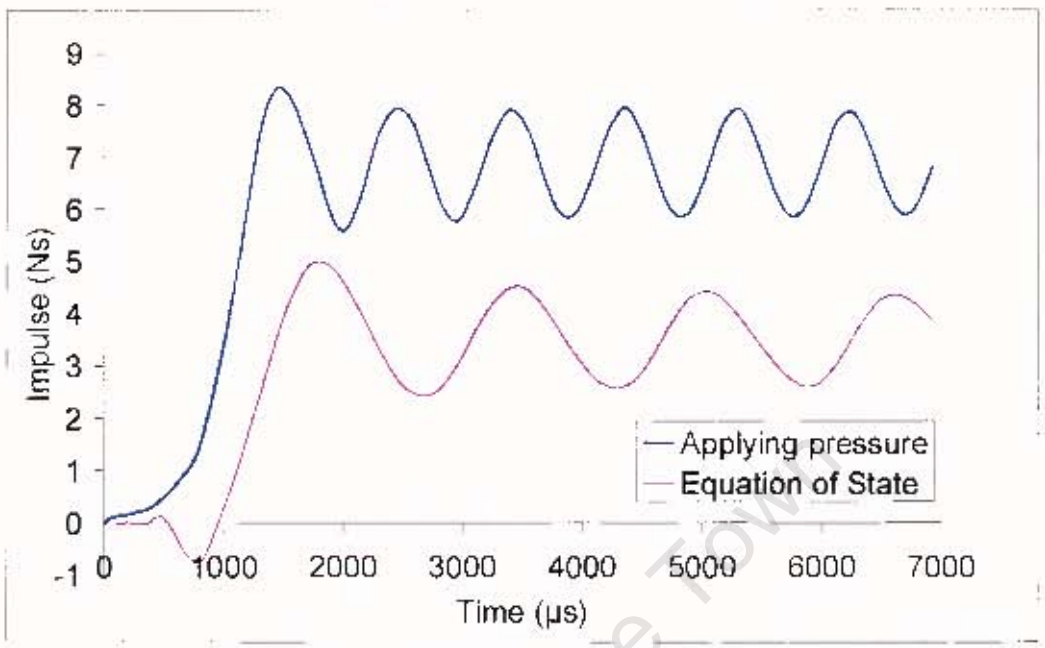

Figure D.2: Impulse Obtained for Different Methods of Modelling the Blast.

simulate the blast results in 0.4 % difference from the experimental value verifying the method of calculating the impulse.

It must be noted that the equation of state provides reasonable displacement profiles [14] although it does have a tendency to under predict the displacement profiles of the capped plates. However the slight under prediction of the displacement profiles can not explain the large discrepancy in the impulse between the equation of state and the experimental values. An incorrect pressure distribution may result from faulty EOS material properties or the approximated force balance obtained using a "contact to contact interaction" between the explosive and the plate as opposed to a more correct shock to shock interaction. An incorrect pressure distribution due to the JWL EOS can result in acceptable displacements even though the impulse may be poor. It is also possible that ABAQUS/Explicit may be giving incorrect reaction forces when the EOS is being used.

D.5 CONCLUSION

The JWL equation of state is able to give acceptable displacement profiles. When the JWL EOS is being used, the penalty contact method should be applied as it gives a more consistent solution. However, the impulse measured using the JWL equation of state does not compare well with experimentation. More work should be undertaken to validate the use of the EOS when a "contact to contact" interaction occurs between the explosive and a plate.

Appendix E

GRAPHS OF THE OPTIMUM EXPONENTIAL DECAY

This appendix compares the displacement profile of the numerical and experimental data for the optimally determined exponential decay of the plastically deformed plates T5, T6 and T7. The optimum exponential decay for each plate was chosen by minimising the residual sum of squares between the experimental and numerical data. The displacement profiles are given in Figures E.1, E.2 and E.3. The solid line represents a best fit polynomial line for the experimental data.

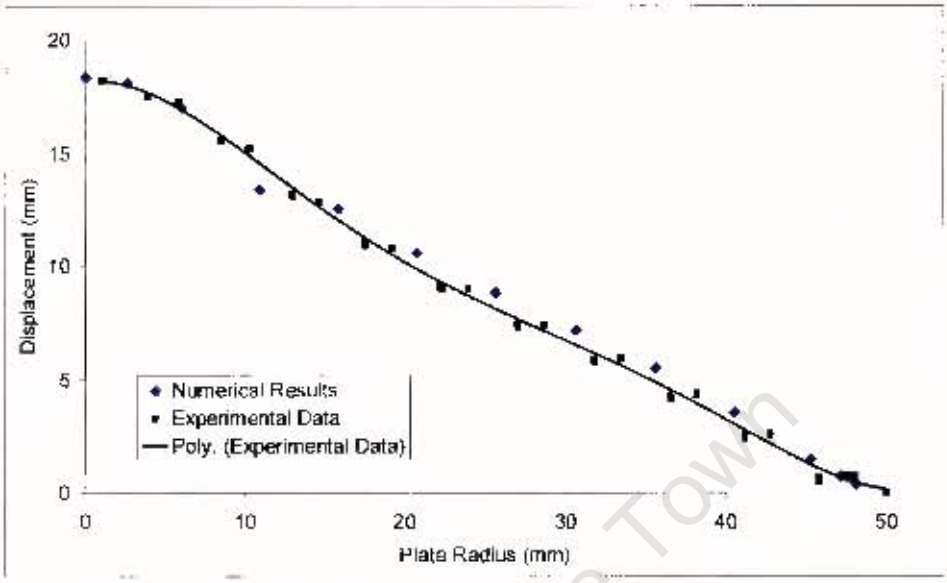

Figure E.1: Optimum Displacement Profile for Plate T5 (k=1.1).

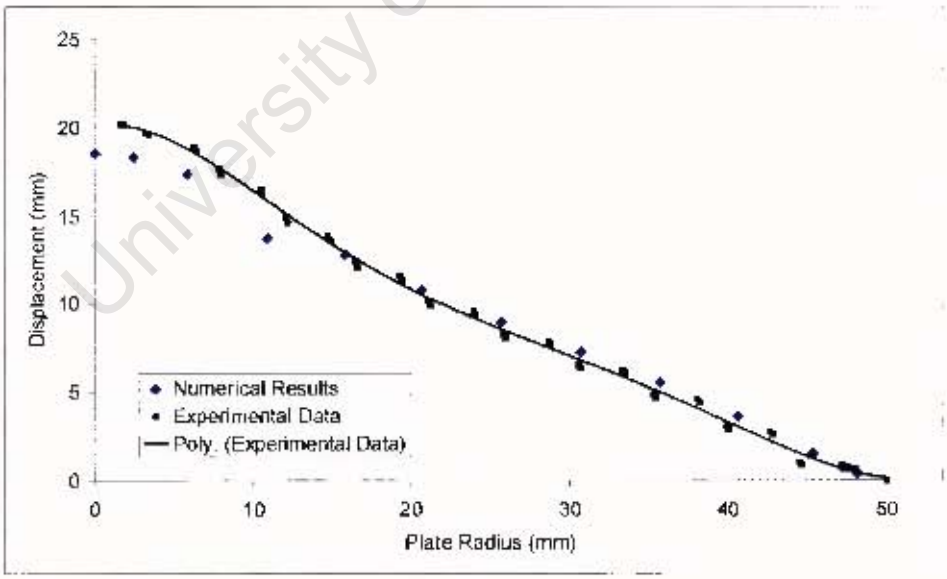

Figure E.2: Optimum Displacement Profile for Plate T6 (k=1.3).

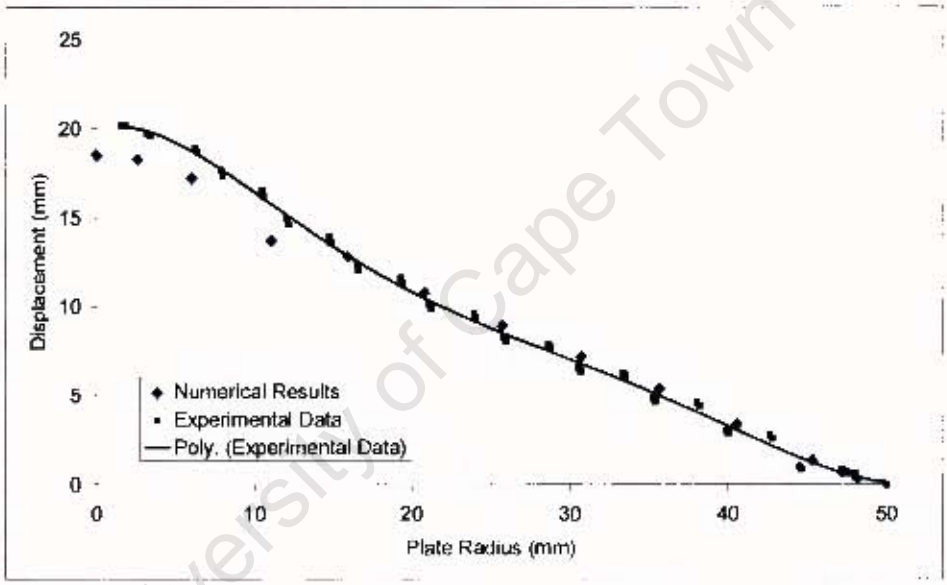

Figure E.3: Optimum Displacement Profile for Plate T7 (k=1.15).

Appendix F

USER SUBROUTINE VDLOAD

This is the user subroutine that applies the blast pressure for the numerical model. It is configured for plate 710 using an exponential decay of 1.2. It is programed in Fortran 77.

```
subroutine vdload (nblock, ndim, stepTime, totalTime,
1 amplitude, curCoords, velocity, dirCos, jtyp,
2 value )
C
include 'vaba_param.inc'
dimension curCoords(nblock,ndim), velocity(nblock,ndim),
1 dirCos(nblock,ndim,ndim), value(nblock)
C
do 100 km = 1, nblock
if (totalTime.lt.2.0D0) then
if (curCoords(km,1).lt. 1.25D0) then
```

```
value(km)=0.033726D0
else
value(km) = (EXP(-1.2D0*(curCoords(km,1)-1.25D0)))*0.033726D0
end if
else
value(km)=0.0D0
end if
100 continue
return
end
```

Appendix G

ABAQUS/EXPLICIT INPUT DECKS

Many different input decks were used for the different mesh densities and for each plate. Each configuration required a separate input deck. The blast pressure is applied using a user subroutine VDLOAD given in Appendix F. An example of a coarse mesh and a fine mesh for plate $T10$ is given in this appendix.

G.1 COARSE MESH EXAMPLE

*HEADING

Plate T10 using support boundary conditions with a mesh density of 1x0.04 mm.

Units: Length cm, mass g, time μs and temperature °C

****

PLATE -50x6,EXPLOSIVE 12x8

Run time=1000

```
ENCLAMPED BOUNDARY CONDITION
**************************************
** NODES AND ELEMENTS FOR THE PLATE
**************************************
*NODE
1 , 0.0 , -0.0875
101 , 5.0 , -0.0875
1601 , 5.0 , 0.0875
1501 , 0.0 , 0.0875
*NGEN,NSET=BOTTOM
1, 101 ,2
*NGEN,NSET=TOP
1501,1601,2
*NFIL,NSET=NPLATE
BOTTOM,TOP,6,250
*NGEN,NSET=INR
1,1501,250
*NGEN,NSET=OUTR
101,1601,250
*NSET,NSET=MD
751,840,850
*SOLID SECTION, ELSET=PLATE,MATERIAL=STEEL
```

```
*ELEMENT,TYPE=CAX4R,ELSET=PLATE
1, 1, 3, 253, 251
*ELGEN, ELSET=PLATE
1 ,50 ,2 ,2 , 6, 250, 250
** The pressure is applied on elset PL
*ELSET,ELSET=PL,GENERATE
1251,1349,2
**********************************
** NODES AND ELEMENTS FOR THE SUPPORT
**********************************
*NODE
100001, 5.0 ,-0.2625
118001, 5.0 , 0.2625
100006, 5.525,-0.2625
118006, 5.525, 0.2625
*NGEN,NSET=HINR
100001, 118001 ,1000
*NGEN,NSET=HOUTR
100006, 118006,1000
*NFIL,NSET=NHOLDER
HINR,HOUTR,5,1
*SOLID SECTION, ELSET=HOLDER,MATERIAL=STEEL
```

```
*ELEMENT,TYPE=CAX4R,ELSET=HOLDER
100001 , 100001,100002,101002,101001_
*ELGEN,ELSET=HOLDER
100001,5,1,1,18,1000,1000
*NSET,NSET=HJOIN,GENERATE
106001,112001,1000
*NSET,NSET=HTOP,GENERATE
118001,118006,1
*NSET,NSET  HBOTTOM,GENERATE
100001,100006,1
**********************************
** MATERIAL PROPERTIES
**********************************
*MATERIAL, NAME=STEEL
*SPECIFIC HEAT
452.0E-8
*DENSITY
7.846
*SHEAR FAILURE
2.0
*INELASTIC HEAT FRACTION
*ELASTIC
```

2.1,0.3,0

1.75,0.3,600

1.46,0.3,700

1.249,0.3,800

1.094,0.3,900

1.001,0.3,1000

0.97,0.3,1100

*PLASTIC

0.00181,0,0

0.002,0.005,0

0.00249,0.024,0

0.003,0.047,0

0.0035,0.08,0

0.004,0.136,0

0.00426,0.184,0

0.00444,0.241,0

0.00181,0.200

0.002,0.005,200

0.00249,0.024,200

0.003,0.047,200

0.0035,0.08,200

0.004,0.136,200

0.00426,0.184,200

0.00444,0.241,200

0.0001991,0.700

0.00022,0.005,700

0.0002739,0.024,700

0.00033,0.047,700

0.000385,0.08,700

0.00044,0.136,700

0.0004686,0.184,700

0.0004884,0.241,700

0.000030046,0,1000

0.0000332,0.005,1000

0.000041334,0.024,1000

0.0000498,0.047,1000

0.0000581,0.08,1000

0.0000664,0.136,1000

0.000070716,0.184,1000

0.000073704,0.241,1000

*RATE DEPENDENT

40.0E-6, 5.0

*INITIAL CONDITIONS,TYPE=TEMPERATURE

NPLATE,20.0

```
NHOLDER,20.0
**********************************
** BOUNDARY CONDITIONS
**********************************
*BOUNDARY
HOUTR,ENCASTRE
HTOP,ENCASTRE
HBOTTOM,ENCASTRE
INR,XSYMM
*MPC
TIE,OUTR,HJOIN
**********************************
** THE STEP CONDITIONS
**********************************
*RESTART, WRITE,NUMBER INTERVAL=20,TIME MARKS=YES
*STEP
*DYNAMIC, EXPLICIT,ADIABATIC
.50
*DLOAD
PL,P3NU,1.0
*END STEP
*STEP,NLGEOM=YES
```

*DYNAMIC, EXPLICIT,ADIABATIC

,800

*END STEP

G.2 FINE MESH EXAMPLE

*HEADING

Plate T10 using support boundary conditions with a mesh density of 0.04x0.04 mm.

Units: Length cm, mass g, time μs and temperature °C

****

** NODES AND ELEMENTS FOR THE PLATE

****

*NODE

1 , 0.0 , -0.0875

20 , 0.3 , -0.0875

54 , 0.6 , -0.0875

242 , 1.35, -0.0875

276 , 1.65, -0.0875

486 , 5.0 , -0.0875

44001 , 0.0 , 0.0875

44020 , 0.3 , 0.0875

44054 , 0.6 , 0.0875

44242 , 1.35, 0.0875

```
44276 , 1.65, 0.0875
44486 , 5.0 , 0.0875
*NGEN,NSET=INR
1, 44001 ,1000
*NGEN,NSET=OUTR
486,44486,1000
*NGEN,NSET=IIO
20, 44020 ,1000
*NGEN,NSET=IO
54,44054 ,1000
*NGEN,NSET=OI
242, 44242 ,1000
*NGEN,NSET=OOI
276,44276,1000
*NFIL,NSET=NPLATE
INR,IIO,19,1
*NFIL,NSET=NPLATE
IO,OI,188,1
*NFIL,NSET=NPLATE
OOI,OUTR,210,1
*NFIL,BIAS=1.04365,NSET=NPLATE
IIO,IO,34,1
```

```
*NFIL,BIAS=0.958176,NSET=NPLATE
O1,OO1,34,1
*SOLID SECTION, ELSET=PLATE,MATERIAL=STEEL
*ELEMENT,TYPE  CAX4R,ELSET=PLATE
1, 1, 2, 1002, 1001
*ELGEN, ELSET=PLATE
1 ,485 ,1 ,1 , 44, 1000, 1000
** The pressure is applied on elset PL
*ELSET,ELSET=PL,GENERATE
43001,43485,1
**************************************
** NODES AND ELEMENTS FOR THE SUPPORT
**************************************
*NODE
100001, 5.0 ,-0.2625
232001, 5.0 , 0.2625
100034, 5.525,-0.2625
232034, 5.525, 0.2625
*NGEN,NSET  HINR
100001, 232001 ,1000
*NGEN,NSET=HOUTR
100034, 232034,1000
```

*NFIL,NSET=NHOLDER

HINR,HOUTR,33,1

*SOLID SECTION, ELSET=HOLDER,MATERIAL=STEEL

*ELEMENT,TYPE=CAX4R,ELSET=HOLDER

100001 , 100001,100002,101002,101001

*ELGEN,ELSET=HOLDER

100001,33,1,1,132,1000,1000

*NSET,NSET=HTOP,GENERATE

232001,232034,1

*NSET,NSET=HBOT,GENERATE

100001,100034,1

*NSET,NSET=HJOIN,GENERATE

144001,188001,1000

****

** MATERIAL PROPERTIES

****

*MATERIAL, NAME=STEEL

*SPECIFIC HEAT

452.0E-8

*DENSITY

7.846

*SHEAR FAILURE

2.0

*INELASTIC HEAT FRACTION

*ELASTIC

2.1,0.3,0

1.75,0.3,600

1.46,0.3,700

1.249,0.3,800

1.094,0.3,900

1.001,0.3,1000

0.97,0.3,1100

*PLASTIC

0.00181,0,0

0.002,0.005,0

0.00249,0.024,0

0.003,0.047,0

0.0035,0.08,0

0.004,0.136,0

0.00426,0.184,0

0.00444,0.241,0

0.00181,0,200

0.002,0.005,200

0.00249,0.024,200

0.003,0.047,200

0.0035,0.08,200

0.004,0.136,200

0.00426,0.184,200

0.00444,0.241,200

0.0001991,0,700

0.00022,0.005,700

0.0002739,0.024,700

0.00033,0.047,700

0.000385,0.08,700

0.00044,0.136,700

0.0004686,0.184,700

0.0004884,0.241,700

0.000030046,0,1000

0.0000332,0.005,1000

0.000041334,0.024,1000

0.0000498,0.047,1000

0.0000581,0.08,1000

0.0000664,0.136,1000

0.000070716,0.184,1000

0.000073704,0.241,1000

*RATE DEPENDENT

```
40.0E-6, 5.0
*INITIAL CONDITIONS,TYPE=TEMPERATURE
NPLATE,20.0
NHOLDER,20.0
**********************************
** BOUNDARY CONDITIONS
**********************************
*BOUNDARY
INR,XSYMM
HTOP,ENCASTRE
HBOT,ENCASTRE
HOUTR,ENCASTRE
*MPC
TIE,OUTR,HJOIN
**********************************
** THE STEP CONDITIONS
**********************************
*RESTART, WRITE,NUMBER INTERVAL=20,TIME MARKS=YES
*STEP
*DYNAMIC, EXPLICIT,ADIABATIC
,10
*DLOAD
```

PL,P3NU,1.0

*END STEP

*STEP

*DYNAMIC, EXPLICIT,ADIABATIC

,10

*END STEP

*STEP

*DYNAMIC, EXPLICIT,ADIABATIC

,100

*END STEP

Appendix H

COARSE MESH RESULTS

ABAQUS simulations of both plastically deformed plates and capped plates were undertaken using a coarse mesh. The simulation temperature profiles of the plates are presented in this appendix.

H.1 PLASTICALLY DEFORMED PLATES

The temperature profiles of the plastically deformed plates $T5$, $T6$ and $T7$ are shown in Figures H.1 to H.3 using a coarse mesh. The temperature profiles are at a time of 0, 50, 100 and 200 μs after the start of the simulations.

H.2 CAPPED PLATES

Temperature profiles of the capped plates $T10$, $T11$, $T12$, $T16$ and $T18$ using a coarse mesh are shown in Figures H.4 to H.8. The figures contain temperature profiles at a time of 0, 50 and 100 μs after the start of the simulation.

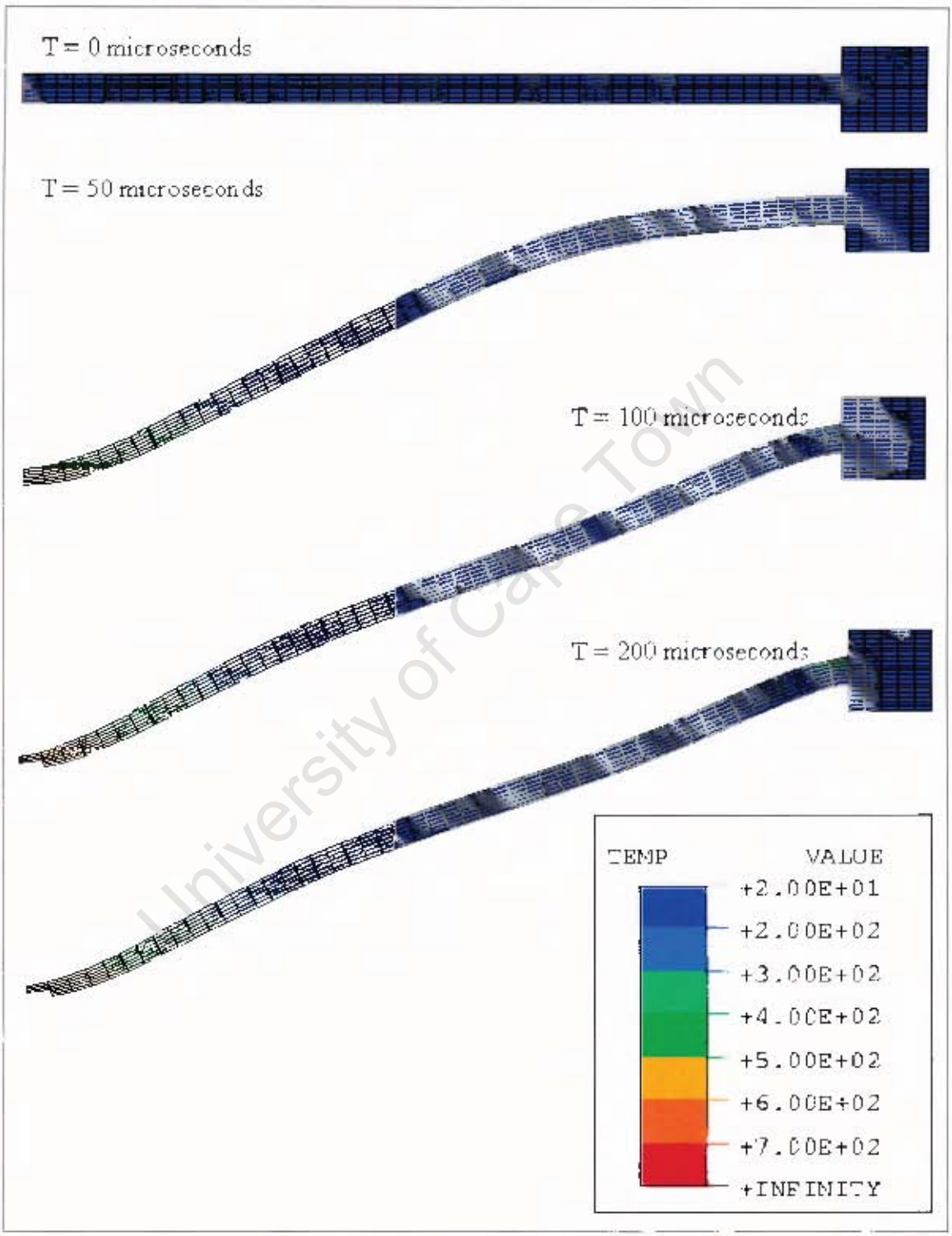

Figure H.1: Temperature Profiles of Plate T5 for a Mesh Density of 1 x 0.278 mm.

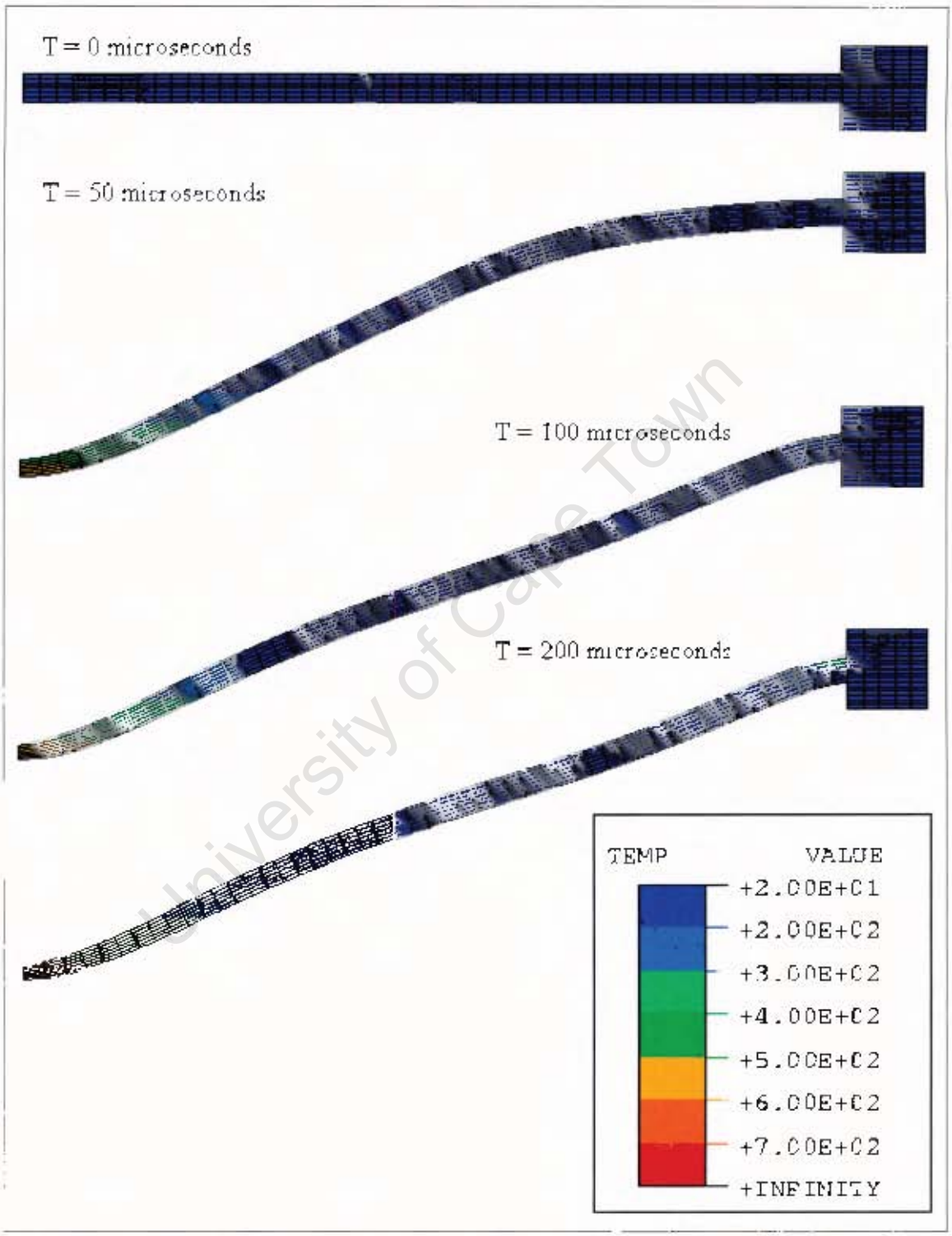

Figure H.2: Temperature Profiles of Plate T6 for a Mesh Density of 1 x 0.268 mm.

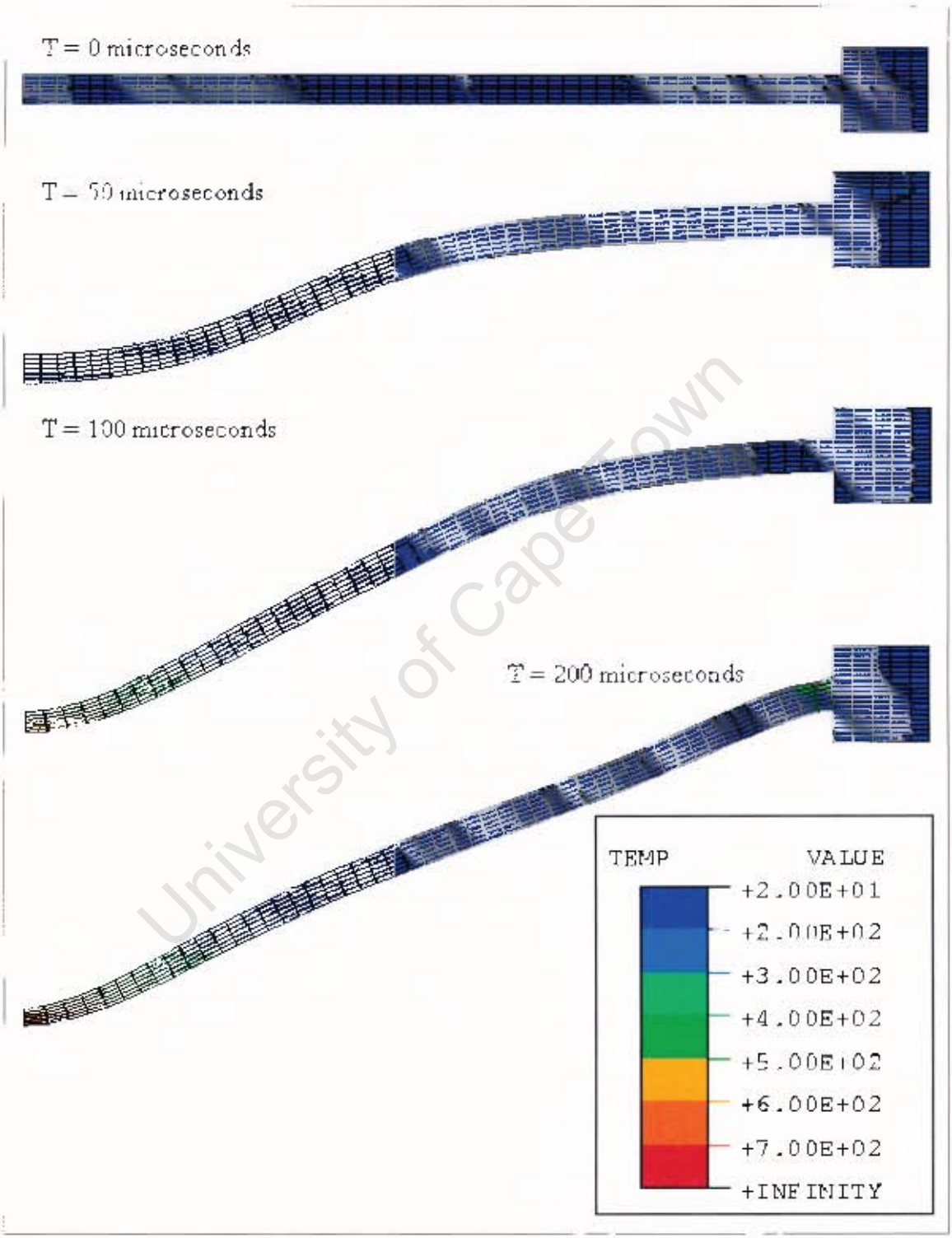

Figure H.3: Temperature Profiles of Plate T7 for a Mesh Density of 1 x 0.328 mm.

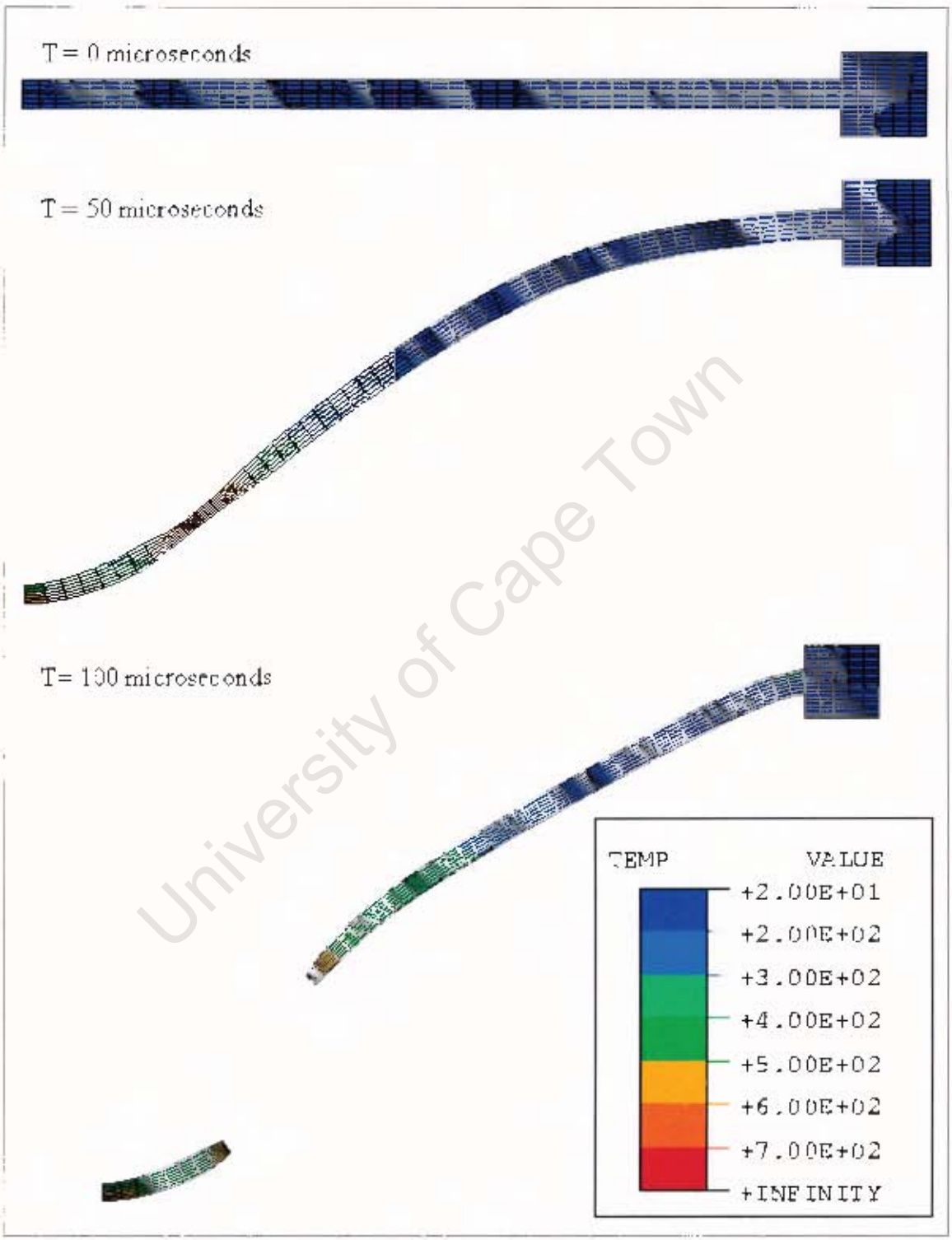

Figure H.4: Temperature Profiles of Plate T10 for a Mesh Density of 1 x 0.292 mm.

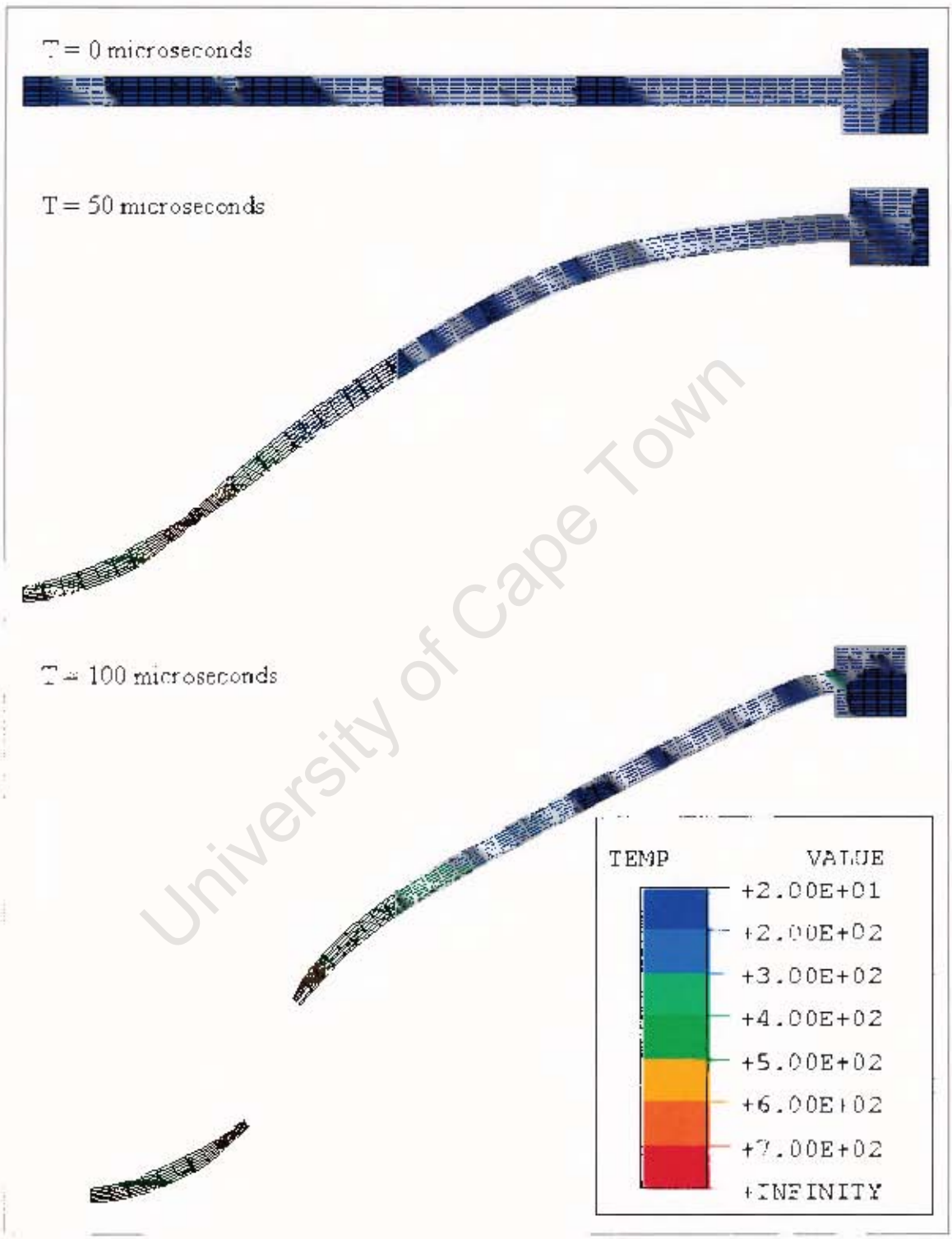

Figure II.5: Temperature Profiles of Plate T11 for a Mesh Density of 1 x 0.258 mm.

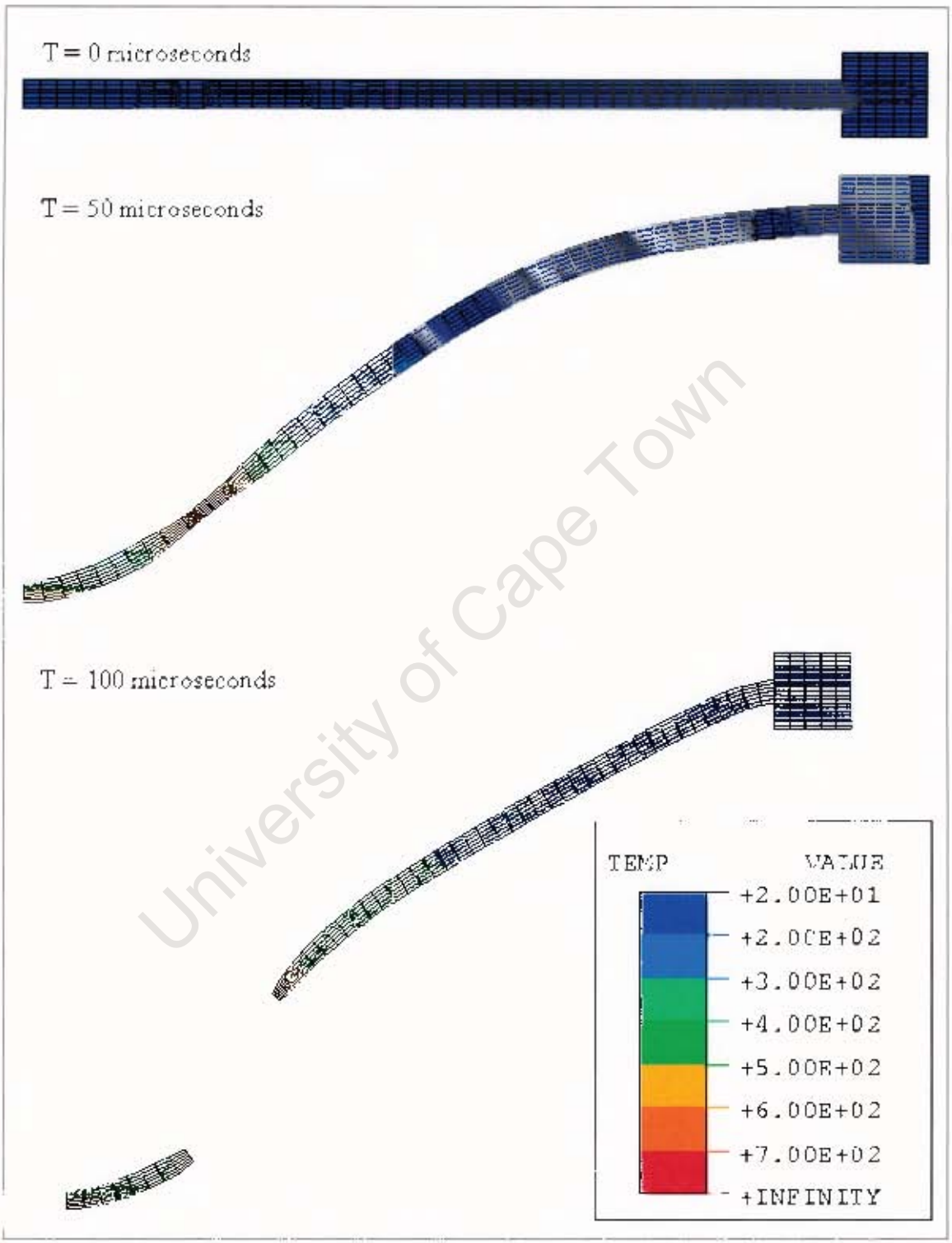

Figure II.6: Temperature Profiles of Plate T12 for a Mesh Mensity of 1 x 0.305 mm.

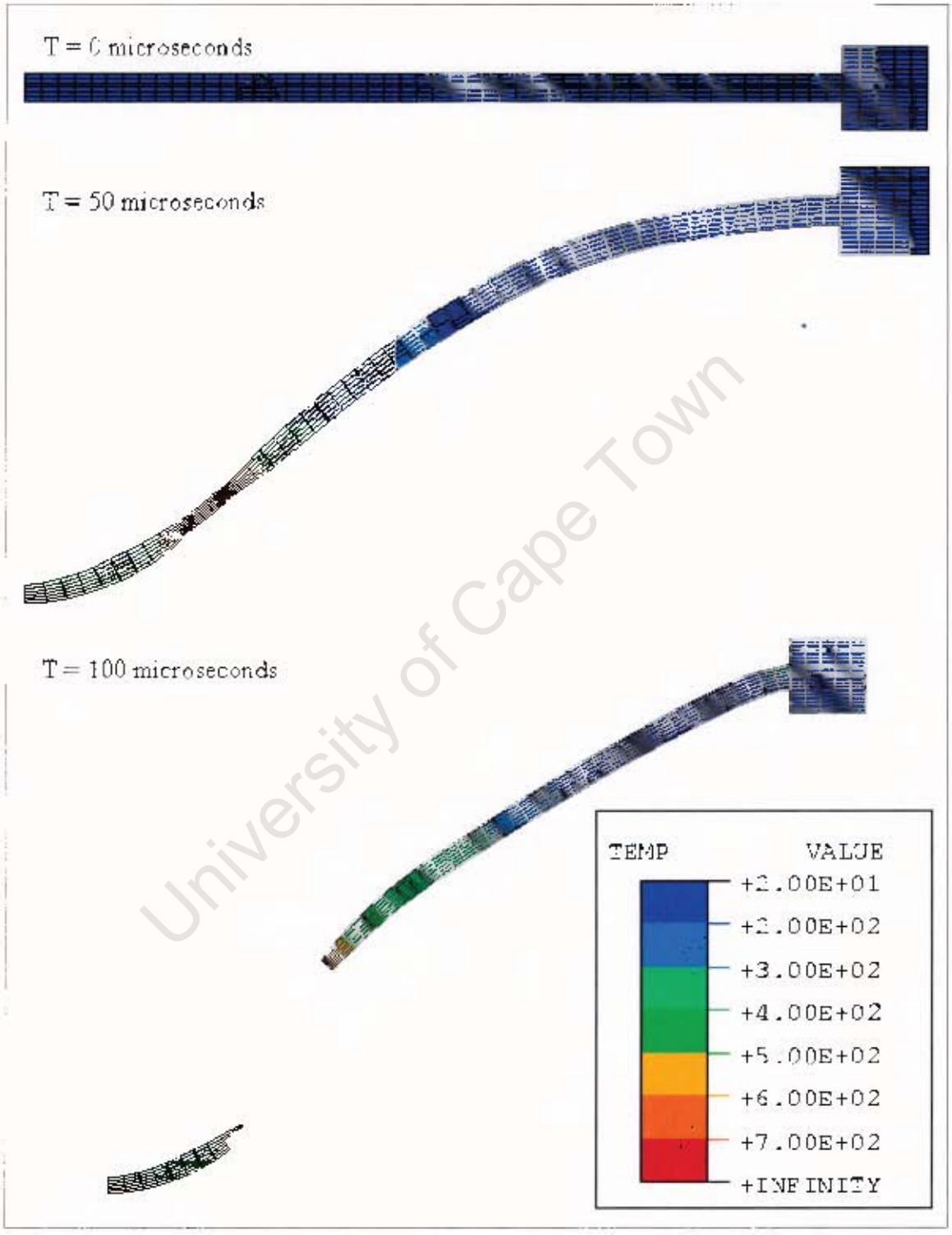

Figure H.7: Temperature Profiles of Plate T16 for a Mesh Density of 1 x 0.30 mm.

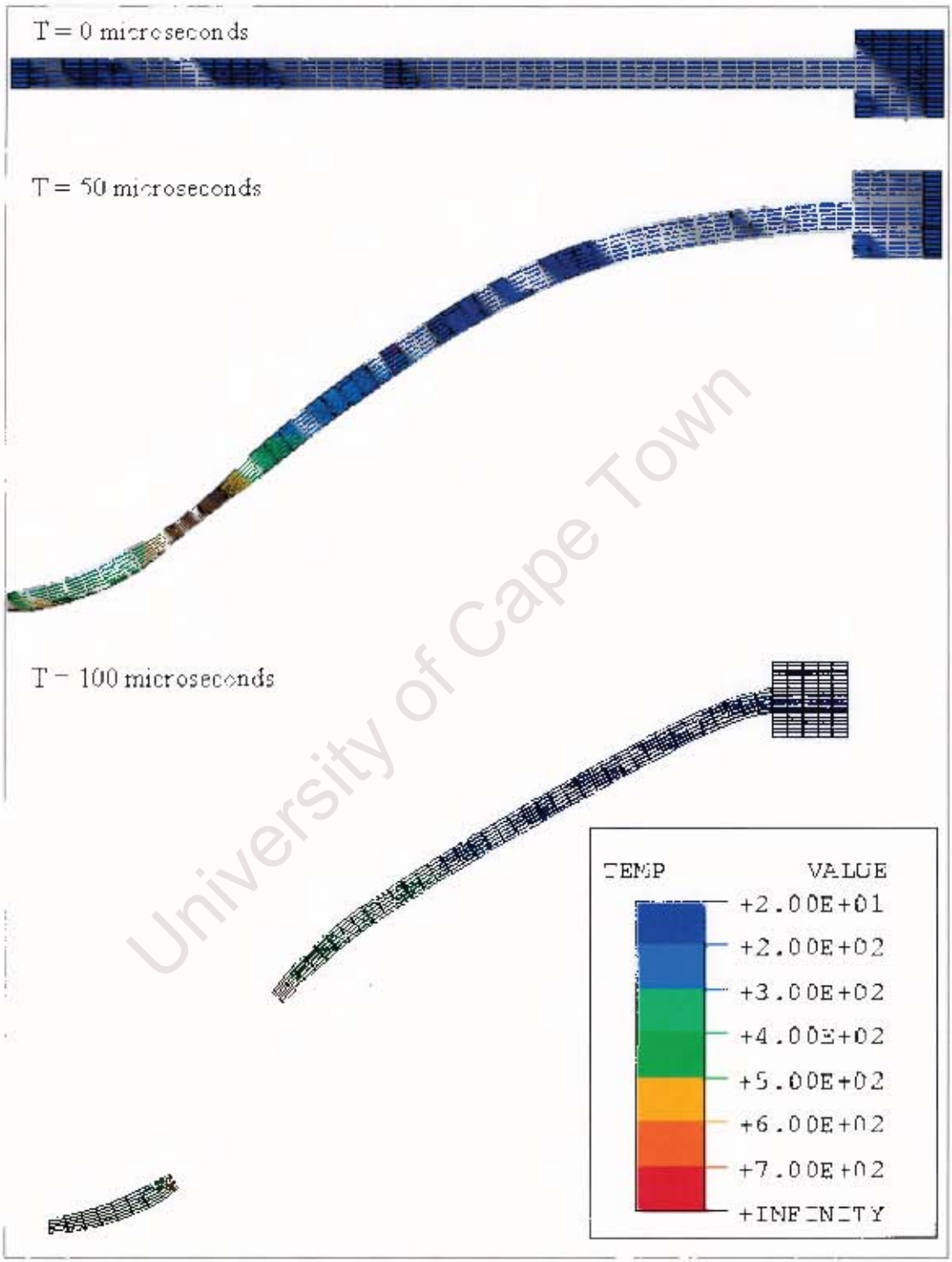

Figure H.8: Temperature Profiles of Plate T18 for a Mesh Density of 1 x 0.288 mm.

Appendix I

FINE MESH RESULTS

This appendix shows temperature profiles of the capped plates $T10$, $T11$, $T12$, $T16$ and $T18$ using a mesh density of 0.04 x 0.04 mm in Figures I.1 to I.5. The figures contain three whole model temperature profiles, namely at the following times after the start of the blast:

- Time equals to zero.
- Just before fracture.
- Time of 30 μs.

A close-up section of the shear band is given immediately before fracture. All the plates experience failure at the location of capping and at the boundary of the thin plate. Failure at the boundary of the thin plates cannot be seen in Figures I.1 to I.5 since boundary failure occurs after 80μs (*see* Figure 5.8).

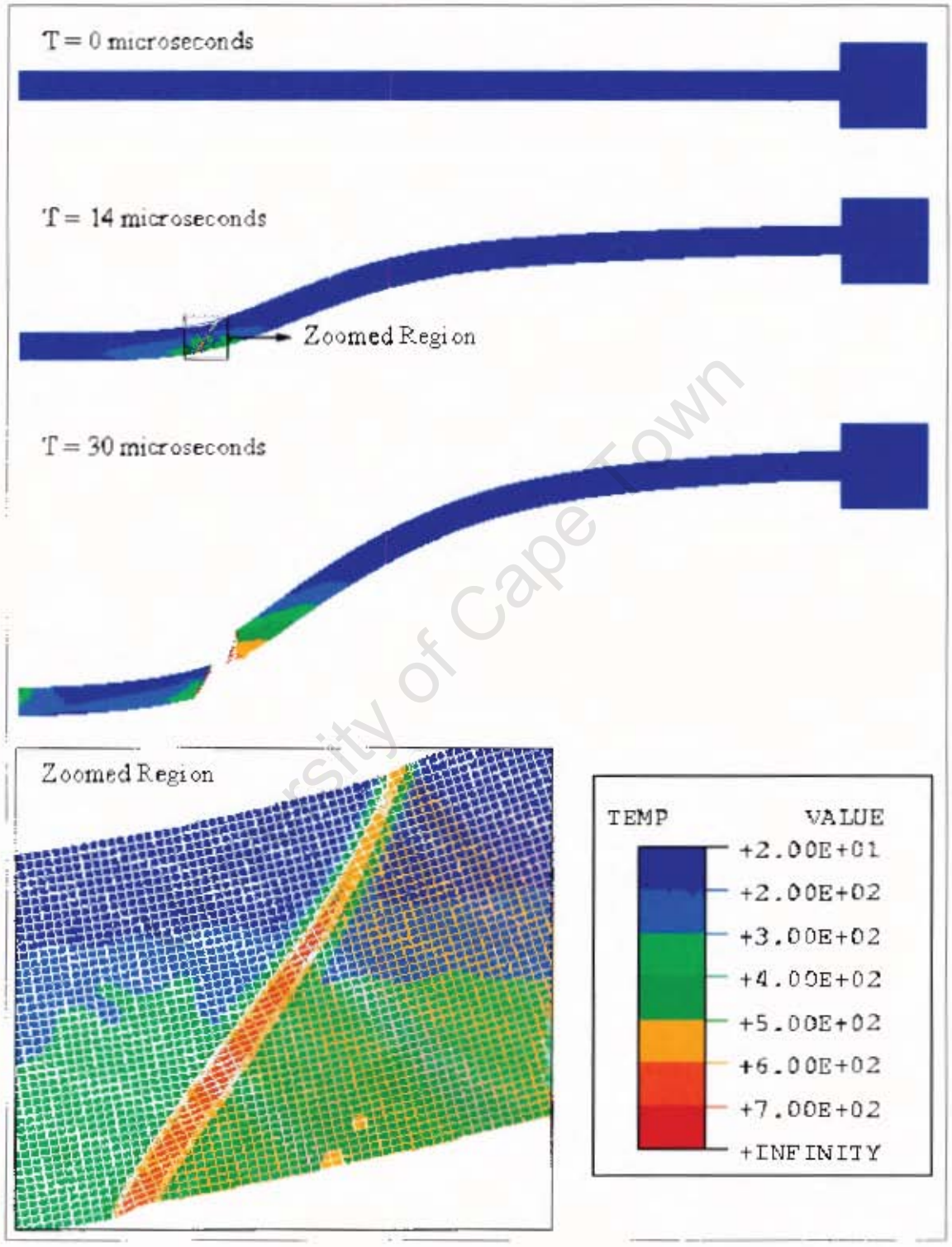

Figure L1: Temperature Profiles of Plate T10 for a Mesh Density of 0.04 x 0.04 mm.

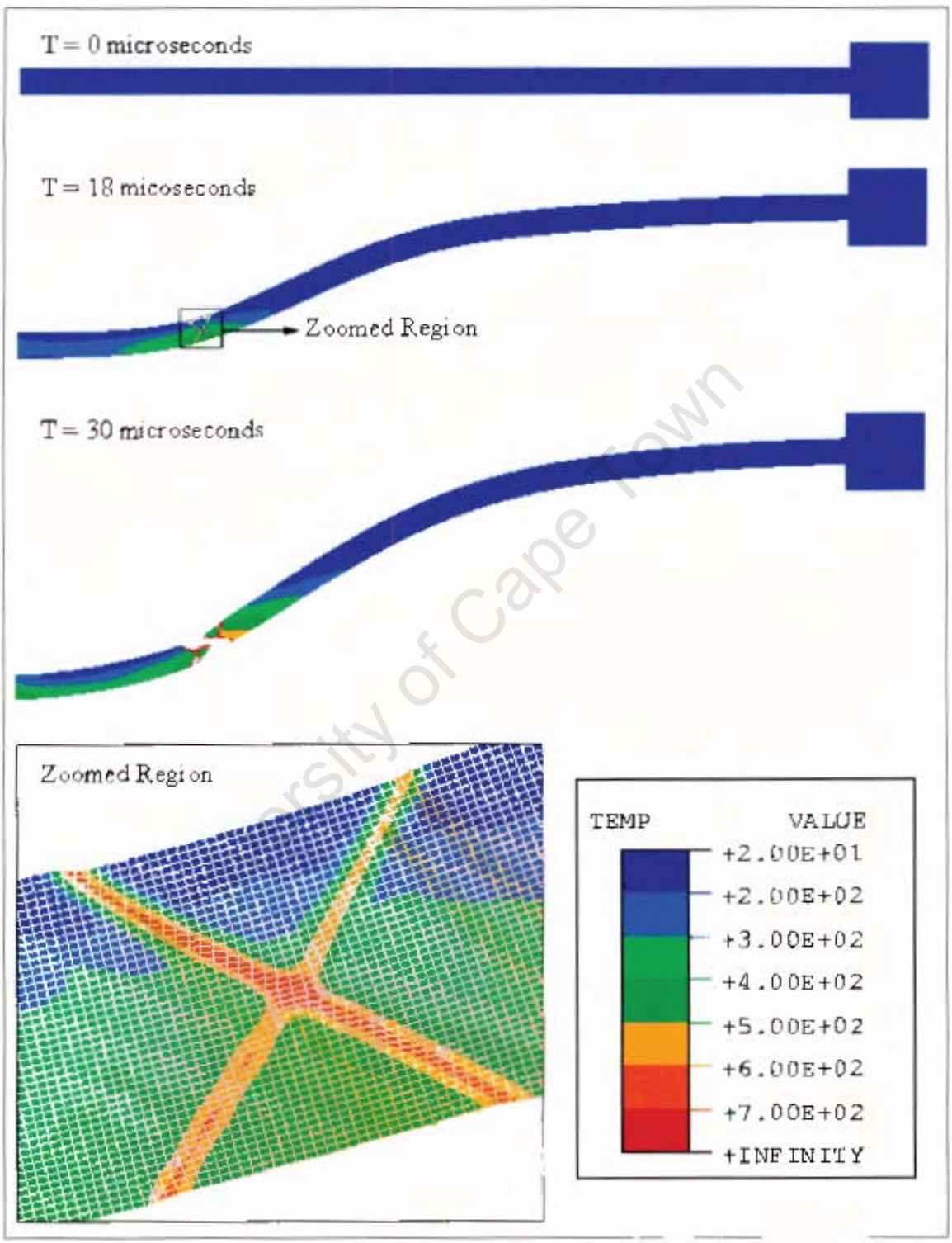

Figure I.2: Temperature Profiles of Plate T11 for a Mesh Density of 0.04 x 0.04 mm.

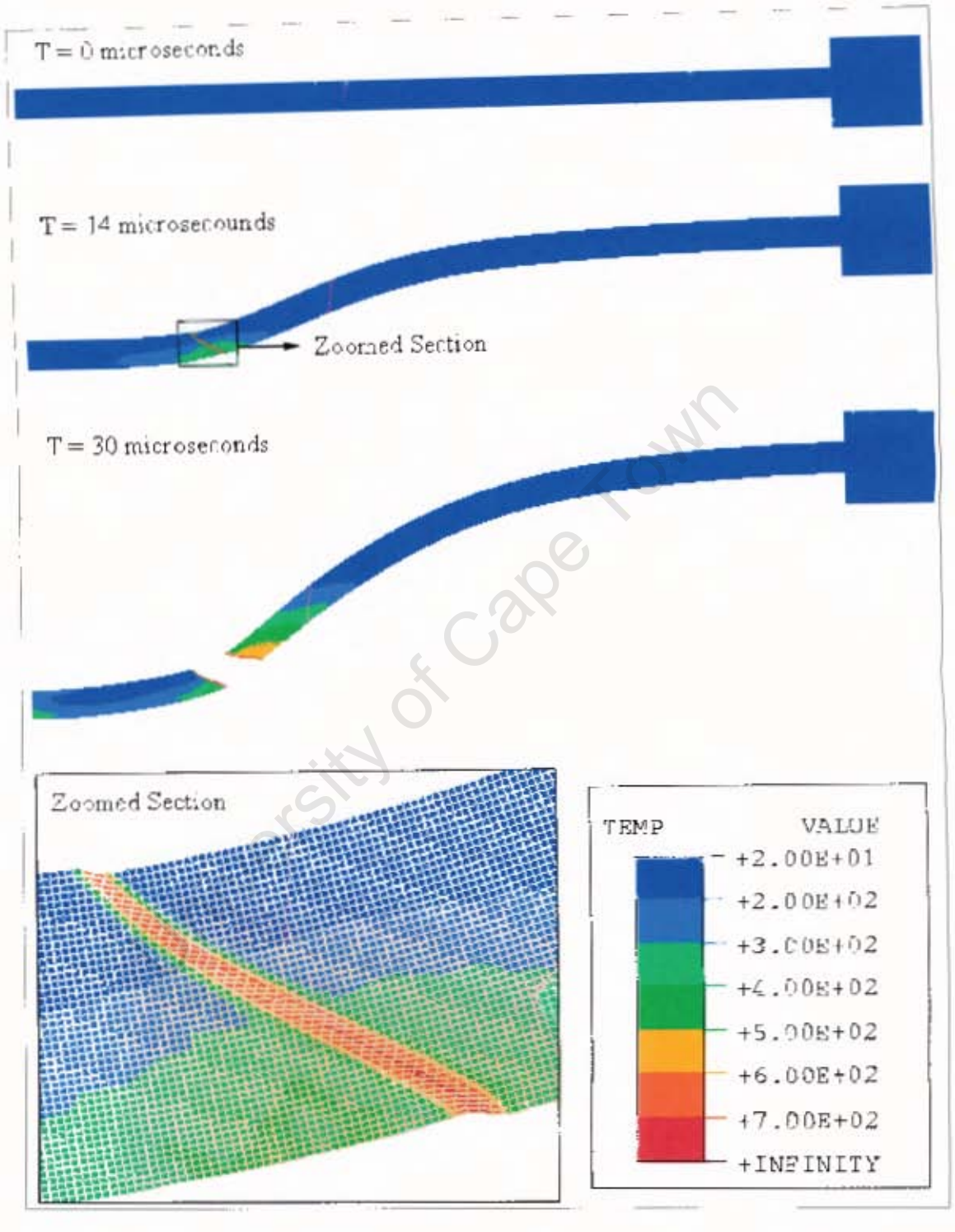

Figure I.3: Temperature Profiles of Plate T12 for a Mesh Density of 0.04 x 0.04 mm.

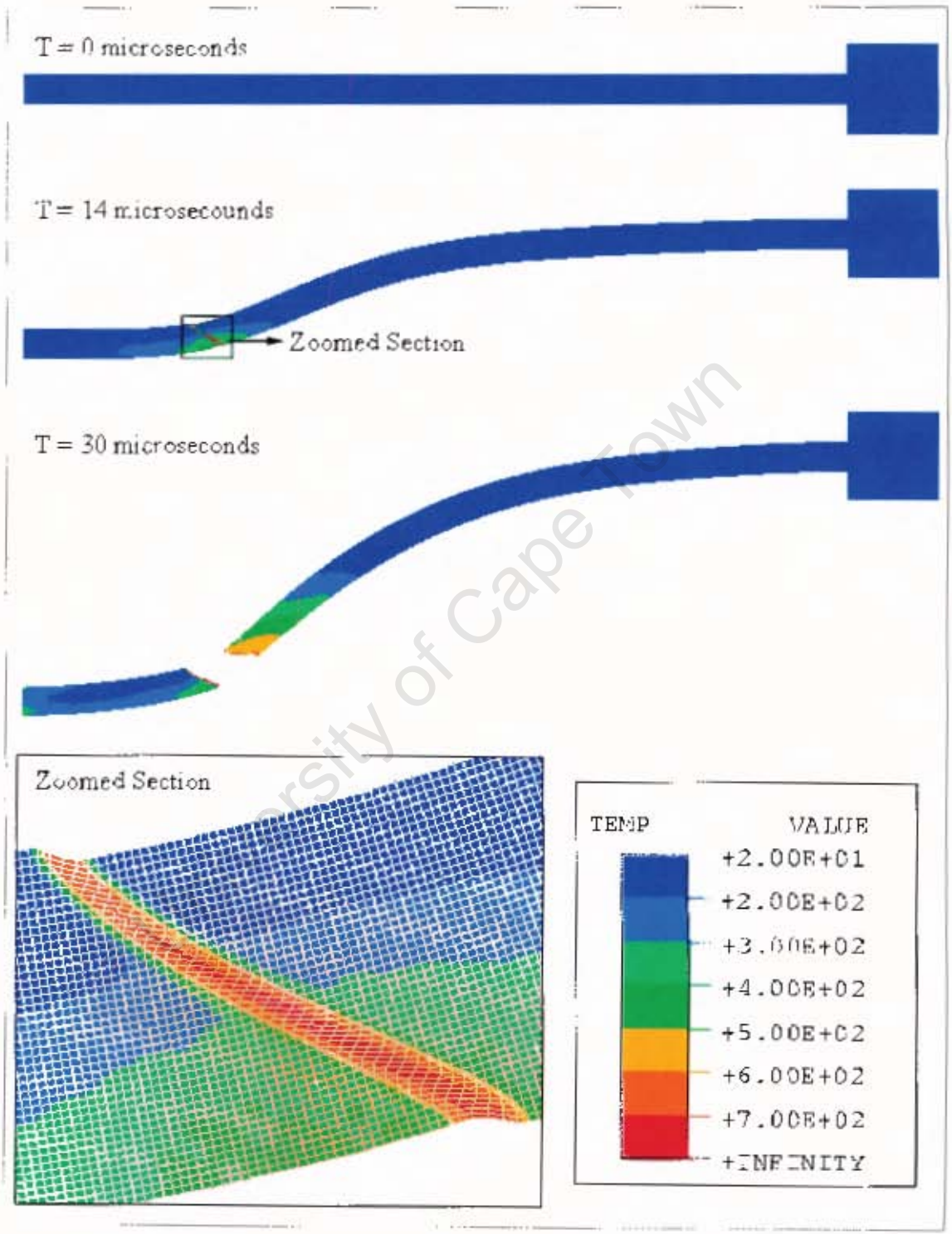

Figure 1.4: Temperature Profiles of Plate T16 for a Mesh Density of 0.04 x 0.04 mm.

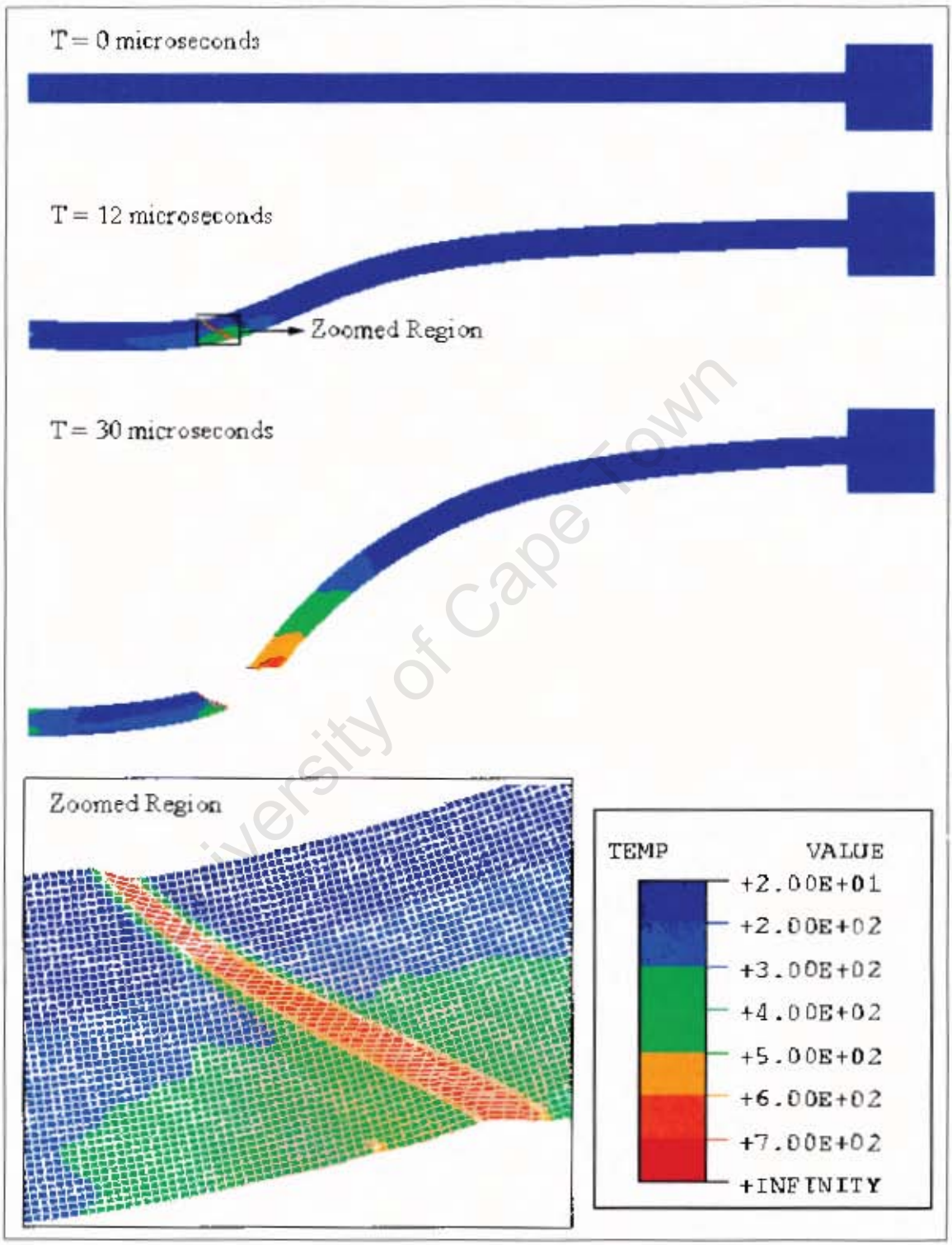

Figure I.5: Temperature Profiles of Plate T18 for a Mesh Density of 0.04 x 0.04 mm.